

# Full-Band Monte Carlo Simulation of Single Photon Avalanche Diodes





Denis Dolgos

**Full-Band Monte Carlo  
Simulation of Single Photon  
Avalanche Diodes**

Hartung-Gorre Verlag Konstanz  
2011

Reprint of Diss. ETH No. 18777

SERIES IN MICROELECTRONICS

VOLUME 203

edited by Wolfgang Fichtner  
Qiuting Huang  
Heinz Jäckel  
Gerhard Tröster  
Bernd Witzigmann

**Bibliographic information published by Die Deutsche Nationalbibliothek**

Die Deutsche Nationalbibliothek lists this publication in the Deutsche Nationalbibliografie; detailed bibliographic data is available on the Internet at:  
<http://dnb.d-nb.de>

Copyright © 2011 by Denis Dolgos

First edition 2011

HARTUNG-GORRE VERLAG KONSTANZ  
<http://www.hartung-gorre.de>

ISSN 0936-5362

ISBN-10: 3-86628-295-8

ISBN-13: 978-3-86628-295-7

# Abstract

This dissertation describes the simulation of high-energy charge transport in single photon avalanche diodes by means of the full-band Monte Carlo technique. Single or few photon detection has become an important feature in optoelectronic systems and enables a variety of interesting applications in medicine, biology, and physics. At present, the full-band Monte Carlo solution of the Boltzmann transport equation is the most promising theoretical tool for high-field carrier dynamics within semiconductor physics of semiclassical charge transport. The particles propagate classically in the phase space whereas quantum mechanics is involved in the computation of the dispersion relation and carrier scattering. A computationally efficient formulation of scattering rates, while keeping the main physical features, renders the CPU-intensive calculation of breakdown characteristics of single photon avalanche diodes feasible. On the deca-nanometer length scale non-equilibrium effects like the velocity overshoot, the dead-space, and the nonlocal impact ionization become important and are naturally covered by the Monte Carlo technique. A full-band Monte Carlo simulator built from scratch is applied to the high-field charge dynamics of the multiplication process in single photon avalanche diodes. Compared to previous works employing simple charge transport models, the solution of the Boltzmann transport equation and the incorporation of the full-band structure puts the evaluation of the breakdown probability, the time to avalanche breakdown and its jitter on deeper theoretical grounds. The examined multiplication layers, having widths between 55 nm and 500 nm, are made of gallium arsenide, indium phosphide, and indium aluminium arsenide. The breakdown probability exhibits a steeper

rise versus the reverse bias for smaller multiplier sizes. The time to avalanche breakdown and its jitter decrease for smaller multiplier widths. Additionally, an impact ionization model for the scattering rates and the secondary carrier energies, being based on the random- $\mathbf{k}$  approximation, is presented.

# Zusammenfassung

Diese Dissertation beschreibt die Simulation hochenergetischen Ladungsträgertransports in Einzelphotonen-Lawinendioden (single photon avalanche diodes) anhand der Monte Carlo Methode, welche die vollständige Bandstruktur miteinbezieht. Die Detektion einzelner beziehungsweise weniger Photonen ist zu einem wichtigen Merkmal optoelektronischer Systeme erwachsen und ermöglicht eine Vielzahl interessanter Anwendungen auf den Gebieten der Medizin, Biologie und Physik. Derzeit gilt die Monte Carlo Methode mit Einbezug der vollständigen Bandstruktur zur Lösung der Boltzmannschen Transportgleichung als vielversprechendstes theoretisches Verfahren, um die Dynamik von Ladungsträgern bei hohen Feldern im Rahmen der Physik des semiklassischen Ladungsträgertransports in Halbleitern zu beschreiben. Die Teilchenausbreitung im Phasenraum wird klassisch behandelt, während die Ladungsträgerstreuung quantenmechanisch zu berechnen ist. Die Formulierung recheneffizienter Streuraten, bei der die wichtigsten physikalischen Merkmale erhalten bleiben, ermöglicht erst die aufwendige Berechnung der Durchbrucheigenschaften von Einzelphotonen-Lawinendioden. Auf der Decanometer-Längenskala werden Nichtgleichgewichtseffekte wie das Überschießen der Geschwindigkeit (velocity overshoot), der benötigte Abstand bis zur Stoßionisation (dead-space) und nichtlokale Stoßionisation wichtig und sind in der Monte Carlo Methode auf natürliche Art miteinbezogen. Ein Monte Carlo Simulator mit vollständiger Bandstruktur, welcher von Grund auf neu entwickelt wurde, wird auf die Dynamik hochenergetischer Ladungsträger während des Multiplikationsprozesses in Einzelphotonen-Lawinendioden angewendet. Im Vergleich zu früheren Arbeiten, die einfache Ladungsträgertransportmodelle verwenden, ist die Lösung

der Boltzmannschen Transportgleichung mit Einbezug der vollständigen Bandstruktur für die Berechnung der Durchbruchwahrscheinlichkeit, der Zeit bis zum Lawinendurchbruch und dessen Schwankung theoretisch grundlegender. Die untersuchten Multiplikationslagen mit Dicken zwischen 55 nm und 500 nm bestehen aus Galliumarsenid, Indiumphosphid und Indiumaluminiumarsenid. Die Durchbruchwahrscheinlichkeiten weisen einen steileren Verlauf mit steigender Sperrspannung für dünnere Multiplikationsschichten auf. Die Zeit bis zum Lawinendurchbruch und dessen Schwankung nehmen für dünnere Multiplikationsschichten ab. Des Weiteren wird ein Stoßionisationsmodell für die Streuraten und Nachstreuenergien vorgestellt, welches auf der random- $\mathbf{k}$  Approximation beruht.

# Contents

<b>Abstract</b>	<b>v</b>
<b>Zusammenfassung</b>	<b>vii</b>
<b>1 Introduction</b>	<b>1</b>
<b>2 Physical Basics of High-field Charge Transport</b>	<b>5</b>
2.1 Hierarchy of Equations . . . . .	5
2.1.1 Quantum Kinetics . . . . .	7
2.1.2 Semiclassical Boltzmann Transport Equation . . . . .	8
2.1.3 Method of Moments . . . . .	11
2.2 Monte Carlo Method . . . . .	12
2.2.1 Introduction . . . . .	12
2.2.2 Algorithm . . . . .	14
<b>3 Full-band Structure</b>	<b>21</b>
3.1 Brillouin Zone Discretization . . . . .	22
3.2 Full-band Structure Computation . . . . .	25
3.3 Valley Allocation . . . . .	25
3.4 Density of States . . . . .	28
3.5 Direction-Weighted Density of States . . . . .	30
3.6 Density Of States Overlap Integral . . . . .	32
3.7 Particle Motion in Phase Space . . . . .	34
<b>4 Scattering Mechanisms</b>	<b>37</b>
4.1 Carrier-Phonon Scattering . . . . .	38
4.1.1 Elastic Acoustic Phonon Scattering . . . . .	40

4.1.2	Nonpolar Optical Phonon Scattering . . . . .	41
4.1.3	Polar Optical Phonon Scattering . . . . .	43
4.1.4	Intervalley Phonon Scattering . . . . .	45
4.2	Impact Ionization Scattering . . . . .	48
4.3	Alloy Scattering . . . . .	53
4.4	Overview of Scattering Rate Forms . . . . .	54
4.5	Choice of State After Scattering . . . . .	56
4.6	Approximations . . . . .	61
4.6.1	Fermi's Golden Rule . . . . .	61
4.6.2	Transition Matrix Elements . . . . .	62
<b>5</b>	<b>Single Photon Avalanche Diodes</b>	<b>67</b>
<b>6</b>	<b>Full-band Monte Carlo Simulator</b>	<b>73</b>
<b>7</b>	<b>Simulation Results</b>	<b>79</b>
7.1	Calibration . . . . .	79
7.2	Impact Ionization Scattering Model . . . . .	89
7.3	Single Photon Avalanche Diodes . . . . .	95
<b>8</b>	<b>Conclusion and Outlook</b>	<b>107</b>
8.1	Major Achievements . . . . .	107
8.2	Future Work . . . . .	108
<b>A</b>	<b>Generation of Random Numbers According to Given Distributions</b>	<b>111</b>
A.1	Direct Technique . . . . .	112
A.1.1	Continuous Case . . . . .	112
A.1.2	Discrete Case . . . . .	112
A.2	Rejection Technique . . . . .	112
<b>B</b>	<b>Useful Formulas</b>	<b>115</b>
B.1	Irreducible Wedge . . . . .	115
B.2	Transformation Matrices . . . . .	116
B.3	Cutting Cubes with Planes . . . . .	117
B.4	Time to Cubic Box Boundaries . . . . .	119
B.5	Reciprocal lattice vectors . . . . .	119
B.6	Nonparabolic Expressions . . . . .	120
B.6.1	Band Structure . . . . .	120



B.6.2	Density of States . . . . .	120
B.6.3	Direction-Weighted Density of States . . . . .	121
<b>C</b>	<b>Further Material Properties and Constants</b>	<b>123</b>
C.1	Fundamental Physical Constants . . . . .	123
C.2	Material Parameters . . . . .	124
C.3	Density of States . . . . .	135
C.4	Scattering Rates . . . . .	139
	<b>Notation and Acronyms</b>	<b>143</b>
	Acronyms . . . . .	143
	Symbols . . . . .	144
	<b>Bibliography</b>	<b>155</b>
	<b>Curriculum Vitae</b>	<b>171</b>



# Chapter 1

## Introduction

With shrinking sizes of semiconductor devices over the decades the need for more complex modeling of device physics has risen. Smaller devices operate at higher electric fields, which leads to higher energies of the charge carriers, when the applied bias is kept constant. The approximations of simpler charge transport models do not hold anymore. In the past, classical balance equation modeling like drift-diffusion, energy transport, and hydrodynamic approaches provided a fully satisfactory description of device behavior for typical system lengths of several microns. In this regime local steady-state properties are similar to the bulk material. By trend, industry developers of devices underline the importance of fast design iteration processes whereas academia emphasizes the importance of modeling necessary physics. In industry, technology computer-aided design (TCAD) groups apply simpler balance equations with empirical extensions down to sub-micron length scales. However, the semi-classical Boltzmann transport equation (BTE) provides an adequate theoretical modeling of submicron sized systems. The simulation of high-energy (around 5 eV) carrier dynamics (scattering) and kinetics (propagation) renders the incorporation of the full-band structure necessary. Approaching system sizes of tens of nanometers, quantum effects become important, manifested in coherent transport, quantization effects, and tunneling. For the devices examined in this work the inclusion of quantum effects

is necessary for carrier scattering and negligible for particle propagation. At present, the full-band Monte Carlo (FBMC) solution of the BTE is the most accurate device simulation method for semiclassical charge transport [1, 2]. The FBMC approach serves as benchmark for approximate methods. On the deep-submicron length scale non-equilibrium effects like the velocity overshoot, the dead-space, and the nonlocal impact ionization become important and are naturally covered by the Monte Carlo (MC) technique.

This doctoral thesis has originated the C++ object-oriented full-band Monte Carlo simulator *CarloS* with incorporated computationally efficient modeling of device physics [1]. *CarloS* is applied to the simulation of single photon avalanche diode (SPAD) properties. The applications of SPADs comprise quantum computing [3], quantum cryptography [4], fundamental studies of quantum physics [5], three-dimensional laser detection and ranging imaging [6], free space optical communication [7], semiconductor circuit diagnostics [8], and fluorescence lifetime imaging in molecular biology and medicine [9] among others. Remarkable progress has been achieved for SPADs regarding their photon detection efficiency, dark count rate, jitter, and afterpulsing [10, 11]. There have been contradictory predictions concerning the dependence of the breakdown probability on the multiplication region width. Wang et al. [12] and Ramirez et al. [13] predict a rising breakdown probability for thicker multiplication regions using a history-dependent analytical impact ionization model and the recursive dead-space multiplication theory, respectively. On the other hand, Ng et al. [14], Hayat et al. [15], and Tan et al. [16] predict the opposite behavior applying the hard dead-space impact ionization model within McIntyre's extended theory, the recurrence equations by McIntyre, and the stochastic random path length model, respectively. The models of Refs. [12, 13, 14, 15, 16] rely on simplified impact ionization and charge transport modeling without taking scattering and the dispersion of charge carriers on a microscopic level into account. Up to now, the dead-space effect is estimated analytically or taken from full-band Monte Carlo simulations. Relevant effects like the velocity overshoot and the nonlocal impact ionization are neglected. Such effects gain importance for shrinking multiplication region sizes. The simulation of high-energy carrier dynamics and kinetics renders the incorporation

of the full-band structure necessary. FBMC simulations involve a high computational burden, which forced previous research on the computation of SPAD breakdown characteristics to apply simplified charge transport modeling. However, with nowadays parallel CPU power on standard computer clusters combined with computationally efficient approaches [1] it has become feasible to gain sufficient statistics with FBMC simulations for the evaluation of breakdown probabilities and standard deviations of variables of interest.

This work concentrates on the investigation of the high-energy charge transport and multiplication process in the SPAD multiplier consisting of gallium arsenide (GaAs), indium phosphide (InP), or indium aluminium arsenide ( $\text{In}_{0.52}\text{Al}_{0.48}\text{As}$ , InAlAs). The effect of tunneling is not considered. The author aims to clarify the contradictory predictions of the breakdown probability by solving the semiclassical Boltzmann transport equation by means of the ensemble FBMC method and to put the computation of SPAD properties on deeper theoretical grounds. Additionally, an impact ionization model based on the random- $\mathbf{k}$  approximation is introduced for GaAs, InP, InAlAs, and indium gallium arsenide ( $\text{In}_{0.53}\text{Ga}_{0.47}\text{As}$ , InGaAs).

The author has the intention to give an overview of the essential theoretical background needed for the understanding of the full-band Monte Carlo transport model. Hopefully, doctoral students and interested readers may form their tedious gathering of detailed information more clearly. The thesis is organized in eight chapters. Chapter 2 summarizes the physical basics of charge transport at high electric fields. The different levels of the theoretical description of charge transport and the Monte Carlo solution technique are presented. The third chapter introduces the discretization of the reciprocal space and the integration over  $\delta$ -functions in the Brillouin zone, which is important for scattering rate computations. Chapter 4 discusses the important scattering mechanisms in III-V semiconductors and the approximations leading to a computationally efficient modeling of carrier scattering. An introduction to single photon avalanche diodes is given in Chapter 5. Chapter 6 illuminates selected details of the full-band Monte Carlo simulator. Chapter 7 presents the calibration results, the impact ionization model based on the random- $\mathbf{k}$  approximation, and

the breakdown behavior of single photon avalanche diodes. Finally, Chapter 8 concludes the thesis and possible future work is suggested.

# Chapter 2

# Physical Basics of High-field Charge Transport

## 2.1 Hierarchy of Equations

In general, the more fundamental the physical description, the harder the solution of the problem. From a physical point of view it is appreciable to choose a more fundamental description. But from a computational standpoint the contrary is preferred. The choice of an appropriate model for the computation of semiconductor structures depends on the system size and its relation to characteristic length scales [17] (p. 12) [18] (p.1):

- *de Broglie wavelength*

The de Broglie wavelength  $\lambda_B = h/p$  is related to the momentum  $p$  of the particle, where  $h$  is the Planck constant.  $\lambda_B$  is a measure of the length scale for quantum mechanical wave effects. An electron in thermal equilibrium at 300 K in GaAs has a thermal de Broglie wavelength of approximately 17 nm.

- *Mean-free path*

The mean-free path  $l_m$  defines the scale where the initial momentum is randomized.  $l_m$  depends on the average distance before a scattering event occurs. The effectiveness to change the particle's momentum depends on the scattering type [18] (p.1 and 16). For example, the electron mean free path in GaAs varies from 30 nm to 3 nm for applied electric fields from  $3 \cdot 10^5$  V/m to  $5 \cdot 10^7$  V/m [19] (Fig. 12, p. 4204).

- *Phase-relaxation length*

The phase-relaxation length  $l_\varphi$  is the distance that a carrier propagates before its initial phase is destroyed, i.e.  $l_\varphi$  defines the length scale where interference effects occur. The ability to destroy the phase depends on the scattering type [18] (p.1 and 17). The phase-relaxation time of GaAs at 5 K is of the order of 1 ps [20] (Fig. 2, p. 7752).

Comparing the different characteristic length scales with the system size  $L_s$ , distinct transport regimes arise [17] (p. 13):

- *Quantum-size effects* appear for  $\lambda_B \gtrsim L_s$ . Quantum confinement effects occur and the density of states is modified. The scattering rates in low dimensional structures differ from scattering rates in 3 dimensions.
- *Coherent transport* occurs for  $l_\varphi \gtrsim L_s$ . The quantum mechanical wave function has a well-defined phase and quantum-interference phenomena are possible.
- In the *(quasi-)ballistic transport regime*  $l_m \gtrsim L_s$  holds. A charge carrier is able to cross the device without, or few, scattering events.
- *Classical diffusive transport* is present for a macroscopic sized system obeying  $l_m, l_\varphi, \lambda_B \ll L_s$ . Many elastic and inelastic scattering events occur on the trajectory of a carrier between the terminals.

*CarloS* is applied to devices that feature a smallest system size of approximately 50 nm. Hence, the regime of quasi-ballistic transport



is relevant.

A full description of charge transport requires a self-consistent solution of a set of transport equations coupled to Maxwell's equations for the electromagnetic fields. The fixed background charges and the free carrier densities affect the electric field profile. In turn, the electric field acts as a source of force on the charged particles. For most applications in small semiconductor devices it is not necessary to solve the whole system of Maxwell equations. Incorporation of Gauss law, leading to the Poisson equation, is sufficient. For applications considered in this work the magnetic field is insignificant. Thus, the Maxwell equations containing the magnetic field are negligible [21] (p. 7 and Ref. 3 therein). For relatively high electric fields and relatively low excess carrier densities the electric field update may become dispensable because the relative change of the electric field turns out to be small [22]. Then, the initial electric field profile, being computed with a commercial drift-diffusion simulator [23], is kept for the whole (frozen-field) computation.

Three hierarchical levels of the theoretical description of charge transport in semiconductors appear: the quantum mechanical description, the semiclassical description, and the classical description (compare with Ravaioli et al. [24]). This work employs the semiclassical approach to charge transport in semiconductors. In the following sections the semiclassical theory is considered in more detail than the quantum and classical approaches.

### 2.1.1 Quantum Kinetics

At the most basic level, quantum mechanics describes the dynamics of particles. However, two problems render the application of quantum theory difficult. The inclusion of the full dispersion relation and detailed scattering is associated with an immense computational burden. Practically, the use of quantum mechanics is limited to restricted physical situations. Single quantum features are incorporated into classical or semiclassical models [24] (p. 3).

Luisier et al. [25] use the nonequilibrium Green's function (NEGF) formalism with an atomistic full-band structure and electron-phonon scattering to simulate three-dimensional nanowire field-effect transistors. Frey et al. [26] incorporate the phenomenological Büttiker scattering into a wave function formalism within the effective mass approach and discusses analogies and differences to more detailed scattering approaches within an effective mass NEGF approach. Static applications like size quantization effects have been analyzed with the coupled Schrödinger and Poisson equations [24] (p. 3). Esposito et al. [27] utilize the Schrödinger equation within the effective mass approximation or envelope function equation for quantum transport simulations. Another approach involves the density matrix, which is the expectation value of the particle number operator [17] (Eq. (6.2.3), p. 175). The Heisenberg equation governs the dynamics of the density matrix. The Fourier transform of the density matrix is the Wigner function being the quantum version of the classical carrier distribution. The Liouville equation governs the evolution of the Wigner function.

### 2.1.2 Semiclassical Boltzmann Transport Equation

To quote Barker [28] (p. 127): "It [the Boltzmann transport theory] also works far better than one could reasonably expect from its origin as a graft from the classical theory of dilute gases."

Starting from the density matrix formulation, it is possible to reduce the set of density matrix equations to the semiclassical Boltzmann transport equation. Following assumptions are made [17] (p. 18) [28] (p. 128):

- The system size is bigger than the de Broglie wavelength meaning that the distribution function varies little over the de Broglie wavelength and quantum confinement is insignificant.
- The system size is bigger than the phase-relaxation length. Thus, coherent effects are irrelevant.

- The density of carriers has to be low enough in order to justify binary collisions. Many-body effects are negligible and a single carrier description is used.
- The duration of a collision  $t_c$  is much shorter than the time between successive collisions. Scattering events are local in space and time, i.e. scattering transitions occur practically immediately. This means that external forces, with a wave vector  $q_{\text{ex}}$  and an angular frequency  $\omega_{\text{ex}}$ , have to be sufficiently weak and the spatial and temporal variations have to be small on a microscopic scale:  $q_{\text{ex}}l_m < 1$  and  $\omega_{\text{ex}}t_c < 1$ . Otherwise, the field accelerates markedly the carrier during the collision. This effect is called intracollisional field effect. Electronic states quantize due to the action of sufficiently strong electric or magnetic fields [28] (p. 129 and Ref. Barker,1979b therein).
- The scattering is weak and collisions are independent. The carrier states possess a long life-time and are nearly stationary with a well-defined momentum state until a scattering event occurs. The carrier states are quasi-free.

For more details consult Schöll [17] (p. 18), Büfler [21] (p. 9), and Barker [28] (p. 127) and the references therein.

In the case of negligible quantum nature of the carrier kinetics, the Boltzmann transport equation describes the charge transport through semiconductor devices. For charge carrier dynamics, quantum mechanics is involved in the scattering probability computation within the collision term  $\hat{S}[f(\mathbf{r}, \mathbf{k}, t)]$  and the velocity  $\mathbf{v}$  of the particle. Newton's law is used for the carrier kinetics. The Boltzmann transport equation describes the evolution of the semiclassical carrier distribution function  $f(\mathbf{r}, \mathbf{k}, t)$  under the action of forces, where  $\mathbf{r}$  is the spatial coordinate,  $\mathbf{k}$  is the wave vector and  $t$  is the time [29] (Eq. (2.9), p. 16):

$$\frac{\partial f_\nu(\mathbf{r}, \mathbf{k}, t)}{\partial t} + \mathbf{v}_\nu(\mathbf{r}, \mathbf{k}) \nabla_{\mathbf{r}} f_\nu(\mathbf{r}, \mathbf{k}, t) + \mathbf{F}_\nu(\mathbf{r}, \mathbf{k}, t) \frac{1}{\hbar} \nabla_{\mathbf{k}} f_\nu(\mathbf{r}, \mathbf{k}, t) = \hat{S}[f] \quad (2.1)$$

with the band or valley index  $\nu$ . The charge carrier's velocity is the expectation value of the velocity operator  $\hat{v} = -i\hbar/m_0\nabla_{\mathbf{r}}$  with the electron rest mass  $m_0$  [30] (p. 121):

$$\mathbf{v}_\nu = \int \Psi^* \hat{v} \Psi d^3r = \frac{1}{\hbar} \nabla_{\mathbf{k}} E_\nu(\mathbf{r}, \mathbf{k}) . \quad (2.2)$$

Here,  $\Psi$  is the particle's wave function. The force [29] (Eq. (2.5), p. 15)

$$\mathbf{F}_\nu(\mathbf{r}, \mathbf{k}, t) = q(\mathbf{E} + \mathbf{v}_\nu \times \mathbf{B}) \quad (2.3)$$

has contributions from external electric  $\mathbf{E}$  and magnetic fields  $\mathbf{B}$ . In compositionally graded heterostructures additional forces as a result of the position-dependent bandgap accelerate particles [31]. The scattering operator is [29] (Eq. (2.9), p. 16)

$$\begin{aligned} \hat{S}[f] = & \sum_{\nu'} \sum_{\mathbf{k}' \in \text{BZ}} \sum_{\lambda} W_{\text{in}}^\lambda(\nu, \mathbf{k} | \nu', \mathbf{k}')(\mathbf{r}, t) f_{\nu'}(\mathbf{r}, \mathbf{k}', t) (1 - f_\nu(\mathbf{r}, \mathbf{k}, t)) \\ & - \sum_{\nu'} \sum_{\mathbf{k}' \in \text{BZ}} \sum_{\lambda} W_{\text{out}}^\lambda(\nu', \mathbf{k}' | \nu, \mathbf{k})(\mathbf{r}, t) f_\nu(\mathbf{r}, \mathbf{k}, t) (1 - f_{\nu'}(\mathbf{r}, \mathbf{k}', t)) \end{aligned} \quad (2.4)$$

where BZ stands for the first Brillouin zone.  $W_{\text{in}}^\lambda$  is the in-scattering transition rate for the scattering mechanism  $\lambda$  that a carrier in the state  $(\mathbf{r}, \mathbf{k}', \nu')$  passes into the state  $(\mathbf{r}, \mathbf{k}, \nu)$  at the time  $t$ .  $W_{\text{out}}^\lambda$  is the out-scattering transition rate that a carrier in the state  $(\mathbf{r}, \mathbf{k}, \nu)$  changes into the state  $(\mathbf{r}, \mathbf{k}', \nu')$  at the time  $t$  by means of the scattering mechanism  $\lambda$ . The Pauli blocking factors  $(1 - f)$  stem from the Pauli exclusion principle. Spin flips due to scattering are very improbable because the involved magnetic fields are too small [30] (p. 393). Hence, a summation in Eq. (2.4) over the spin quantum numbers is not necessary. Where it is appropriate, a factor of 2 will appear. For practical reasons the sum over the dense  $\mathbf{k}$ -states is replaced by an integral

$$\sum_{\mathbf{k} \in \text{BZ}} f(\mathbf{k}) \rightarrow \int_{V_{\text{BZ}}} d^3k \rho_{\mathbf{k}} f(\mathbf{k}) \quad (2.5)$$

with the density of states in the reciprocal space  $\rho_{\mathbf{k}} = V/8\pi^3$ , the volume of the first Brillouin zone  $V_{\text{BZ}}$ , and the crystal volume  $V$ . The

deviation of a perfect crystal periodicity is the source of nonstationarity or scattering. In general, the main sources of scattering are due to phonons, impurities, alloy disorder, surfaces, interfaces and other carriers. The standard to compute the transition rates is to start from Fermi's golden rule [29] (Eq. (4.1), p. 57)

$$W_{nn'}(\mathbf{k}, \mathbf{k}') = \frac{2\pi}{\hbar} |M_{nn'}(\mathbf{k}, \mathbf{k}')|^2 \delta(E_{n'}(\mathbf{k}') - E_n(\mathbf{k}) \mp E_{nn'}^{\text{trans}}(\mathbf{k}, \mathbf{k}')) \quad (2.6)$$

with the matrix element of the interaction process  $M_{nn'}(\mathbf{k}, \mathbf{k}')$  from the initial reciprocal space vector  $\mathbf{k}$  and band  $n$  to the final state  $(n', \mathbf{k}')$  and the corresponding energy transfer  $E_{nn'}^{\text{trans}}(\mathbf{k}, \mathbf{k}')$  of the interaction process. A discussion concerning a more detailed insight into the computation of scattering rates is given in Chap. 4.

The nonlinearity of the BTE in the distribution function appears threefold. The Pauli blocking factors produce a product of distribution functions. The transition rates  $W$  contain the distribution function through carrier-carrier screening effects. The electromagnetic force depends on the distribution of charged particles [29] (p. 16). The nonlinear BTE makes self-consistent iteration schemes necessary, which are a source of numerical instability and computational cost. To reduce the computational burden, the linear BTE is favorable. One assumes that the carrier concentration is low enough to omit Pauli's exclusion principle. The short-range rearrangement of carriers due to Coulomb interaction, i.e. carrier-carrier scattering, is neglected.

Eq. (2.1) is a system of coupled Boltzmann equations for different particle species being coupled by the scattering operator defined in Eq. (2.4). The different particle species may be electrons and holes or carriers in different valleys of the band structure [30] (p. 388). For example, the coupling of electrons and holes is due to impact ionization. Intervalley scattering couples the valleys among each other.

### 2.1.3 Method of Moments

A further reduction of complexity from semiclassical to classical transport is possible by taking the  $m$ th moment of the Boltzmann transport

equation. Therefore, Eq. (2.1) is multiplied with a function  $\phi(\mathbf{k}) = \mathbf{k}^m$  and integrated over the momentum space. The result is [32] (Eq. (1.12), p. 6)

$$\frac{\partial (n(\mathbf{r}, t) \langle \phi \rangle(\mathbf{r}, t))}{\partial t} + \nabla_{\mathbf{r}} \mathbf{j}_{\langle \phi \rangle}(\mathbf{r}, t) = n(\mathbf{r}, t) F_{\langle \phi \rangle}(\mathbf{r}, t) + \left. \frac{\partial (n \langle \phi \rangle)}{\partial t} \right|_{\text{coll}} \quad (2.7)$$

with the particle density  $n(\mathbf{r}, t) = \int d^3k f(\mathbf{r}, \mathbf{k}, t)$ , the mean value  $\langle \phi \rangle = \int \phi(\mathbf{k}) f(\mathbf{r}, \mathbf{k}, t) d^3k / n(\mathbf{r}, t)$ , the generalized flux  $\mathbf{j}_{\langle \phi \rangle} = n \langle \mathbf{v} \phi \rangle$ , the generalized driving force  $F_{\langle \phi \rangle} = q \mathbf{E} \langle \nabla_{\mathbf{p}} \phi \rangle$  and the momentum  $\mathbf{p} = \hbar \mathbf{k}$ . The detailed information about the momentum space is lost making the equations easier and faster to solve [32] (p. 6). The generalized flux contains the next order of moment. At some point the hierarchy must be truncated by formulating the flux term by lower moments. For example, for  $m = 0, 1, 2$  there follows a conservation law for the carrier density, the current density and the energy density, respectively. To make the collision term convenient for calculations, the relaxation time approximation is used. Depending on the further level of approximation or simplification, several transport models like the hydrodynamic transport model, the energy balance model, or the drift-diffusion model may be deduced [32, 17, 24]. As a result of the approximations, the approaches based on the method of moments are less suitable for high-field transport. Nevertheless, these models find widespread use in the industry due to their fast simulation runs.

Further approximations concerning the transport model, the device geometry and doping profile lead to compact approaches [24] (p. 1 and 9). These models have simple analytical solutions of the semiconductor equations in explicit form.

## 2.2 Monte Carlo Method

### 2.2.1 Introduction

The Monte Carlo simulation is a stochastic solution method relying on random experiments or rather random numbers. Seemingly, the term Monte Carlo has its origin from physicists working at the Los Alamos Scientific Laboratory on nuclear weapons who had to give a

code name for their secret project using random experiments [33,34]. They named the method after the district of Monaco being famous for gambling.

The MC method comes into play when deterministic solution methods are computationally prohibitive. In 1966, for the first time, Kurosawa [35] introduced the Monte Carlo method to the solution of charge transport in semiconductors. Over the last 45 years the MC method has been improved eminently [17] (p. 59) [36] (p. 1899). The use of the MC method to solve the BTE has been the most popular and successful one [24] (p. 3). Other solution methods are tested and compared to the MC method. The MC approach is considered to be more general than the description of particle dynamics via the Boltzmann transport equation, for example, the MC approach can naturally include fluctuations and noise [24] (p. 2). The advantages of the MC algorithm are the clear physical picture of drift and scattering allowing a simple implementation of the main MC loop (see Fig. 6.2), the ability to parallelize the code easily for the linear Boltzmann equation owing to statistical independent numerical experiments, the widespread use in the hot carrier modeling community, the modular character, the extensibility of the band structure model and the scattering mechanisms. The disadvantages are the high computational burden and the nondeterministic nature of the method causing noisy solutions. Statistical enhancement methods [37, 38] and backward MC algorithms [36] are able to reduce the statistical noise. Statistical methods become necessary when the carrier concentration differs in regions by several orders of magnitude. *CarloS* uses a weighted ensemble and has an incorporated multiple refresh method (for details, see Meier [22] and Jungemann et al. [29]).

Other creative solution methods for the Boltzmann transport equation exist with its advantages and disadvantages. Banoo [39] describes the first direct numerical solution method usable for practical device simulations. Mustieles et al. [40] present a deterministic method allocating each particle a weight that varies in time according to the collision integral. Leung et al. [41] use a modification of Chambers path integral solution. Alam et al. [42,43,44] introduce scattering matrices to solve the Boltzmann transport equation. Ventura et al. [45]

describe a spherical harmonics expansion of the distribution function. Galler et al. [46] present a multigroup model and solve the coupled system of electrons and polar optical phonons. Kometer et al. [47] use a cellular automata approach. Brugger et al. [48] invented moments of the inverse scattering operator. Peikert et al. utilize a wavelet basis to discretize the multi-dimensional phase-space [49]. Jakumeit et al. [50] developed an evolutionary algorithm. Rees [51] introduces an iterative method.

## 2.2.2 Algorithm

The Monte Carlo algorithm follows from the path integral representation of the Boltzmann transport equation formulated for the conditional probability density [29] (Eq. (3.13), p. 36) [36] (Eq. (17), p. 1901)

$$p(\boldsymbol{\xi}, t | \boldsymbol{\xi}_0, t_0) = p_0(\boldsymbol{\xi}, t | \boldsymbol{\xi}_0, t_0) + \int_{t_0}^t \int \int p(\boldsymbol{\xi}, t | \boldsymbol{\xi}'_1, t_1) W(\boldsymbol{\xi}'_1, \boldsymbol{\xi}_1) p_0(\boldsymbol{\xi}_1, t_1 | \boldsymbol{\xi}_0, t_0) d\boldsymbol{\xi}'_1 d\boldsymbol{\xi}_1 dt_1 \quad (2.8)$$

with the particle state vector  $\boldsymbol{\xi} = (\mathbf{r}, \mathbf{k})$  and the conditional probability density  $p_0(\boldsymbol{\xi}, t | \boldsymbol{\xi}_0, t_0)$  that a particle in the state  $(\boldsymbol{\xi}_0, t_0)$  survives into  $(\boldsymbol{\xi}, t)$  without scattering [29] (Eq. (3.12), p. 36):

$$p_0(\boldsymbol{\xi}, t | \boldsymbol{\xi}_0, t_0) = \delta(\boldsymbol{\xi} - \boldsymbol{\xi}_{\text{drift}}(t | \boldsymbol{\xi}_0, t_0)) \times \exp \left( - \int_{t_0}^t W(\boldsymbol{\xi}_{\text{drift}}(t' | \boldsymbol{\xi}_0, t_0)) dt' \right). \quad (2.9)$$

$\boldsymbol{\xi}_{\text{drift}}(t | \boldsymbol{\xi}_0, t_0)$  is the solution of the equation of motion for a charged carrier propagating from  $(\boldsymbol{\xi}_0, t_0)$  to  $(\boldsymbol{\xi}_{\text{drift}}, t)$ . Interestingly, based on the conjugate [29] (p. 36) of Eq. (2.8) a backward MC method follows, which propagates particles backward in time. The backward MC method allows efficient simulation of rarely occupied regions [52].



The relation between the conditional probability density and the distribution function is [36] (Eq. (1), p. 1900)

$$f(\boldsymbol{\xi}, t) = \int d\boldsymbol{\xi}_0 p(\boldsymbol{\xi}, t | \boldsymbol{\xi}_0, t_0) f(\boldsymbol{\xi}_0, t_0). \quad (2.10)$$

For example, a Newtonian equation of motion, a constant electric field and small time increments result in

$$\boldsymbol{\xi}_{\text{drift}}(t | \boldsymbol{\xi}_0, t_0) = (\mathbf{r} + \mathbf{v}(t - t_0), \mathbf{k}_0 + \frac{q}{\hbar} \mathbf{E}(t - t_0)) \quad (2.11)$$

(compare with Sec. 3.7). In words, Eq. (2.8) is the probability density that a particle in the state  $(\boldsymbol{\xi}_0, t_0)$  propagates to  $(\boldsymbol{\xi}_1, t_1)$  without scattering, then, scatters instantaneously from  $(\boldsymbol{\xi}_1, t_1)$  to  $(\boldsymbol{\xi}'_1, t_1)$ , propagates without and with scattering from  $(\boldsymbol{\xi}'_1, t_1)$  into  $(\boldsymbol{\xi}, t)$ . Repeated insertion of Eq. (2.8) into itself gives the Neumann series [29] (Eq. (3.15), p. 37)

$$\begin{aligned} p(\boldsymbol{\xi}, t | \boldsymbol{\xi}_0, t_0) &= p_0(\boldsymbol{\xi}, t | \boldsymbol{\xi}_0, t_0) \\ &+ \int_{t_0}^t \int \int p_0(\boldsymbol{\xi}, t | \boldsymbol{\xi}'_1, t_1) W(\boldsymbol{\xi}'_1 | \boldsymbol{\xi}_1) p_0(\boldsymbol{\xi}_1, t_1 | \boldsymbol{\xi}_0, t_0) d\boldsymbol{\xi}'_1 d\boldsymbol{\xi}_1 dt_1 \\ &+ \int_{t_0}^t \int \int \int_{t_1}^t \int \int p_0(\boldsymbol{\xi}, t | \boldsymbol{\xi}'_2, t_2) W(\boldsymbol{\xi}'_2 | \boldsymbol{\xi}_2) p_0(\boldsymbol{\xi}_2, t_2 | \boldsymbol{\xi}'_1, t_1) \\ &\quad \times W(\boldsymbol{\xi}'_1 | \boldsymbol{\xi}_1) p_0(\boldsymbol{\xi}_1, t_1 | \boldsymbol{\xi}_0, t_0) \\ &\quad \times d\boldsymbol{\xi}'_2 d\boldsymbol{\xi}_2 dt_2 d\boldsymbol{\xi}'_1 d\boldsymbol{\xi}_1 dt_1 \\ &+ \dots \end{aligned} \quad (2.12a)$$

$$= p_0(\boldsymbol{\xi}, t | \boldsymbol{\xi}_0, t_0) + p_1(\boldsymbol{\xi}, t | \boldsymbol{\xi}_0, t_0) + p_2(\boldsymbol{\xi}, t | \boldsymbol{\xi}_0, t_0) + \dots \quad (2.12b)$$

The physical interpretation of Eq. (2.12) is straightforward. The first term  $p_0$  is the probability density that the particle does not scatter during its propagation from  $(\boldsymbol{\xi}_0, t_0)$  to  $(\boldsymbol{\xi}, t)$ . The second term is the probability density that the charge carrier scatters once. The particle propagates without scattering from  $(\boldsymbol{\xi}_0, t_0)$  to  $(\boldsymbol{\xi}_1, t_1)$ , scatters instantly from  $(\boldsymbol{\xi}_1, t_1)$  to  $(\boldsymbol{\xi}'_1, t_1)$  and propagates without

scattering from  $(\xi'_1, t_1)$  to  $(\xi, t)$ . The third term is the probability density that a particle scatters twice. The carrier propagates from  $(\xi_0, t_0)$  to  $(\xi_1, t_1)$ , scatters instantaneously from  $(\xi_1, t_1)$  to  $(\xi'_1, t_1)$ , propagates from  $(\xi'_1, t_1)$  to  $(\xi_2, t_2)$ , scatters in no time from  $(\xi_2, t_2)$  to  $(\xi'_2, t_2)$  and propagates from  $(\xi'_2, t_2)$  to  $(\xi, t)$  without scattering. The interpretation of higher-order terms is likewise. Thus, scattering processes interrupt accelerated flights, which are a result of acting forces on the charge carriers.

The algorithm asks for the probability for the first scattering occurrence. Integrating Eq. (2.9) over all final states gives the probability in  $[t_0, t]$  for zero scattering events

$$P_0(t|\xi_0, t_0) = \int p_0(\xi, t|\xi_0, t_0)d\xi \quad (2.13)$$

and  $1 - P_0$  for at least one scattering event. Because the evaluation of the integral in the exponential of Eq. (2.9) is demanding, Rees introduced a fictitious scattering mechanism named self-scattering such that the total scattering rate  $\bar{\Gamma}$ , including self-scattering, is a constant in terms of time [53]. Then, the computation of the integral gets straightforward (see Eq. (2.17)). The self-scattering mechanism does not change the state of a particle [29] (Eq. (3.19), p. 38):

$$W_{\text{self}}(\xi'|\xi) = (\bar{\Gamma} - W_{\text{real}}(\xi'|\xi))\delta(\xi' - \xi) . \quad (2.14)$$

The upper bound estimate for  $\bar{\Gamma}$  should be as near as possible to the sum of the real scattering rates to minimize self-scattering occurrences. Otherwise, self-scattering events occur too often and waste CPU time because the total scattering rate is already computed but finally the particle does not change its state. This work employs the variable  $\Gamma$  scheme, which is able to reduce the self-scattering events by introducing  $\mathbf{r}$ - and  $\mathbf{k}$ -space region  $\Lambda_i$  dependent  $\bar{\Gamma}$ 's [29] (Eq. (3.30), p. 40)

$$\bar{\Gamma}_i(\xi) = \max_{\xi \in \Lambda_i} [W(\xi)] \quad (2.15)$$

with the scattering rate

$$W(\xi) = \sum_{\mathbf{k}'} W(\xi'|\xi) . \quad (2.16)$$

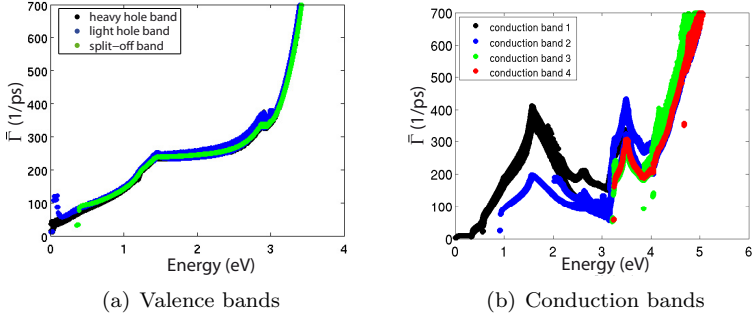


Figure 2.1: Upper bound estimates  $\bar{\Gamma}(E(\mathbf{k}))$  for valence bands and conduction bands of GaAs.

Naturally, the regions are primitives of the  $\mathbf{k}$ -space grid and depend on the real-space coordinate by means of the material. Fig. 2.1 depicts an example of the variable  $\Gamma$  scheme for GaAs. With the help of a random number  $r$  between zero and one, the time for the first scattering event is drawn [29] (Eq. (3.26), p. 40<sup>1</sup>):

$$t_s = -\frac{1}{\bar{\Gamma}(\xi)} \ln r . \quad (2.17)$$

The Monte Carlo technique picks a multitude of single trajectories of Eq. (2.12) and does not compute the multi-dimensional integrals deterministically. After a free flight a scattering process has to be chosen. The total scattering rate including self-scattering

$$W_{\text{tot}}(\nu, \mathbf{k}) = \sum_{\nu'} \sum_{\mathbf{k}'} W_{\text{out}}(\nu', \mathbf{k}' | \nu, \mathbf{k}) + W_{\text{in}}(\nu, \mathbf{k} | \nu', \mathbf{k}') + W_{\text{self}}(\mathbf{k}', \mathbf{k}) \quad (2.18a)$$

$$= \sum_{\lambda} W^{\lambda}(\mathbf{k}) \quad (2.18b)$$

consists of several contributions  $\lambda$  including self-scattering. According to the direct method for discrete probabilities (compare with App.

<sup>1</sup> $r$  and  $1 - r$  are uniformly distributed

A.1.2) the  $i$ th scattering mechanism is chosen [29] (Eq. (3.28), p.40) with a random number  $r$  [29] (Eq. (3.28), p. 40):

$$\sum_{\lambda=1}^{i-1} W^\lambda(\mathbf{k}) < r\bar{\Gamma} \leq \sum_{\lambda=1}^i W^\lambda(\mathbf{k}) . \quad (2.19)$$

The final  $\mathbf{k}$ -state after scattering for the  $i$ th scattering mechanism is computed by means of the rejection technique (see App. A.2) using the probability density [29] (Eq. (3.29), p. 40)

$$p_i(\mathbf{k}') = \frac{W_i(\mathbf{k}', \mathbf{k})}{W_i(\mathbf{k})} . \quad (2.20)$$

Section 4.5 describes the details about the state after scattering probabilities for the single scattering processes.

In the Monte Carlo method an ensemble of test particles represents the real-world charge carriers. The single-particle probability density is estimated by [29] (Eq. (3.44), p. 44)

$$p(\boldsymbol{\xi}, t) = \frac{1}{N_{\text{sim}}} \sum_{i=1}^{N_{\text{sim}}} \bar{w}_i \delta(\boldsymbol{\xi} - \boldsymbol{\xi}_i(t)) \quad (2.21)$$

with the number  $N_{\text{sim}}$  of carriers in the ensemble and the particle's statistical weight  $\bar{w}_i$  fulfilling  $\sum_{i=1}^{N_{\text{sim}}} \bar{w}_i = N_{\text{sim}}$ . The expectation value of an ensemble average of the microscopic quantity  $A(\boldsymbol{\xi}, t)$  is given by [29] (Eq. (3.46), p. 44)

$$\langle A \rangle(t) = \int A(\boldsymbol{\xi}) p(\boldsymbol{\xi}, t) d\boldsymbol{\xi} = \frac{1}{N_{\text{sim}}} \sum_{i=1}^{N_{\text{sim}}} \bar{w}_i A(\boldsymbol{\xi}_i(t)) . \quad (2.22)$$

The standard deviation  $\sigma$  of the random variable  $A(\boldsymbol{\xi}, t)$  reads [54] (Eq. (16.53), p. 774)

$$\sigma_A = \sqrt{\langle A^2 \rangle - \langle A \rangle^2} . \quad (2.23)$$

In summary, the main Monte Carlo loop consists of four steps (compare with Fig. 6.2):

1. stochastic computation of a free flight time using Eq. (2.17),
2. integration of the equation of motion (see Sec. 3.7),
3. stochastic selection of a scattering mechanism by means of Eq. (2.19),
4. stochastic calculation of a state after scattering with Eq. (2.20).



## Chapter 3

# Full-band Structure

For small carrier energies around a local valley minimum it is possible to approximate the band structure with analytical terms (see App. B.6). Analytical expressions are advantageous because the scattering integrals and the equations of motion can be solved analytically, making the MC simulator faster. For higher particle energies no analytical approximations exist that include the details of the full-band structure. Nevertheless, in the words of Fischetti et al. [55] (p. 815), in a “band structure cuisine” the full-band structure is emulated with many-valley models. The approach of using analytical band structures has the benefit of lower computational burden and may resolve engineering problems. But for kinetic energies higher than approximately 1 eV, the density of states (DOS) (compare with Fig. 3.5), the effective mass, and the velocity deviate strongly from nonparabolic approximations of the band structure. Therefore, the author has numerically incorporated the full-band structure, in both, the computation of carrier propagation and scattering rates.

Interestingly, the work of Dunn et al. [56] shows a good agreement between a Monte Carlo simulator using multiple nonparabolic valleys and the full-band structure. By trend, for smaller energy separation of the valleys and for smaller band gap energies, the description with nonparabolic valleys becomes better. The earlier onset of impact ionization events and valley transitions lower the kinetic energy of

the carriers. Electrons and holes less often reach badly described regions of the band structure. An agreement of the charge transport calculations based on the full-band structure and the multivalley band model has to be expected for mean values where the majority of particles remains in the energy range being well approximated by the analytical nonparabolic band structure. For example, the mean energy and the mean velocity are well described. However, for properties that depend on the high-energy tail of the distribution function, like impact ionization, differences have to be expected. For example, the evaluation of the mean time to breakdown in single photon avalanche diodes requires the realistic band structure.

### 3.1 Brillouin Zone Discretization

This work examines III-V materials crystallizing in the zincblende structure. Due to the 48-fold symmetry of the face-centered cubic lattice, it is sufficient to compute the dispersion relation on the 1/48th part of the first Brillouin zone, namely the irreducible wedge. Apps. B.1 and B.2 summarize the faces of the irreducible wedge and the transformation matrices  $\mathbf{T}$  being elements of the point group of the cubic crystal system. Application of an adequate transformation matrix folds an arbitrary  $\mathbf{k}$ -vector inside the first Brillouin zone into the irreducible wedge. This work uses an equidistant tensor grid to discretize the irreducible wedge. The Gilat-Raubenheimer method [57] is utilized, which asks for energy gradients (compare with Sec. (3.4)), for the density of states computation. To avoid vanishing energy gradients in high symmetry points, the cube centers are placed on an offset mesh [58] (Eq. (A1), p. 337)

$$\mathbf{k}_{\text{cb}} = (2i + 1)b\hat{e}_x + (2j + 1)b\hat{e}_y + (2k + 1)b\hat{e}_z . \quad (3.1)$$

Here,  $i$ ,  $j$ , and  $k$  are natural numbers,  $\hat{e}_x$ ,  $\hat{e}_y$ ,  $\hat{e}_z$  are unit vectors along the cubic box axes,  $2b = 2\pi/aN$  is the cube edge length, and  $N$  is the natural number of cubic boxes in the  $\hat{e}_x$ -direction (compare with Fig.



3.1). Additionally, in this work  $N/2$  has to be a natural number <sup>1</sup>. The definition of the irreducible wedge is [58] (Eq. (A8), p. 339)

$$0 \leq k_z \leq k_y \leq k_x \leq \frac{2\pi}{a} \quad (3.2a)$$

$$k_x + k_y + k_z \leq \frac{3}{2} \frac{2\pi}{a} \quad (3.2b)$$

with the lattice constant  $a$ . From Eqs. (3.2a) and (3.2b) the values for  $i$ ,  $j$ , and  $k$  follow [58] (Eq. (A9), p. 339):

$$0 \leq k \leq j \leq i \leq N - 1 \quad (3.3a)$$

$$2(i + j + k) \leq 3N - 1. \quad (3.3b)$$

The total number of cubic boxes discretizing the irreducible wedge is given by [58] (Eq. (A10), p. 339)

$$N_{\text{tot}} = \frac{N(N+2)(2N+5)}{24}. \quad (3.4)$$

Fig. 3.1 depicts the irreducible wedge of the first Brillouin zone with the discretization boxes. The center points of the cubic boxes are the grid points of Eq. (3.1). The method of Gilat and Raubenheimer asks for the computation of the area  $A_0$  of a cubic box cut by a equi-energy plane (see Sec. 3.4). Therefore, cubes lying partly outside the irreducible wedge have a different contribution compared to boxes lying completely inside the irreducible wedge [58] (p. 339). Symmetry considerations are very useful to compute the contribution of boundary boxes. Consider the case where the  $i$ th cubic box lies completely inside the irreducible wedge. Then, the contribution of the area to the whole Brillouin zone is  $A_{\text{BZ}} = 48A_0$ . The box weight is  $w_i = 1$ . Assume that a boundary of the irreducible wedge cuts the cubic box such that, including the neighboring wedge, the cubic box lies again inside these two wedges. Then, the contribution to the whole Brillouin zone is  $A_{\text{BZ}} = 48/2 \cdot A_0$ . The box weight is  $w_i = 1/2$ . The third possibility is that boundary boxes lie partly outside of the irreducible wedge such that six wedges are needed to

---

<sup>1</sup>This additional condition allows an easier treatment of boundary box weights. The U-point  $2\pi/a(1, 1/4, 1/4)$  lies on a corner of the cubic box.

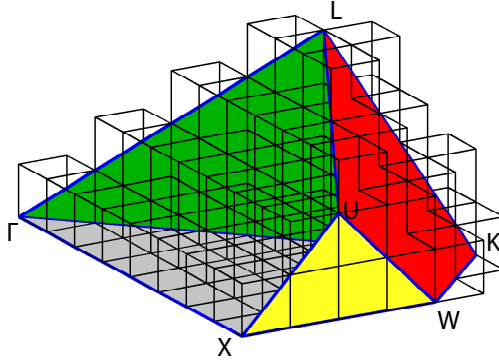


Figure 3.1: Irreducible wedge of the first Brillouin zone with cubic discretization boxes for  $N = 8$ .

make the boundary box completely lie inside the wedges. Here, the box weight is  $w_i = 1/6$ . Summarized, for the discretization scheme of this work, the box weighting function is

$$w_i = \begin{cases} 1 & \text{if } i\text{th cube cut by 0 boundary planes} \\ \frac{1}{2} & \text{if } i\text{th cube cut by 1 boundary plane} \\ \frac{1}{6} & \text{if } i\text{th cube cut by 3 boundary planes} . \end{cases} \quad (3.5)$$

The boundary planes (see App. B.1) of the irreducible wedge cutting the discretization boxes with respect to the box weights are:

- boxes having  $w_i = 1/2$ :  
 $\Gamma\text{KL}$ ,  $\Gamma\text{LUX}$ ,  $\text{KLUW}$ ,
- boxes having  $w_i = 1/6$ :  
 $\Gamma\text{LUX}$  and  $\Gamma\text{KL}$ ,  $\Gamma\text{LUX}$  and  $\text{KLUW}$ ,  $\Gamma\text{KL}$  and  $\text{KLUW}$ ,
- boxes having  $w_i = 1$ :  
 no cuts with boundary planes.

## 3.2 Full-band Structure Computation

The majority of full-band Monte Carlo simulators compute their band structure from programs using the empirical pseudopotential method (EPM) [59, 60]. Because of the empirical properties of the EPM, the agreement with experimental data is better than methods using ab initio potentials. Ab initio calculations of the band structure utilize other severe approximations, which render the agreement with experiment worse. The full-band structure and the energy gradients on the  $\mathbf{k}$ -space grid defined by Eq. (3.1) are calculated with the program *ESEP*, which employs the EPM. The parameters for the empirical pseudopotential band structure computations are taken from Chelikowsky et al. [59] and Zheng et al. [61]. The energy around a cubic box center point  $\mathbf{k}_{cb}$  [58] (Eq. (3), p. 324) is expanded linearly:

$$E(\mathbf{k}) = E(\mathbf{k}_{cb}) + \nabla_{\mathbf{k}}E(\mathbf{k}_{cb})(\mathbf{k} - \mathbf{k}_{cb}) . \quad (3.6)$$

It has to be pointed out that the band structure is the basic ingredient of full-band transport. The particle dynamics, i.e. the scattering rates and states after scattering, and the carrier kinetics, i.e. the motion in phase space, rely on the band structure. In literature, even for the well-known III-V compound GaAs, differences in the DOS, and therefore, in the band structure are present, especially for higher energies (compare with Fig. 3.7). The solutions obtained with different FBMC simulators vary for higher energies [62].

Figs. 3.2 and 3.3 present the band structures, including spin-orbit coupling, of GaAs, InP, InAlAs, and InGaAs along special paths through the first Brillouin zone.

## 3.3 Valley Allocation

The carrier-phonon deformation potentials are in good approximation constant within a valley (compare with Sec. 4.1). Therefore, the utilized scattering model asks for a partition of the  $\mathbf{k}$ -space into valleys for each conduction band. Jungemann et al. [29] (Eq. (4.5), p. 59) and Bufler [63]<sup>2</sup> allocate the valleys according to symmetry

---

<sup>2</sup>private communication

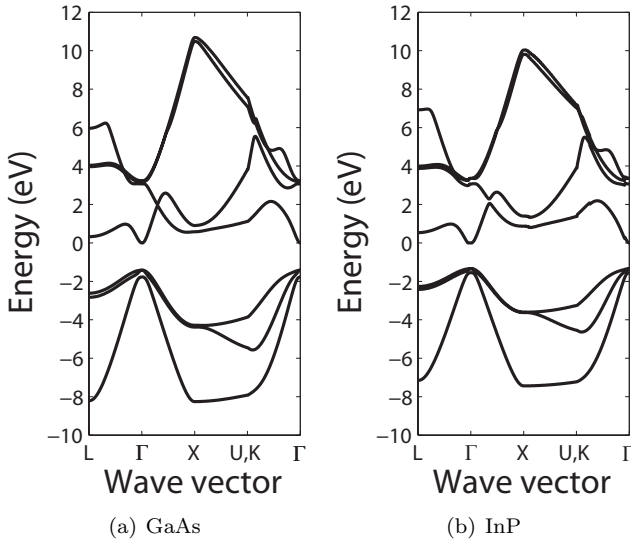


Figure 3.2: Full-band structures along the special path  $\Gamma$ -L-X-U/K- $\Gamma$  through the first Brillouin zone for GaAs and InP.

considerations in the reciprocal space. For example Bufler [63] groups the  $\mathbf{k}$ -points to valleys lying within a sphere around their minima. In this work, the  $\mathbf{k}$ -space grid cubes are allocated to particular valleys with a customized steepest descent method. This allocation method divides the reciprocal space into groups of  $\mathbf{k}$ -points according to the following algorithm. The starting point  $\mathbf{k}_{\text{start}}$  is a center point of the tensor grid given in Eq. (3.1). The next point  $\mathbf{k}_{\text{next}}$  lies in the next cubic box in the direction of the negative gradient at the center point of the current cube. If  $\mathbf{k}_{\text{next}}$  leaves the irreducible wedge during the iteration loop, it is transformed back again into the irreducible wedge. After a number of iterations, the end point  $\mathbf{k}_{\text{end}}$  is reached. All  $\mathbf{k}_{\text{end}}$  gather around the local energy minimum of the particular valley. A cubic box is allocated to the particular valley per conduction band where the customized steepest descent method converges to its valley minimum energy. The author does not expect relevant changes of the

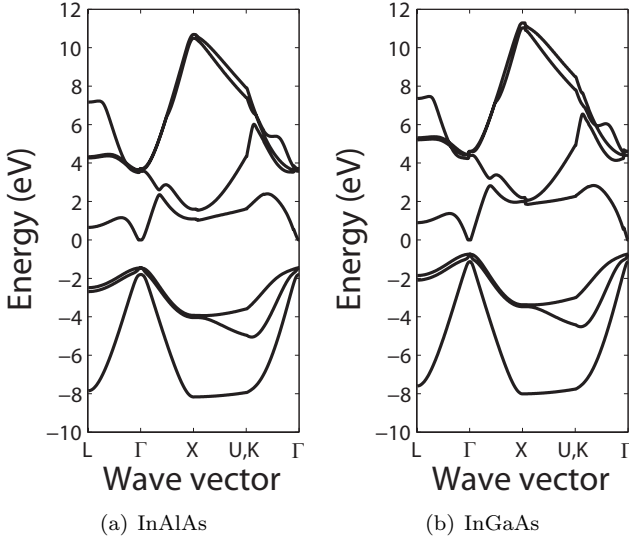


Figure 3.3: Full-band structures along the special path  $\Gamma$ -L-X-U/K- $\Gamma$  through the Brillouin zone for InAlAs and InGaAs.

MC simulation results due to the different valley allocation approaches used in literature. Holes possess only one local minimum per valence band rendering the valley allocation trivial:

$$\nu_n(\mathbf{k}) = \begin{cases} hh & \text{if } n = \text{heavy hole band,} \\ lh & \text{if } n = \text{light hole band,} \\ so & \text{if } n = \text{split-off band.} \end{cases} \quad (3.7)$$

Fig. 3.4 shows the evaluated valleys for the conduction bands of GaAs. The local minimum energies and  $\mathbf{k}_{\min}$ -points are computed based on the set of center and corner points of the cubic boxes. Tables C.3, C.4 and C.5 summarize the minima taken from the set of center and corner points of the  $\mathbf{k}$ -space grid. The nomenclature of the conduction band valley minima is as follows. The first four conduction band valleys are  $\Gamma_6$ ,  $L_6$ ,  $X_6$ , for the first conduction band, and  $X_7$  for the second conduction band. All other conduction band valleys are defined as

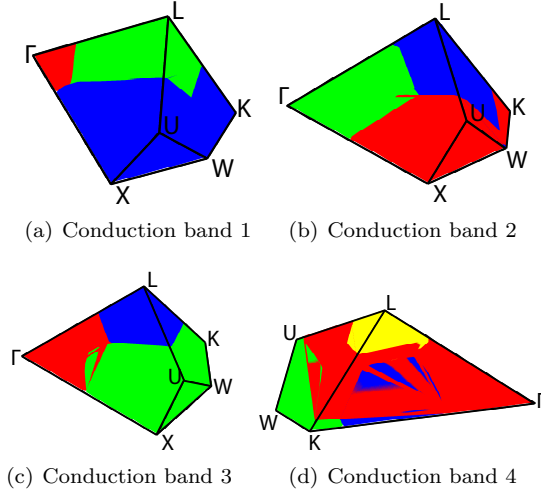


Figure 3.4: GaAs valley allocation for all conduction bands within the irreducible wedge of the first Brillouin zone. The plot shows the convex hulls of the cubic box center points within a valley for a discretization with  $N = 100$ . (a)  $\Gamma_6$  red,  $L_6$  green,  $X_6$  blue. (b)  $X_7$  red,  $c_{22}$  green,  $c_{23}$  blue. (c)  $c_{31}$  red,  $c_{32}$  green,  $c_{33}$  blue. (d)  $c_{41}$  red,  $c_{42}$  green,  $c_{43}$  blue,  $c_{44}$  yellow.

$c_{nm}$  where  $n$  is the conduction band number and where  $m$  is the valley number within  $n$ . The valleys are ordered with rising valley minimum energy within a band.

### 3.4 Density of States

The density of states is important for the computation of the scattering rates. The definition of the DOS in the  $\mathbf{k}$ -subspace volume  $V_\nu$  per spin is [29] (Eq. (5.31), p. 84)

$$\mathcal{D}_\nu(E(\mathbf{k})) = \frac{1}{V} \sum_{\mathbf{k}' \in V_\nu} \delta(E(\mathbf{k}) - E_\nu(\mathbf{k}')) \quad (3.8a)$$

$$= \frac{1}{(2\pi)^3} \int_{V_\nu} d^3k' \delta(E(\mathbf{k}) - E_\nu(\mathbf{k}')) \quad (3.8b)$$

with the volume of the crystal  $V$ . If  $\nu$  denotes a band index, then  $V_\nu$  is the volume of the first Brillouin zone. For  $\nu$  being a valley index,  $V_\nu$  is the volume of a valley. The total density of states is the sum over all possible  $\nu$ :

$$\mathcal{D}(E) = \sum_\nu \mathcal{D}_\nu(E). \quad (3.9)$$

Formulation (3.8b) of the DOS is impractical for numerical calculations because it requires a lot of energy eigenvalues  $E(\mathbf{k})$  to obtain a smooth DOS function. Therefore, the transformation of Eq. (3.8b) to a surface integral [58] (Eq. (2), p. 324) is used:

$$\mathcal{D}_\nu(E(\mathbf{k})) = \frac{2}{(2\pi)^3} \int_{E_\nu(\mathbf{k})=E(\mathbf{k})} \frac{dA}{|\nabla_{\mathbf{k}} E_\nu(\mathbf{k})|} \quad (3.10a)$$

$$\approx \sum_i \mathcal{D}_{\nu,i}(E) \quad (3.10b)$$

with the box DOS

$$\mathcal{D}_{\nu,i}(E) = \frac{2}{(2\pi)^3} \frac{A_{\nu,i}(E)w_i}{\hbar|\mathbf{v}_{\nu,i}|} \quad (3.11)$$

of the  $i$ th discretization cube including a factor of 2 by virtue of spin degeneracy. The sum runs over all cubes where their particular minimum and maximum box energies  $E_{\min}^{\text{box}}$  and  $E_{\max}^{\text{box}}$  obey  $E_{\min}^{\text{box}} \leq E = E(\mathbf{k}) \leq E_{\max}^{\text{box}}$ . Owing to computational efficiency, *CarloS* uses precomputed energy interval lists (see Chap. 6).  $A_{\nu,i}(E)$  is the area of the equi-energy surface defined by Eq. (3.6) cut with the cubic box (see App. B.3). If the energy  $E$  is not within the cube, the area is zero. As a result of the linear expansion of the equi-energy plane given in Eq. (3.6), the energy gradient is constant within a cube. Furthermore,  $w_i$  is the box weighting function defined by Eq. (3.5). Fig. 3.5 depicts the used full-band DOS for the first three conduction valleys and valence bands of GaAs. The nonparabolicities  $\bar{\alpha}$ , the effective masses at the valley bottom  $m^*$ , and the valley offset energies  $\Delta E$  are taken from Dunn et al. [56] (Table 3, p. 131) (see Table (B.1)).

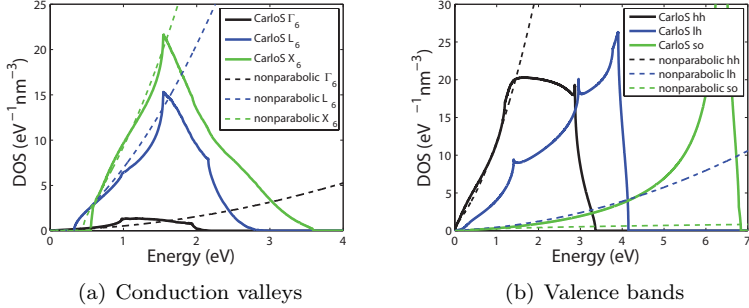


Figure 3.5: Comparison of single valley full-band DOS of GaAs with nonparabolic DOS (see Eq. (B.29)) with  $\Delta E_{\Gamma_6 L_6} = 0.323$  eV,  $\Delta E_{\Gamma_6 X_6} = 0.447$  eV, and  $\Delta E_{s_0} = 0.34$  eV.

Fig. 3.6 illustrates the DOS of higher conduction bands. Fig. 3.7 presents a comparison of the total conduction band DOS in GaAs. In literature, the total conduction band DOS for energies smaller than 2.5 eV match well with each other except for Fischetti88 [64]. In this energy range the main contribution to the DOS stems from the first conduction band. For higher energies the DOS deviates stronger indicating different underlying full-band structures especially for higher conduction bands.

For few 100 meV around the local valley minima of the conduction and valence bands the analytical nonparabolic expression (see Eq. (B.26)) describes the band structure well.

### 3.5 Direction-Weighted Density of States

In this work, the polar optical phonon scattering rate is proportional to a quantity called direction-weighted density of states:

$$\mathcal{D}_{q^{-2}, \nu}(\mathbf{k}) = \frac{2}{(2\pi)^3} \int_{V_{\text{BZ}}} d^3 k' \frac{1}{|\mathbf{q}|^2} \delta(E(\mathbf{k}') - E(\mathbf{k}) \mp E_{\text{trans}}(\mathbf{q})) \quad (3.12a)$$

$$\approx \sum_i \mathcal{D}_{q^{-2}, \nu, i}(\mathbf{k}) \quad (3.12b)$$



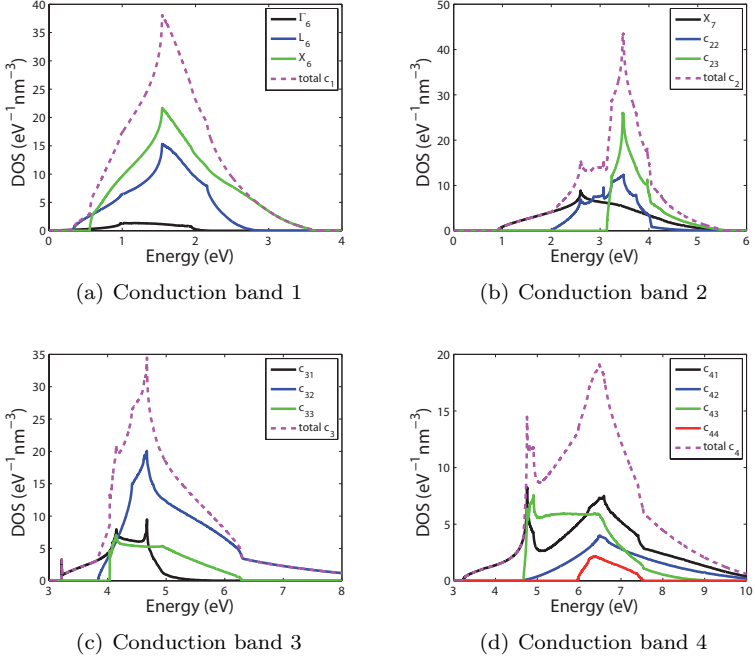


Figure 3.6: Density of states of conduction band valleys and conduction bands of GaAs.

with the phonon wave vector  $\mathbf{q} = \mathbf{k} - \mathbf{k}'$  and the direction-weighted box DOS

$$\mathcal{D}_{q^{-2},\nu,i}(\mathbf{k}) = \frac{\mathcal{D}_{\nu,i}(E(\mathbf{k}) \pm E_{\text{trans}}(\mathbf{q}))}{(\mathbf{k} - \mathbf{k}_{\text{cb}})^2}. \quad (3.13)$$

The factor 2 appears due to spin degeneracy. The sum runs over all cubes  $i$  obeying  $E_{\text{min}}^{\text{box}} \leq E = E(\mathbf{k}) \pm E_{\text{trans}}(\mathbf{q}) \leq E_{\text{max}}^{\text{box}}$ . Fig. 3.8 compares the numerically and analytically (see Eq. (B.30)) evaluated direction-weighted density of states of GaAs. The full-band expression is space-averaged. The full-band and analytical direction-weighted density of states are in good agreement for a few 100 meV above the valley minimum in which the difference of about 10 % stems from the neglect of the overlap integral in the numerical integration.

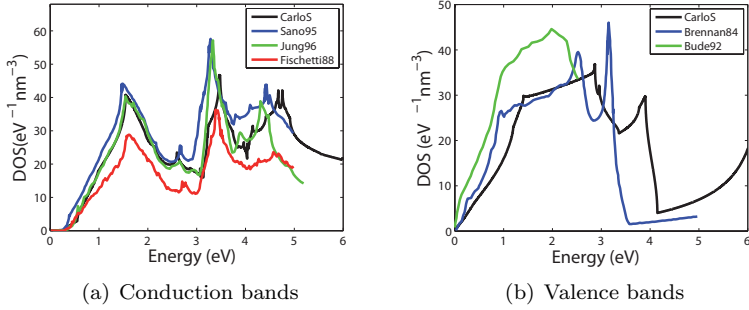


Figure 3.7: Comparison of the total DOS of GaAs computed in this work with other published results. (a) Comparison between *CarloS*, Sano95 [65], Jung96 [66], and Fischetti88 [64]. (b) Comparison between *CarloS*, Brennan84 [67], and Bude92 [68].

For higher energies the difference between the full-band and the non-parabolic density of states drives the similar energy dependency apart.

### 3.6 Density Of States Overlap Integral

The impact ionization scattering rate has a functional dependency according to a quantity called density of states overlap integral. For an impacting electron the function is given by [69] (Eqs. (11) and (12), p. 628)

$$\begin{aligned}
 \mathcal{D}_{ii}(E_c) = & \sum_{\substack{v',c',c'' \\ c'' \geq c'}} \int_0^{\hat{E}_{c'}} dE_{c'} \int_0^{\hat{E}_{v'}} dE_{v'} \mathcal{D}_{v'}(E_{v'}) \mathcal{D}_{c'}(E_{c'}) \\
 & \times \mathcal{D}_{c''}(E_c - E_{c'} - E_{v'} - E_g)
 \end{aligned} \tag{3.14}$$

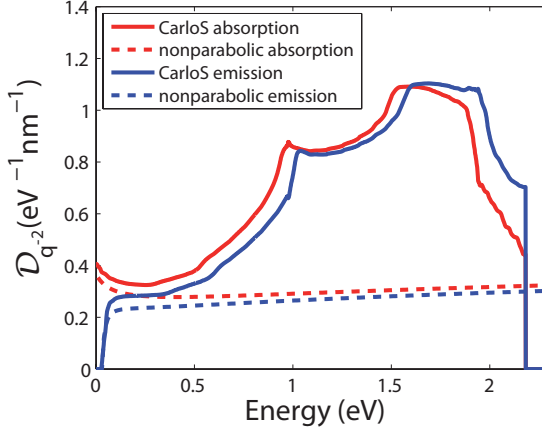


Figure 3.8: Comparison of full-band and analytical direction-weighted density of states for  $\Gamma_6$ -valley in GaAs.

and for an impacting hole it is

$$\mathcal{D}_{ii}(E_v) = \sum_{\substack{c',v',v'' \\ v'' \geq v'}} \int_0^{\hat{E}_{v'}} dE_{v'} \int_0^{\hat{E}_{c'}} dE_{c'} \mathcal{D}_{c'}(E_{c'}) \mathcal{D}_{v'}(E_{v'}) \quad (3.15)$$

$$\times \mathcal{D}_{v''}(E_v - E_{v'} - E_{c'} - E_g) .$$

Here, it is  $E_{c,c',v,v'} = E(\mathbf{k}_{c,c',v,v'})$ . Furthermore,  $E_g$  is the band gap energy. The upper integration boundaries are for an impacting electron

$$\hat{E}_{c'} = E_c(\mathbf{k}_c) - E_g \quad (3.16a)$$

$$\hat{E}_{v'} = E_c(\mathbf{k}_c) - E_{c'} - E_g \quad (3.16b)$$

and for an impacting hole

$$\hat{E}_{v'} = E_v(\mathbf{k}_v) - E_g \quad (3.17a)$$

$$\hat{E}_{c'} = E_v(\mathbf{k}_v) - E_{v'} - E_g . \quad (3.17b)$$

For the numerical computation the discretized version of Eq. (3.14)

$$\begin{aligned} \mathcal{D}_{\text{ii}}(E_c) = & \sum_{\substack{v',c',c'' \\ c'' \geq c'}} \sum_{i=0}^{i_{\max}^c} \sum_{j=0}^{j_{\max}^c} \mathcal{D}_{v'}(E_j) \Delta E_j \mathcal{D}_{c'}(E_i) \Delta E_i \\ & \times \mathcal{D}_{c''}(E_c - E_i - E_j - E_g) \end{aligned} \quad (3.18)$$

and of Eq. (3.15)

$$\begin{aligned} \mathcal{D}_{\text{ii}}(E_v) = & \sum_{\substack{c',v',v'' \\ v'' \geq v'}} \sum_{i=0}^{i_{\max}^v} \sum_{j=0}^{j_{\max}^v} \mathcal{D}_{c'}(E_j) \Delta E_j \mathcal{D}_{v'}(E_i) \Delta E_i \\ & \times \mathcal{D}_{v''}(E_v - E_i - E_j - E_g) \end{aligned} \quad (3.19)$$

are utilized with  $i_{\max}^c = \text{int}(\hat{E}_{c'}/\Delta E_i)$ ,  $j_{\max}^c = \text{int}(\hat{E}_{v'}/\Delta E_j)$ ,  $i_{\max}^v = \text{int}(\hat{E}_{v'}/\Delta E_i)$ , and  $j_{\max}^v = \text{int}(\hat{E}_{c'}/\Delta E_j)$ . Here, the function  $\text{int}()$  is used in the sense of a C++ type cast.

## 3.7 Particle Motion in Phase Space

As a result of the symmetry of the examined devices, a one-dimensional discretization of the real-space is sufficient. The z-direction of the real-space is discretized with a one-dimensional tensor grid and the reciprocal space with a three-dimensional equidistant tensor grid (see Sec. 3.1). For device simulations the electric field is precomputed with a commercial drift-diffusion solver [23]. Within a real-space discretization element, the electric field is constant. The energy gradient, and therefore the velocity, is constant within a reciprocal space discretization element. There are several time intervals until a particle reaches one kind of boundary [63] (p. 24):

- flight time to reach the boundary of a  $\mathbf{k}$ -space cubic box  $t_k$  (see App. B.4),
- time  $t_r$  till the border  $z_r$  of the real-space grid:  $t_r = z_r - z(t_0)/v_z$  (compare with Eq. (3.22)),

- time interval till the time step of the synchronous ensemble  $t_T = T - t$ .

The charge carrier propagates for the minimum of the four time intervals  $\Delta t = \min(t_s, t_k, t_r, t_T)$  [63] (Fig. (2.5), p. 26). If the time until a scattering event  $t_s$  is the minimum time interval, a scattering event and a final  $\mathbf{k}$ -state are selected randomly. Otherwise, it is allowed to stop the propagation at  $t_k, t_r, t_T < t_s$  and to start the algorithm again [70] (see Fig. 6.2). This propagation scheme allows an easier treatment of the flight time calculation without corrections [71] (Eq. (2.8), p. 652) due to a region-dependent  $\bar{\Gamma}(\boldsymbol{\xi})$ . Newton's second law governs the  $\mathbf{k}$ -space motion. The equation of motion is given by

$$\hbar \frac{d\mathbf{k}(t)}{dt} = q\mathbf{E}(\mathbf{r}(t)) . \quad (3.20)$$

As a result of the constant electric field during the propagation, the integrated equation of motion is

$$\mathbf{k}(t) = \mathbf{k}(t_0) + \frac{q}{\hbar}\mathbf{E}\Delta t \quad (3.21)$$

with  $\Delta t = t - t_0$  and the current time  $t_0$ . Owing to the small propagation time, which allows the disregard of the acceleration term [63] (Eq. (2.15), p. 25), and the constant velocity during the propagation, the real-space position is simply given by

$$\mathbf{r}(t) = \mathbf{r}(t_0) + \mathbf{v}\Delta t . \quad (3.22)$$

If the particle leaves the first Brillouin zone, the carrier is transformed back by means of an Umklapp process

$$\mathbf{k}_{\text{BZ}} = \mathbf{k} + \mathbf{G} \quad (3.23)$$

with a reciprocal lattice vector  $\mathbf{G}$  (see App. B.5).



# Chapter 4

## Scattering Mechanisms

The treatment of scattering mechanisms is the key ingredient of semiclassical transport theory. The balance of acceleration due to external fields and the dissipation owing to scattering disturbances governs the distribution function and the mean values.

Typically, semiclassical transport theory starts with Fermi's golden rule to compute the quantum mechanical scattering rate from an unperturbed initial  $|i\rangle$  to an unperturbed final state  $|f\rangle$ . A formulation of the matrix element in Eq. (2.6) is given in Jacoboni et al. [71] (Eq. (3.21), (3.28), p. 671, 672) (also compare with Hess et al. [2] p. 43):

$$|M|^2 = \left| \langle f | \hat{H}_p | i \rangle \right|^2 = \frac{(2\pi)^3}{V^2} \left| \sum_{\mathbf{q}} \langle c' | \tilde{H}_p(\mathbf{q}) | c \rangle \right|^2 \mathcal{G}(\mathbf{k}, \mathbf{k}') . \quad (4.1)$$

Here,  $|c\rangle$  and  $|c'\rangle$  describe the initial and the final state of the crystal. Furthermore,  $\hat{H}_p$  is the perturbation operator and  $\tilde{H}_p$  is its Fourier transform. The overlap integral [71] (Eq. (3.29), p. 672) over the unit cell volume  $V_{\text{cell}}$  is given by

$$\mathcal{G}(\mathbf{k}, \mathbf{k}') = \left| \int_{V_{\text{cell}}} d^3r u_{\mathbf{k}'}^* u_{\mathbf{k}} \exp(i\mathbf{G}\mathbf{r}) \right|^2 \quad (4.2)$$

with the periodic part of the Bloch wave function  $u_{\mathbf{k}}$ . The forms of  $\hat{H}_p$  and  $\tilde{H}_p$  for the particular scattering mechanisms are discussed in literature [2, 28, 30, 71, 72, 73, 74, 75, 76, 77, 78].

This work follows the density of states ansatz of Tang et al. [79] fulfilling computational efficiency [1]. The transition rates, except polar optical phonon scattering, have the computationally efficient form [1] (Eq. (9), p. 873)

$$W_{\nu\nu'}(\mathbf{k}, \mathbf{k}') = \frac{\Lambda_{\nu\nu'}(E(\mathbf{k}))}{V} \delta(E_{\nu'}(\mathbf{k}') - E_{\nu}(\mathbf{k}) \mp E_{\text{trans}}) . \quad (4.3)$$

$\Lambda_{\nu\nu'}$  is an energy-dependent prefactor, which is allowed to vary with the initial energy. Summing Eq. (4.3) over  $\mathbf{k}'$  leads to a scattering rate being directly proportional to the density of final states and a function of the initial energy (compare with Eq. (3.8a))

$$W_{\nu\nu'}(E) = \Lambda_{\nu\nu'}(E) \mathcal{D}_{\nu'}(E_{\nu} \pm E_{\text{trans}}) . \quad (4.4)$$

The states after scattering are equally distributed on an equi-energy surface in a given band or valley. An efficient selection of the final reciprocal state is possible [1] (p. 873).

## 4.1 Carrier-Phonon Scattering

For carrier-phonon scattering expression (4.1) evaluates to [74] (Eq. (3.14), p. 85)

$$|M|^2 = \frac{\hbar}{2N_{\text{cell}}\bar{M}} \frac{C_{\tilde{b}}(\mathbf{k}, \mathbf{k}')\mathcal{G}(\mathbf{k}, \mathbf{k}')}{\omega_{\tilde{b}}(\mathbf{q})} \left( n(\omega_{\tilde{b}}(\mathbf{q})) + \frac{1}{2} \mp \frac{1}{2} \right) \delta_{\mathbf{k}\pm\mathbf{q}-\mathbf{k}', \mathbf{G}} \quad (4.5)$$

with the number of unit cells  $N_{\text{cell}}$ , the oscillator mass  $\bar{M}$ , the coupling strength  $C_{\tilde{b}}(\mathbf{k}, \mathbf{k}')$ , the phonon branch  $\tilde{b}$ , the phonon angular frequency  $\omega_{\tilde{b}}(\mathbf{q})$ , and the phonon occupation number  $n(\omega_{\tilde{b}}(\mathbf{q}))$ . The upper signs correspond to phonon absorption and the lower signs stand for phonon emission. The transition energy is  $E_{\text{trans}} = \hbar\omega_{\tilde{b}}(\mathbf{q})$ .



Usually, the phonon occupation number is taken to be that for thermodynamic equilibrium following Bose-Einstein statistics [30] (Eq. (6.3), p. 373)

$$n_{\tilde{b}}(\mathbf{q}) = \frac{1}{\exp\left(\frac{\hbar\omega_{\tilde{b}}(\mathbf{q})}{k_B T}\right) - 1} \quad (4.6)$$

with the Boltzmann constant  $k_B$  and the lattice temperature  $T$ . The momentum-conserving  $\delta$ -function  $\delta_{\mathbf{k}\pm\mathbf{q}-\mathbf{k}',\mathbf{G}}$  is no constraint because a suitable  $\mathbf{k}$ -state is always found due to the utilized phonon dispersion approximations. The term  $C_{\tilde{b}}(\mathbf{k}, \mathbf{k}')\mathcal{G}(\mathbf{k}, \mathbf{k}')$  dictates the selection rules [74] (p. 85). The factor  $C_{\tilde{b}}(\mathbf{k}, \mathbf{k}')$  is a tedious quantity that contains the concept of a deformation potential [80,81]. Owing to the laborious theoretical treatment of the deformation potential [2,82,83], the usage of empirical simplifications is common practice in the community of Monte Carlo modeling of semiclassical charge transport [55]. Deformation potentials are tuned to experimental data [55]. In energy band dependent parts of the Brillouin zone the deformation potential can be approximated as a constant, which does neither depend on the initial nor on the final  $\mathbf{k}$ -state or energy [55] (p. 815). Such a partitioning of  $W(\mathbf{k}, \mathbf{k}')$  into regional constant deformation potentials allows an efficient evaluation of the scattering rates (compare with Sec. 4.6.2). The main features of the scattering rate stem from the density of final states and less due to the matrix element. Tang et al. [79] introduced the density of states ansatz. Years later, the evaluation of the matrix element, employing phonon models, Refs. [2, 55, 62, 82, 83, 84] have shown the adequacy of that constant matrix approximation. This work follows the density of states ansatz and the transition rates according to Jacoboni et al. [71], Fischetti et al. [64] and Jungemann et al. [29].

Summing up the phonon transition rates  $W_{\tilde{b}nn'}(\mathbf{k}, \mathbf{k}')$  over all final states  $\mathbf{k}'$ , final bands  $n'$ , and phonon branches  $\tilde{b}$  yields the phonon scattering rate

$$W_n(\mathbf{k}) = \sum_{\mathbf{k}', n', \tilde{b}} W_{\tilde{b}nn'}(\mathbf{k}, \mathbf{k}') . \quad (4.7)$$

### 4.1.1 Elastic Acoustic Phonon Scattering

The coupling strength for acoustic phonons is given by [71] (Eq. (3.35), p. 673) [30] (p. 436)

$$C_{\tilde{b}}(\mathbf{k}, \mathbf{k}') = (\tilde{\Xi}\mathbf{q}\zeta)^2 \quad (4.8)$$

with the acoustic phonon deformation potential  $\tilde{\Xi}$  and the phonon polarization vector  $\zeta$ . The scalar product  $\mathbf{q}\zeta$  limits the contribution to longitudinal phonon modes. For a discussion of contributions of transversal modes due to elastic anisotropies the author refers to Ridley [74] (p. 94). The dispersion of acoustic phonons for intravalley transitions is modeled with the Debye approximation [85] (p. 458)

$$\omega_{\tilde{b}}(\mathbf{q}) = u_l q \quad (4.9)$$

with the longitudinal sound velocity  $u_l$ . Then, the phonon occupation number becomes [71] (Eq. (3.44), p. 674)

$$n_{\tilde{b}}(\mathbf{q}) \approx \frac{k_B T}{\hbar q u_l} - \frac{1}{2}. \quad (4.10)$$

The intravalley acoustic phonon energy is small compared to the carrier energies rendering  $E_{\text{trans}} = 0$  reasonable [71] (p. 673 and 674). This means that there is no exchange of energy with the thermal phonon bath for low temperatures and low electric fields. Scattering with intravalley acoustic phonons has a transition rate [71] (Eq. (3.46), p. (674)) of

$$W_{\text{ac}}(\nu, \mathbf{k} | \nu', \mathbf{k}') = \frac{2\pi k_B T \Xi_{\nu}^2}{\hbar V u_l^2 \rho} \delta(E_{\nu'}(\mathbf{k}') - E_{\nu}(\mathbf{k})) \delta_{\nu_n(\mathbf{k}), \nu'_n(\mathbf{k}')} \quad (4.11)$$

with  $N_{\text{cell}} \bar{M} = \rho V$ , the mass density of the semiconductor material  $\rho$ , the effective acoustic phonon deformation potential  $\Xi = \tilde{\Xi}\mathcal{G}$  including the effect of the overlap integral, and the valley allocation  $\nu_n(\mathbf{k})$  defined in Sec. 3.3. The elastic, energy-equipartition approximation renders the prefactor to be a constant with respect to energy, fulfilling Eq. (4.3). The scattering rate evaluates to

$$W_{\text{ac}}(\nu, E) = \frac{\pi k_B T \Xi_{\nu}^2}{\hbar u_l^2 \rho} \mathcal{D}_{\nu}(E) \quad (4.12)$$

with the density of final states  $\mathcal{D}_\nu(E)$  including spin degeneracy. Fig. 4.1 illustrates the elastic acoustic phonon scattering rates for electrons and holes in GaAs.

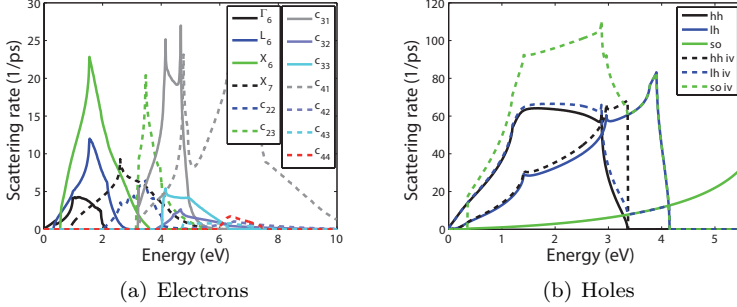


Figure 4.1: Elastic acoustic phonon scattering rates of GaAs. (a) Electron intravalley acoustic phonon scattering rates for conduction valleys. (b) Hole intra- and intervalley (iv) acoustic phonon scattering rates for valence bands.

### 4.1.2 Nonpolar Optical Phonon Scattering

The coupling strength for nonpolar optical phonons is given by [30] (p. 436) [74] (p. 106 ff.)

$$C_{\bar{b}}(\mathbf{k}, \mathbf{k}') = (\tilde{D}\mathbf{n}_1\boldsymbol{\zeta})^2 \quad (4.13)$$

with the nonpolar optical phonon deformation potential  $\tilde{D}$  and an unit vector  $\mathbf{n}_1$  pointing in the direction from the Brillouin zone center to a valley minimum. Concerning the contribution of different phonon branches, the author refers to Ridley [74] (p. 107) and the references therein. Usually, MC codes use an effective coupling strength with one single mode frequency [74] (Eq. (3.120), p. 108). Using the Einstein approximation for the optical phonon dispersion [85] (p. 462)  $\omega_{\bar{b}}(\mathbf{q}) = \omega_{\text{op}} = \text{const}$ , which neglects the dependence of the optical phonon angular frequency  $\omega_{\text{op}}$  on the phonon wave vector, the transition rate

for intravalley nonpolar optical phonon scattering evaluates to [71] (Eq. (3.71), p. 678)

$$\begin{aligned}
 W_{\text{npop}}^{\text{abs/em}}(\nu, \mathbf{k} | \nu', \mathbf{k}') &= \frac{\pi D_\nu^2}{\rho V \omega_{\text{op}}} \left( n_{\text{op}} + \frac{1}{2} \mp \frac{1}{2} \right) \\
 &\times \delta(E_{\nu'}(\mathbf{k}') - E_\nu(\mathbf{k}) \mp \hbar \omega_{\text{op}}) \\
 &\times \delta_{\nu_n(\mathbf{k}), \nu'_{n'}(\mathbf{k}')} .
 \end{aligned} \tag{4.14}$$

Here,  $D = \tilde{D}\mathcal{G}$  is the effective nonpolar optical deformation potential, which includes the effect of the overlap integral, and  $n_{\text{op}}$  is the thermal equilibrium occupation number of optical phonons. The scattering rate for nonpolar optical phonon scattering computes to

$$W_{\text{npop}}^{\text{abs/em}}(\nu, E) = \frac{\pi D_\nu^2}{2\rho\omega_{\text{op}}} \left( n_{\text{op}} + \frac{1}{2} \mp \frac{1}{2} \right) \mathcal{D}_\nu(E \pm \hbar\omega_{\text{op}}) \tag{4.15}$$

where the final density of states  $\mathcal{D}_\nu(E \pm \hbar\omega_{\text{op}})$  includes spin degeneracy. The prefactor does not depend on a reciprocal space vector, fulfilling Eq. (4.3). Figs. 4.2 and 4.3 display the nonpolar optical phonon scattering rates for electrons and holes in GaAs.

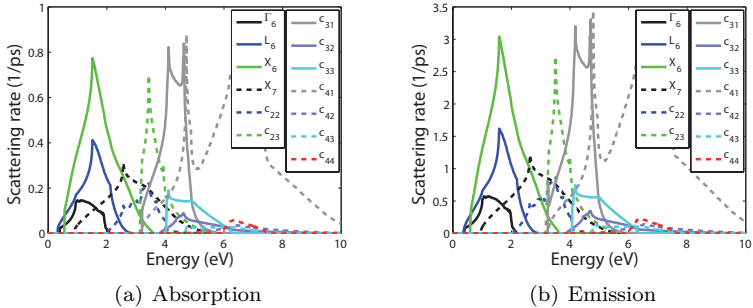


Figure 4.2: Electron nonpolar optical phonon scattering rates of GaAs with  $\hbar\omega_{\text{op}} = 35.36$  meV.

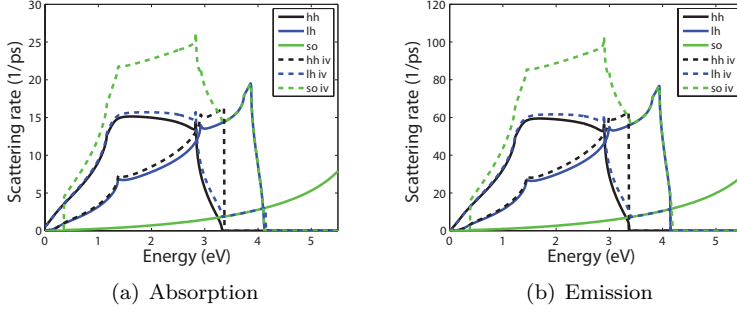


Figure 4.3: Hole nonpolar optical phonon scattering rates of GaAs (iv: intervalley).

### 4.1.3 Polar Optical Phonon Scattering

The coupling strength of polar optical phonons is given by [74] (p. 114 ff.)

$$C_b(\mathbf{k}, \mathbf{k}') = \frac{e^2 \omega_{\text{op}}^2 \bar{M}}{V_{\text{cell}} |\mathbf{q}|^2} \left( \frac{1}{\epsilon_{\infty}} - \frac{1}{\epsilon_0} \right) \quad (4.16)$$

with the unit cell volume  $V_{\text{cell}}$  and the phonon wave vector  $\mathbf{q}$ , which is given by  $\mathbf{k}' = \mathbf{k} \mp \mathbf{q} + \mathbf{G}$ . The relation between the optical and static dielectric permittivity  $\epsilon_{\infty}$  and  $\epsilon_0$ , and the optical and static dielectric constant  $\kappa_{\infty}$  and  $\kappa_0$  is given by

$$\epsilon_{\infty} = 4\pi\epsilon_0\kappa_{\infty} \quad (4.17a)$$

$$\epsilon_0 = 4\pi\epsilon_0\kappa_0 \quad (4.17b)$$

with the vacuum permittivity  $\epsilon_0$ . Polar optical phonon scattering has only contributions from longitudinal modes [74] (p. 113). The dispersion relation of optical phonons follows the Einstein approximation. The intraband polar optical phonon scattering rate is given by [64] (Eq. (5), p. 9725)

$$W_{\text{pop}}^{\text{abs/em}}(n, \mathbf{k}) = \frac{2\pi}{\hbar} \sum_{\mathbf{q}} \frac{e^2 F^2}{\mathbf{q}^2} \left( n_{\text{op}} + \frac{1}{2} \mp \frac{1}{2} \right) \mathcal{G}(\mathbf{k}, \mathbf{k}')$$

$$\begin{aligned} & \times \delta(E_{n'}(\mathbf{k}') - E_n(\mathbf{k}) \mp \hbar\omega_{\text{op}}) \delta_{n,n'} \quad (4.18\text{a}) \\ & = \frac{2\pi}{\hbar} e^2 F^2 (n_{\text{op}} + \frac{1}{2} \mp \frac{1}{2}) \mathcal{D}_{q^{-2},n}(\mathbf{k}) \quad (4.18\text{b}) \end{aligned}$$

with  $V = N_{\text{cell}} V_{\text{cell}}$ . The polar coupling constant  $F$  in the Fröhlich expression is given by [64] (p. 9725)

$$F^2 = \frac{\hbar\omega_{\text{op}}}{4} \left( \frac{1}{\epsilon_{\infty}} - \frac{1}{\epsilon_0} \right). \quad (4.19)$$

Here,  $\mathcal{D}_{q^{-2},n}(\mathbf{k})$  is the direction-weighted DOS for the  $n$ th band (compare with Sec. 3.5). The overlap integral is set to unity leading to a slight overestimation of the polar optical phonon scattering rate. The summation over  $\mathbf{q}$  goes over all possible final states within the same band. Therefore, polar optical phonon scattering leads to a weak intervalley coupling. The electron interband transitions caused by polar optical phonons are neglected. Due to computational efficiency, the

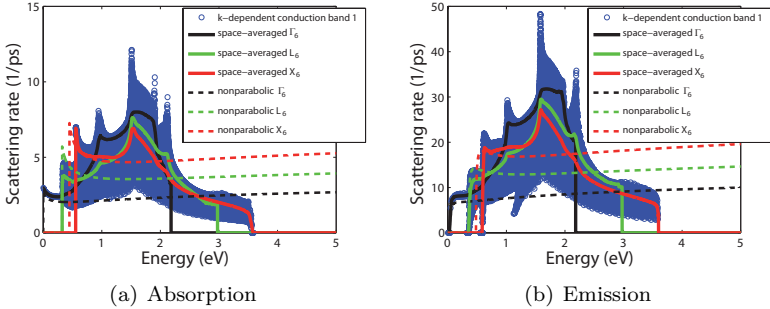


Figure 4.4: Full-band  $\mathbf{k}$ -dependent, full-band space-averaged, and nonparabolic polar optical phonon scattering rates of the first conduction band in GaAs vs. the energy.

anisotropic polar optical phonon scattering rate is averaged according to [64] (p. 9729)

$$W(E) = \frac{1}{\mathcal{D}(E)} \sum_{\mathbf{k}} W(\mathbf{k}) \delta(E(\mathbf{k}) - E) \quad (4.20)$$

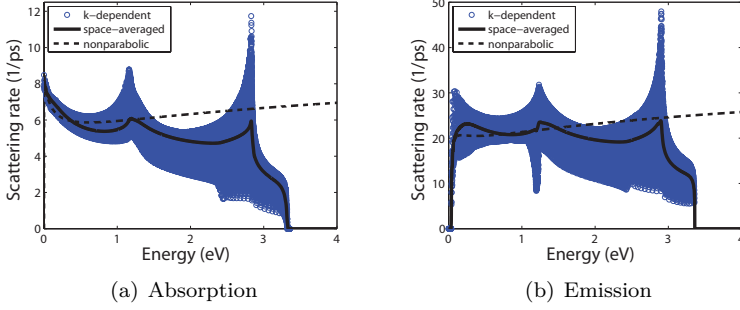


Figure 4.5: Full-band  $\mathbf{k}$ -dependent, full-band space-averaged, and nonparabolic polar optical phonon scattering rates of the heavy hole band in GaAs vs. the energy.

with the initial density of states  $\mathcal{D}(E)$ . Figs. 4.4 and 4.5 present the full-band  $\mathbf{k}$ -dependent polar optical phonon scattering rates of GaAs and compare them with the space-averaged and the analytical rates evaluated with the nonparabolic band structure. The nonparabolic parameters are taken from Dunn et al. [56] (Table 3, p. 131) (see Table B.1). Figs. 4.6 and 4.7 display the  $\mathbf{k}$ -space-averaged polar optical phonon scattering rates partitioned into contributions from the single conduction band valleys and valence bands in GaAs.

#### 4.1.4 Intervalley Phonon Scattering

In principle, every scattering mechanism couples different valleys among each other. The contributions of acoustic and nonpolar optical phonon modes are tied to a single intervalley phonon scattering mechanism. The hole interband transitions are treated individually. For an intervalley transition of an electron from a conduction band valley with its minimum at  $\mathbf{k}_{\min,\nu}$  into a valley with  $\mathbf{k}_{\min,\nu'}$  the involved phonon wave vector is close to  $\mathbf{k}_{\min,\nu'} - \mathbf{k}_{\min,\nu} \approx \mathbf{q}_{\nu\nu'}$ . Because the variation of  $\mathbf{q}_{\nu\nu'}$  is small, the involved phonon energy for a phonon branch is almost constant [71] (p. 678). Formally, electron intervalley

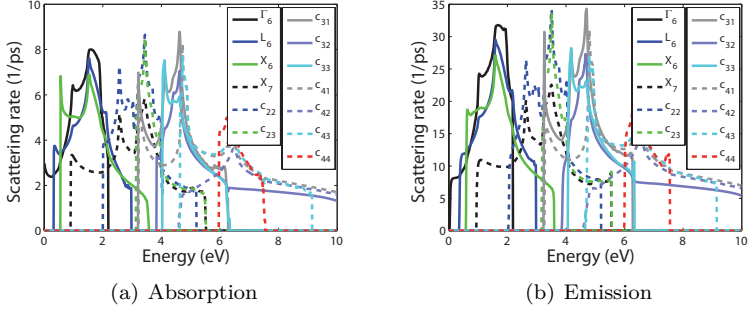


Figure 4.6: Space-averaged polar optical phonon scattering rates for the conduction band valleys of GaAs.

scattering is treated like the intravalley nonpolar optical phonon scattering (compare with Sec. 4.1.2). The transition rate for intervalley phonon scattering is given by [71] (Eq. (3.74), p. 679)

$$W_{iv}^{\text{abs/em}}(\nu, \mathbf{k}|\nu', \mathbf{k}') = \frac{\pi D_{\nu\nu'}^2}{\rho V \omega_{\nu\nu'}} \left( n_{\nu\nu'} + \frac{1}{2} \mp \frac{1}{2} \right) \times \delta(E_{\nu'}(\mathbf{k}') - E_{\nu}(\mathbf{k}) \mp \hbar\omega_{\nu\nu'} - \Delta E_{\nu\nu'}) \quad (4.21)$$

with the effective intervalley deformation potential  $D_{\nu\nu'} = \tilde{D}_{\nu\nu'} \mathcal{G}$  including the overlap integral, the intervalley deformation potential  $\tilde{D}_{\nu\nu'}$ , the intervalley phonon angular frequency  $\omega_{\nu\nu'}$  (see Table C.10), the intervalley phonon occupation number  $n_{\nu\nu'}$ , and the energy difference between the two valley minimum energies  $\Delta E_{\nu\nu'}$  (compare with Tables C.3 and C.4). The author computes the effective intervalley deformation potentials owing to contributions from acoustic and non-polar optical transitions according to [64] (p. 9732)

$$\tilde{D}_{\nu\nu'} = \sqrt{|\Xi \mathbf{q}_{\nu\nu'}|^2 + D^2} \quad (4.22)$$

with the phonon wave vector connecting the energy minima of valley  $\nu$  and  $\nu'$ . Tables C.3 and C.4 show the computed minimum positions  $\mathbf{k}_{\min}^{\text{wedge}}$  in the irreducible wedge. 48-fold transformation of  $\mathbf{k}_{\min}^{\text{wedge}}$  into the first Brillouin zone leads to a number of equivalent valleys and,



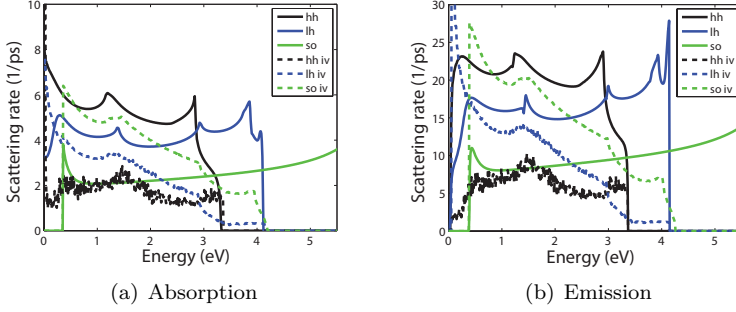


Figure 4.7: Space-averaged intra- and intervalley (iv) polar optical phonon scattering rates for the valence bands of GaAs.

hence, different possibilities for the  $\mathbf{q}_{\nu\nu'}^2$ . The effective intervalley deformation potential from valley  $\nu$  to valley  $\nu'$  is the mean value of all possible equivalent transitions. Tables C.6, C.7, C.8, and C.9 present the computed effective intervalley deformation potentials for GaAs, InP, InAlAs, and InGaAs.

The summation over all final states  $\mathbf{k}'$  leads to the electron intervalley phonon scattering rate

$$W_{\text{iv}}^{\text{abs/em}}(\nu, \nu', E) = \frac{\pi D_{\nu\nu'}^2}{2\rho\omega_{\nu\nu'}} \left( n_{\nu\nu'} + \frac{1}{2} \mp \frac{1}{2} \right) \mathcal{D}_{\nu'}(E \pm \hbar\omega_{\nu\nu'} - \Delta E_{\nu\nu'}) . \quad (4.23)$$

The final density of states  $\mathcal{D}_{\nu'}(E \pm \hbar\omega_{\nu\nu'} - \Delta E_{\nu\nu'})$  accounts for the number of equivalent final valleys (see App. C.2 and Table C.11) and spin degeneracy. Fig. 4.8 illustrates the sum of the absorption and the emission electron intervalley scattering rates owing to acoustic and nonpolar optical phonon transitions in GaAs. Polar optical phonons additionally couple weakly valleys among each other in the approach of this work.

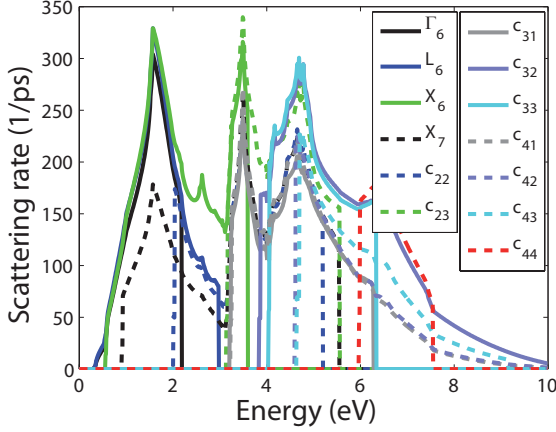


Figure 4.8: Sum of the absorption and the emission intervalley scattering rates for electrons in GaAs.

## 4.2 Impact Ionization Scattering

Impact ionization is an electron-electron interaction process. A high-energy carrier is able to generate a new electron-hole pair by lifting an electron from the valence band into the conduction band. The transition probability follows from Fermi's golden rule. For a primary impacting electron the impact ionization scattering rate is given by [69] (Eq. (1), p. 626)

$$\begin{aligned}
 W_{ii}(\mathbf{k}_c) &= \frac{2\pi}{\hbar} \sum_{\substack{v',c',c'' \\ c'' \geq c'}} \sum_{\mathbf{k}_{v'}, \mathbf{k}_{c'}, \mathbf{k}_{c''}} |M_{ii}|^2 \\
 &\times \delta(E_c(\mathbf{k}_c) - E_{c'}(\mathbf{k}_{c'}) - E_{c''}(\mathbf{k}_{c''}) - E_{v'}(\mathbf{k}_{v'}) - E_g) \\
 &\times \delta_{\mathbf{k}_c, \mathbf{k}_{v'} + \mathbf{k}_{c'} + \mathbf{k}_{c''} + \mathbf{G}}
 \end{aligned} \tag{4.24}$$

with the double Coulomb impact ionization matrix element  $M_{ii}$  and the sum over all possible final states and conduction  $c$  and valence bands  $v$ . Here,  $E_c$  and  $E_v$  denote the full-band energy of electrons and holes, respectively. Furthermore,  $E_g$  is the band gap energy.

Swapping  $c$  and  $v$  in Eq. (4.24) leads to the scattering rate for a primary impacting hole. In first principle approaches,  $|M_{ii}|^2 = |M_d|^2 + |M_e|^2 + |M_d - M_e|^2$  is calculated with the direct term  $M_d$ , the exchange term  $M_e$ , and the Coulomb interaction potential  $V(\mathbf{r}_1, \mathbf{r}_2)$  according to [66] (Eqs. (9)-(11), p. 2476)

$$M_d = \int \int d^3\mathbf{r}_1 d^3\mathbf{r}_2 \Psi_{1'}^*(\mathbf{r}_1) \Psi_{2'}^*(\mathbf{r}_2) V(\mathbf{r}_1, \mathbf{r}_2) \Psi_1(\mathbf{r}_1) \Psi_2(\mathbf{r}_2) \quad (4.25a)$$

$$M_e = \int \int d^3\mathbf{r}_1 d^3\mathbf{r}_2 \Psi_{2'}^*(\mathbf{r}_1) \Psi_{1'}^*(\mathbf{r}_2) V(\mathbf{r}_1, \mathbf{r}_2) \Psi_1(\mathbf{r}_1) \Psi_2(\mathbf{r}_2) . \quad (4.25b)$$

Here,  $\Psi_{1,2}$  and  $\Psi_{1',2'}$  denote the wave functions of the initial and the final state, respectively. The impact ionization scattering rate is calculated using the random- $\mathbf{k}$  approximation (RKA) [69], which ignores momentum conservation. Dropping the restriction of momentum conservation leads to an upper bound estimation of the impact ionization scattering rate. The inclusion of the unities  $1 = \int_0^\infty dE_{c'} \delta(E_{c'} - E_{c'}(\mathbf{k}_{c'}))$  and  $1 = \int_0^\infty dE_{v'} \delta(E_{v'} - E_{v'}(\mathbf{k}_{v'}))$  [86] into Eq. (4.24) and the following summation over  $\mathbf{k}_{c'}$  and  $\mathbf{k}_{v'}$  yields the impact ionization scattering rate in the RKA and constant matrix approximation (CMA). The impact ionization scattering rate is dominated by the single particle DOS. Comparing Kane's RKA with first principle impact ionization evaluation methods, the RKA- and CMA-based impact ionization rates provide good results [69] (p. 628) [87] (p. 43) [55] (p. 818) (compare with Sec. 4.6.2).

For a primary impacting electron the rate is [69] (Eq. (12), p. 628) [88] (Eq. (3), p. 24)

$$W_{ii}(E_c(\mathbf{k}_c)) = \Lambda_e^{ii} \mathcal{D}_{ii}(E_c) \quad (4.26)$$

and for a primary impacting hole the impact ionization scattering rate is given by

$$W_{ii}(E_v(\mathbf{k}_v)) = \Lambda_h^{ii} \mathcal{D}_{ii}(E_v) . \quad (4.27)$$

Here, the  $\mathcal{D}_{ii}$  are the density of states overlap integrals defined in Eqs. (3.14) and (3.15), and the prefactors  $\Lambda^{ii}$  including the averaged matrix element  $M_{ii}$ :

$$\Lambda^{ii} = \frac{2\pi}{\hbar} |M_{ii}|^2 \frac{V^3}{N_{\text{cell}}} . \quad (4.28)$$

In the RKA and CMA the impact ionization prefactors  $\Lambda_e^{ii}$  and  $\Lambda_h^{ii}$  are treated as fit parameters, which are tuned to experimental data. Fig. 4.9 displays a comparison of impact ionization scattering rates

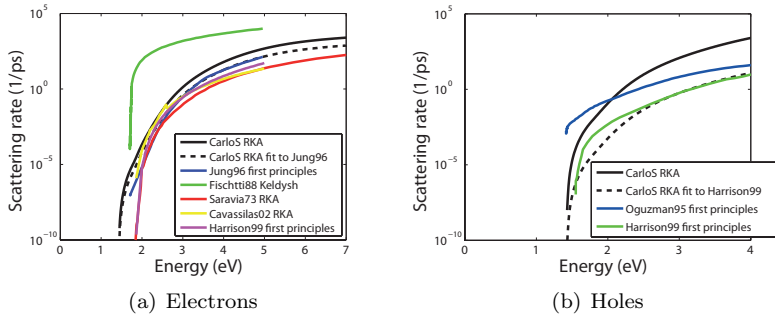


Figure 4.9: Comparison of impact ionization rates for primary impacting electrons and holes in GaAs. (a) Comparison between electron impact ionization rates calculated with RKA-based methods (*CarloS*, Saravia73 [89], Cavassilas02 [90]), first principle approaches (Jung96 [66], Harrison99 [91]) and the Keldysh approximation (Fischetti88 [64]). (b) Comparison between hole impact ionization rates calculated with RKA-based approaches (*CarloS*) and ab initio methods (Oguzman95 [92], Harrison99 [91]).

being based on different computation methods. The GaAs impact ionization scattering rates show less variation for electron rates than for holes rates in literature. Immediately before an impact ionization event, the carrier has a specific energy and resides in a certain valley. Fig. 4.10 presents the simulated distribution of the energy and the valley immediately before an impact ionization event occurs. Mainly, electrons impact-ionize with energies ranging from 3 eV to 5 eV residing in valleys of the second conduction band. Holes mostly ionize from the light hole band with energies between 2 eV and 3 eV.

The secondary carrier energies after impact ionization are computed by means of the random- $\mathbf{k}$  approximation [69] (p. 629) too. The secondary distribution function  $W_{ee}$  for a primary electron with

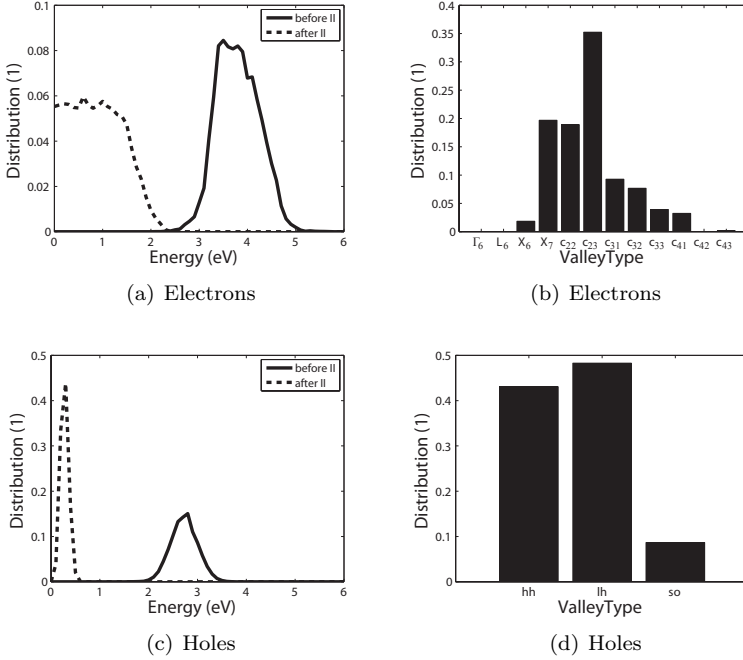


Figure 4.10: Distribution of impact ionization (II) events in GaAs depending on the energy and the valley type just before the impact ionization.

the energy  $E_c$  and a secondary electron with the energy  $E'_c$  is given by [69] (Eq. (17), p. 629)

$$\begin{aligned}
 W_{ee}(E_c, E'_c) &= \frac{2}{\mathcal{D}_{ii}(E_c)} \sum_{\substack{v', c', c'' \\ c'' \geq c'}} \mathcal{D}_{c'}(E'_c) \\
 &\times \int_0^{E_c - E'_{c'} - E_g} dE_{v'} \mathcal{D}_{v'}(E_{v'}) \mathcal{D}_{c''}(E_c - E'_{c'} - E_{v'} - E_g) .
 \end{aligned} \tag{4.29}$$

For a primary hole having the energy  $E_v$  and a secondary hole with the energy  $E'_v$  the secondary carrier energy distribution function is [69] (Eq. (18), p. 629)

$$\begin{aligned}
 W_{\text{hh}}(E_v, E'_v) &= \frac{2}{\mathcal{D}_{\text{ii}}(E_v)} \sum_{\substack{c', v', v'' \\ v'' \geq v'}} \mathcal{D}_{v'}(E'_{v'}) \\
 &\times \int_0^{E_v - E'_{v'} - E_g} dE_{c'} \mathcal{D}_{c'}(E_{c'}) \mathcal{D}_{v''}(E_v - E'_{v'} - E_{c'} - E_g) .
 \end{aligned} \tag{4.30}$$

$W_{\text{ee}}$  and  $W_{\text{hh}}$  are normalized to 2 because the secondary particles are indistinguishable. Application of the rejection technique to Eqs. (4.29) and (4.30) generates the random variables  $E'_c$  and  $E'_v$  for given primary energies  $E_c$  and  $E_v$ . Fig. 4.11 shows the secondary carrier energy distribution function  $W_{\text{ee}}(E_c, E'_c)$  of GaAs. Negative energies correspond to secondary holes. By reason of computational efficiency,

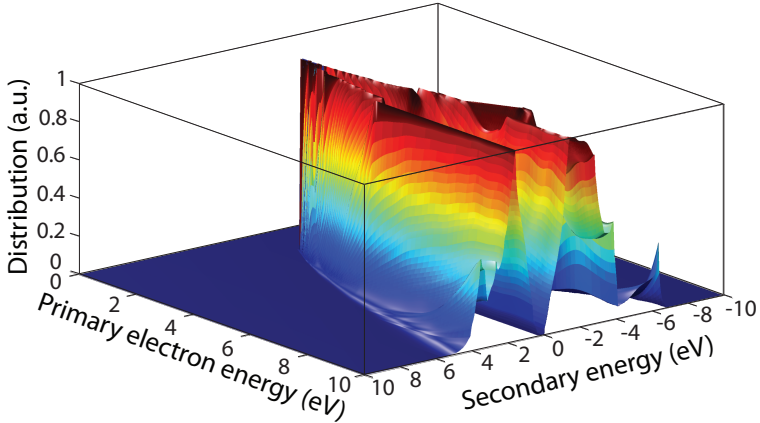


Figure 4.11: Secondary carrier energy distribution function  $W_{\text{ee}}(E_c, E'_c)$  computed using the random- $\mathbf{k}$  approximation for an impacting electron in GaAs. The negative energies correspond to secondary holes.

the author uses the mean value of the secondary energy distributions:

$$\langle E'_c \rangle(E_c) = \sum_{E'_c} W_{ee}(E_c, E'_c) E'_c \quad (4.31)$$

and

$$\langle E'_v \rangle(E_v) = \sum_{E'_v} W_{hh}(E_v, E'_v) E'_v . \quad (4.32)$$

For a primary impacting electron the secondary carrier energies for the two electrons  $E'_{e1}$ ,  $E'_{e2}$  and the single hole  $E'_h$  are chosen according to

$$E'_{e1} = \langle E'_c \rangle(E_c) r \quad (4.33a)$$

$$E'_{e2} = \langle E'_c \rangle(E_c) - E'_{e1} \quad (4.33b)$$

$$E'_h = E_c - \langle E'_c \rangle(E_c) - E_g \quad (4.33c)$$

with a random number  $r$  between 0 and 1. For a primary impacting hole the secondary carrier energies for the two holes  $E'_{h1}$ ,  $E'_{h2}$  and the single electron  $E'_e$  are selected corresponding to

$$E'_{h1} = \langle E'_v \rangle(E_v) r \quad (4.34a)$$

$$E'_{h2} = \langle E'_v \rangle(E_v) - E'_{h1} \quad (4.34b)$$

$$E'_e = E_v - \langle E'_v \rangle(E_v) - E_g . \quad (4.34c)$$

Fig. 4.12 presents the mean values of the secondary energy distributions for GaAs, InP, InAlAs, and InGaAs.

### 4.3 Alloy Scattering

In an alloy  $A_{\tilde{x}}B_{1-\tilde{x}}C$  having the mole fraction  $\tilde{x}$ , different arrangements of the group-III atoms  $A$  and  $B$  between the group-V atoms  $C$  within the primitive cell are realizable. The crystal potential periodicity is disturbed. Therefore, alloy disorder is a source of scattering. The alloy scattering rate is given by [74] (Eq. (4.167), p. 182 <sup>1</sup>)

$$W_{\text{alloy}}(E) = \frac{\pi \Delta V^2 \tilde{x}(1-\tilde{x}) \Omega_0}{\hbar} \mathcal{D}_{\nu'}(E) \quad (4.35)$$

---

<sup>1</sup>The factor 2 is accounted for in the final density of states

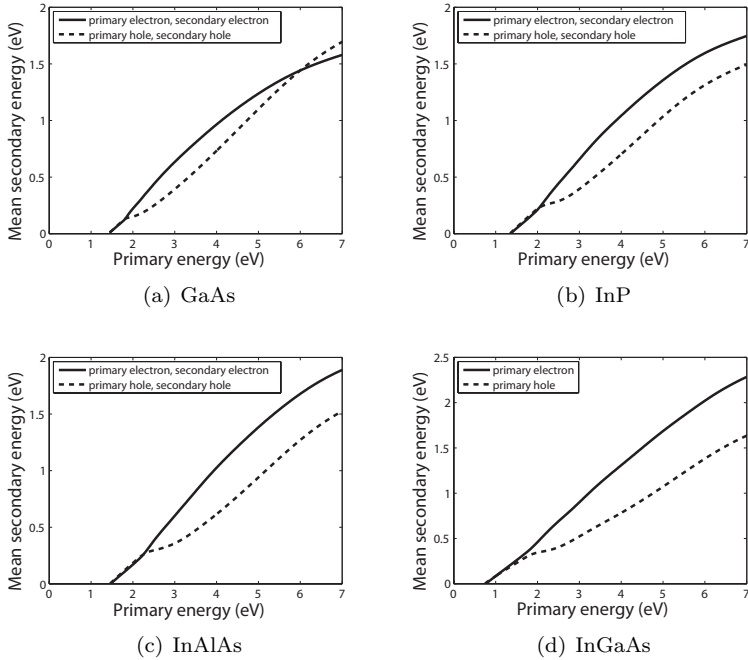


Figure 4.12: Mean energy of secondary carriers after impact ionization in random- $\mathbf{k}$  approximation vs. the primary energy.

where the interaction potential  $\Delta V$  is determined empirically [74] (p. 182).  $\mathcal{D}_{\nu'}(E)$  is the final density of states including spin degeneracy. Fig. 4.13 illustrates the alloy scattering rate of electrons in InGaAs.

## 4.4 Overview of Scattering Rate Forms

The full-band Monte Carlo scattering model in this work utilizes three forms of scattering mechanisms depending on their proportionality functions: (i) elastic acoustic phonon scattering, nonpolar optical phonon scattering, intervalley phonon scattering, alloy scattering, (ii)



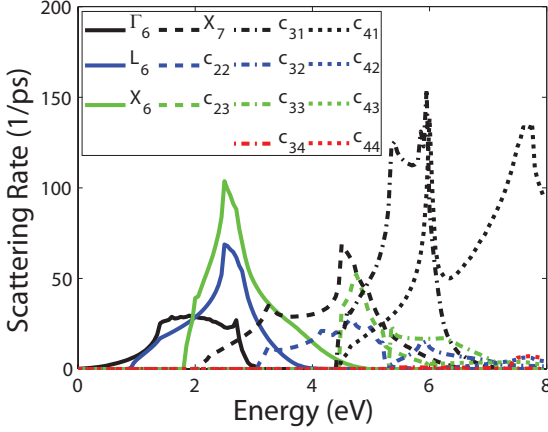


Figure 4.13: Alloy scattering rates of conduction band valleys in InGaAs.

polar optical phonon scattering, and (iii) impact ionization scattering. Scattering rates of the first form are given by

$$W_{\nu\nu'}^m(E) = \Lambda_{\nu\nu'}^m \mathcal{D}_{\nu'}(E \pm E_{\text{trans}}) \quad (4.36)$$

with the particle energy  $E$  before and  $E' = E \pm E_{\text{trans}}$  after scattering, the prefactor  $\Lambda_{\nu\nu'}^m$  of scattering mechanism type  $m$ , and the initial  $\nu$  and final valley  $\nu'$ . The scattering rate is proportional to the final DOS  $\mathcal{D}_{\nu'}(E')$  (see Eq. (3.8a)). The polar optical phonon scattering rate is of the second form

$$W_{\nu'}^{\text{POP}}(E) = \Lambda^{\text{POP}} \mathcal{D}_{q^{-2}, \nu'}(E) \quad (4.37)$$

with its prefactor  $\Lambda^{\text{POP}}$ . The rate is proportional to the direction-weighted DOS  $\mathcal{D}_{q^{-2}, \nu'}$  (see Eq. 3.12a). The impact ionization scattering rate defines the third form

$$W^{\text{ii}}(E) = \Lambda^{\text{ii}} \mathcal{D}_{\text{ii}}(E) \quad (4.38)$$

with the prefactor  $\Lambda^{\text{ii}}$ . The scattering rate of the third form is proportional to the density of states overlap integral  $\mathcal{D}_{\text{ii}}$  (see Eqs. (3.14)

Mechanism	$\Lambda$
elastic acoustic phonon scattering	$\frac{\pi k_B T \Xi_\nu^2}{\hbar u_1^2 \rho}$
nonpolar optical phonon scattering	$\frac{\pi D^2}{2\rho\omega_{\text{op}}}(n_{\text{op}} + \frac{1}{2} \mp \frac{1}{2})$
intervalley phonon scattering	$\frac{\pi D_{\nu\nu'}^2}{2\rho\omega_{\nu\nu'}}(n_{\nu\nu'} + \frac{1}{2} \mp \frac{1}{2})$
alloy scattering	$\frac{\pi \Delta V^2 x(1-x)\Omega_0}{\hbar}$
polar optical phonon scattering	$\frac{2\pi}{\hbar} e^2 F^2 (n_{\text{op}} + \frac{1}{2} \mp \frac{1}{2})$
impact ionization	$\frac{2\pi}{\hbar}  M_{\text{ii}} ^2 \frac{\Omega^3}{N_{\text{cell}}}$

Table 4.1: Overview of scattering rate prefactors  $\Lambda$ . The effective acoustic phonon deformation potential  $\Xi$ , the effective nonpolar optical phonon deformation potential  $D$ , and the impact ionization prefactor  $\Lambda^{\text{ii}}$  are tuned to experimental data.

and (3.15)). Table 4.1 summarizes the prefactors  $\Lambda$  of the different scattering mechanisms.

The computation of the total carrier-phonon scattering rates for Figs. 4.14 and C.5 relies on the following procedure. A valley defines an energy interval, which spans the possible energy range of a carrier being within that valley. Let a particle with a particular energy  $E_\nu$  have the possibility to reside in  $l$  valleys. Then, the total carrier-phonon scattering rate is the averaged rate of  $l$  possible rates at the energy  $E_\nu$ . Figs. 4.14 and C.5 present the total carrier-phonon and impact ionization scattering rates of GaAs, InP, InAlAs, and InGaAs. Additionally, Fig. C.4 illustrates a comparison of the scattering rates for the  $\Gamma_6^-$ ,  $L_6^-$ , and  $X_6^-$ -valleys of GaAs evaluated with the full-band structure and its nonparabolical approximation.

## 4.5 Choice of State After Scattering

After the selection of a scattering mechanism, the final  $\mathbf{k}$ -state for a given final energy and valley or band has to be chosen. For elastic processes, like elastic acoustic phonon and alloy scattering,  $E' = E$  holds true. For processes involving intravalley optical phonons, the

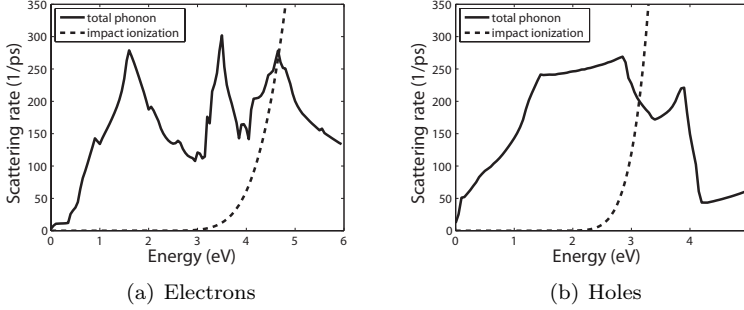


Figure 4.14: Full-band carrier-phonon and impact ionization scattering rates of GaAs.

final energy is  $E' = E \pm \hbar\omega_{\text{op}}$ . The final energy for intervalley phonon scattering is  $E' = E \pm \hbar\omega_{\nu\nu'} - \Delta E_{\nu\nu'}$ . The mean values of the secondary carrier distributions  $\langle E'_c \rangle(E_c)$  and  $\langle E'_v \rangle(E_v)$  define the secondary carrier energies after an impact ionization event.

In general, the probability that the  $\mathbf{k}$ -state is inside the  $i$ th cubic box is given by [1] (Eq. (10), p. 873)

$$P_i(\mathbf{k}) = \frac{\int W(\mathbf{k}, \mathbf{k}') d^3 k'}{\int_{V_{\text{BZ}}} W(\mathbf{k}, \mathbf{k}') d^3 k'}. \quad (4.39)$$

Here,  $V_{\text{cube}}$  is the volume of the  $\mathbf{k}$ -space discretization box. For scattering mechanisms having the form of Eq. (4.3) (all except polar optical phonon scattering) the probability to choose the  $i$ th box becomes [1] (Eq. (10), p. 873)

$$P_i(E') = \frac{\int \delta(E' - E(\mathbf{k}')) d^3 k'}{\int_{V_{\text{wedge}}} \delta(E' - E(\mathbf{k}')) d^3 k'} \quad (4.40a)$$

$$= \frac{\mathcal{D}_i(E')}{\sum_{j \in \text{wedge}} \mathcal{D}_j(E')} \quad (4.40b)$$

with the box DOS defined in Eq. (3.11) and the volume of the irreducible wedge  $V_{\text{wedge}}$ . For polar optical phonon scattering (Eq. (4.18)) the probability for the  $i$ th cubic box is given by

$$P_i^{\text{pop}}(E') = \frac{\int_{V_{\text{cube}}} \frac{1}{q^2} \delta(E' - E(\mathbf{k}')) d^3 k'}{\int_{V_{\text{BZ}}} \frac{1}{q^2} \delta(E' - E(\mathbf{k}')) d^3 k'} \quad (4.41a)$$

$$= \frac{\mathcal{D}_{q^{-2},i}(E')}{\sum_{j \in \text{BZ}} \mathcal{D}_{q^{-2},j}(E')} \quad (4.41b)$$

with the direction-weighted box DOS defined in Eq. (3.13).

The sum over all box density of states in the wedge hinders a fast evaluation of Eqs. (4.40b) and (4.41b). Therefore, the author uses the rejection technique (see App. A.2) and energy interval lists for an efficient computation of the final cubic box [1] (p. 873) (see Chap. 6). The  $i$ th cubic box within the corresponding energy interval of the list is chosen with uniform probability. If the desired energy is not represented within the chosen box, the cube is rejected. The box is accepted only when [1] (Eq. (12), p. 873)

$$\mathcal{D}_i(E') \geq r \mathcal{D}^{\text{max}}(E') \quad (4.42)$$

or

$$\mathcal{D}_{q^{-2},i}(\mathbf{k}') \geq r \mathcal{D}_{q^{-2}}^{\text{max}}(\mathbf{k}') \quad (4.43)$$

holds true. Here,  $\mathcal{D}^{\text{max}}(E')$  is the maximal box DOS and  $\mathcal{D}_{q^{-2}}^{\text{max}}(\mathbf{k}')$  is the maximal direction-weighted box DOS (see Chap. 6). Otherwise, the procedure is repeated until a cube is accepted. The selection of a final cubic box for a polar optical phonon scattering event degrades the performance compared to the selection of a DOS proportional scattering mechanism because the number of rejection steps depends on the ratio of  $\mathcal{D}_{q^{-2}}^{\text{max}}/\langle \mathcal{D}_{q^{-2}} \rangle$ , which is higher than  $\mathcal{D}^{\text{max}}/\langle \mathcal{D} \rangle$  [1] (p. 874).

In general, the intersection of a cube with a plane can be a triangle, a quadrangle, a pentagon, or a hexagon. If the intersection is a

polygon with more than three edges, the equi-energy surface is divided into triangles [1] (p. 874). The probability to choose one of the triangles is proportional to the area of the triangle [1] (p. 874)

$$A_{\Delta} = \frac{1}{2}|(\mathbf{b} - \mathbf{a}) \times (\mathbf{c} - \mathbf{a})| \quad (4.44)$$

with the corner vectors  $\mathbf{a}$ ,  $\mathbf{b}$ , and  $\mathbf{c}$ . The method of choice to select a triangle is the direct method for discrete probabilities (see App. A.1.2). The direct method is used to get a uniformly distributed  $\mathbf{k}$ -state on the selected triangle [29] (Eqs. (5.72) and (5.73), p. 96)

$$\mathbf{k}_{\Delta} = \mathbf{a} + \lambda_1(\mathbf{b} - \mathbf{a}) + \lambda_2(\mathbf{c} - \mathbf{a}) \quad (4.45)$$

with  $\lambda_1 = 1 - \sqrt{1 - r_2}$  and  $\lambda_2 = r_2(1 - \lambda_1)$ . For scattering mechanisms fulfilling Eq. (4.3) the final state is equally probable for any chosen final wedge:

$$\mathbf{k}_{\text{BZ}} = \underline{\mathbf{T}}^{-1}\mathbf{k}_{\text{wedge}} \quad (4.46)$$

with the inverse transformation matrix  $\underline{\mathbf{T}}^{-1}$ . This is the case for all used mechanisms except polar optical phonon scattering. The computation of the polar optical phonon scattering rate already includes the probability of  $\mathbf{k}'$  being in the whole Brillouin zone.

In summary, the selection of the final state after scattering consists of the

- determination of the final cubic box applying the rejection technique to Eq. (4.40b) or Eq. (4.41b) (Fig. 4.15(a)),
- selection of a triangle according to its area given in Eq. (4.44) (Fig. 4.15(b)),
- computation of the final  $\mathbf{k}$ -state on the triangle defined by Eq. (4.45) (Fig. 4.15(c)), and the
- choice of the inverse transformation matrix into one of the 48 wedges for mechanisms fulfilling Eq. (4.3) (Fig. 4.15(d)).

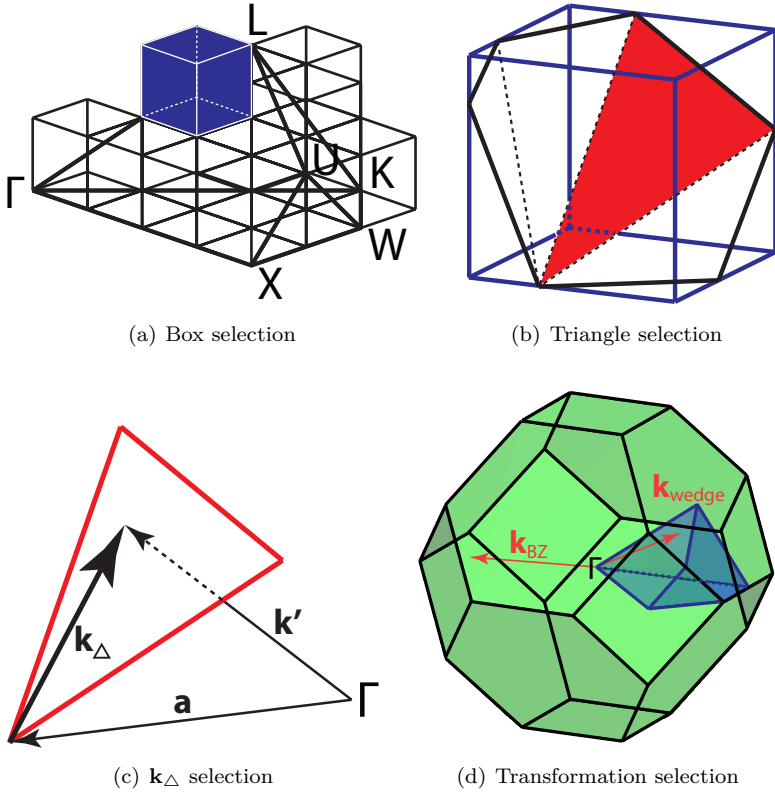


Figure 4.15: Illustration of the  $k'$  selection process.

## 4.6 Approximations

Surely, the ultimate goal in the simulation of carrier transport in semiconductors would be the usage of the ion potential as the only input. However, as a result of the huge computational effort, approximations have to be made. For example, the model for the dielectric function, the lattice dynamics model, the approximations to the *ab initio* exchange and correlation interactions lead to inherent difficulties and uncertainties [2] (Chap. 5). Efficient device simulation asks for approximations of the full transition elements while keeping the main physical features [24] (p. 149). In the case of a full-band Monte Carlo computation of breakdown characteristics of SPADs efficient modeling of carrier scattering renders the calculation actually feasible on nowadays parallel CPU power on standard computer clusters. For a more detailed discussion of involved approximations in the scattering rate computation the author refers to Hess et al. [2].

Carrier-carrier scattering, plasmon scattering, piezoelectric scattering, and ionized impurity scattering are neglected due to their small influence on the high-energy tail of the distribution function.

### 4.6.1 Fermi's Golden Rule

One has to be aware that in the derivation of Fermi's golden rule an assumption is made that limits its usage for high electric fields. The energy conserving  $\delta$ -function appears for the time limit  $t \rightarrow \infty$  [93] (p. 476). For practical calculations  $t \rightarrow \infty$  translates to  $t \gg \hbar/E$ , which depicts Heisenberg's uncertainty principle [30] (p. 424). For a finite observation time the uncertainty in the energy difference of the initial and the final state is in the order of  $\hbar/t$ . If one considers the process approximately energy conserving, this uncertainty has to be small compared with characteristic energies of the carrier [30] (p. 425). But at high electric fields in the order of  $10^7$  V/m the time between scattering events is so short that the assumption of point-like events in space and time does not hold. The intracollisional field effect accounts for the issue of the influence of the electric field during the scattering process [28] (p. 139). Additionally, rigorous energy conservation is not fulfilled giving rise to collision broadening [17] (p. 88). Works exist

that include the intracollisional field effect and collision broadening into the semiclassical transport theory [79, 94, 95]. Quade et al. [96] describe the influence of a density matrix treatment to the impact ionization rate.

At high electric fields the scattering potentials are strong and collisions become dependent [28] (p. 138) contradicting the assumptions for the validity of the BTE (see Sec. 2.1.2). One has to be aware that for high carrier energies the picture of semiclassical charge transport is pushed to its limits. On the other hand, the range of validity of the Boltzmann transport equation may have been underestimated [64] (p. 9722). Nevertheless, it is common practice in the community of semiclassical high-field transport to disregard the intracollisional field effect and the collision broadening [1, 64].

## 4.6.2 Transition Matrix Elements

The full-band Monte Carlo simulators described in literature differ mainly in the usage of the implemented scattering model. For phonon scattering the differences lie in the treatment of the deformation potential, the overlap integral, and the phonon dispersion relation. Commonly, phonons are treated to be in a thermodynamic heat bath in equilibrium. On the most basic side of the hierarchy, starting from Fermi's golden rule, the full transition rate  $W_{nn'}(\mathbf{k}, \mathbf{k}')$  has to be computed from every initial  $(n, \mathbf{k})$  to any final state  $(n', \mathbf{k}')$ . The deformation potentials are not fit parameters but are computed based on the full-band structure. This means that there is less freedom for calibration, and the quality of the transition rates depends on the complexity of the underlying theory [24] (p. 148). The full phonon dispersion is included. Fischetti et al. [2] (Chap. 5), Kunikiyo et al. [82], and Yoder et al. [83] contributed to this research-intensive and computationally heavy approach.

However, the feasibility and the efficiency of device simulation ask for approximations of the full transition matrix elements while keeping the main physical features [24] (p. 149). It is possible to define volumes or valleys in reciprocal space where the deformation potentials are approximately constant [62], [82] (p. 301), [55] (p. 815) [84, 29]. This allows a grouping of the phonon transition rates into packages of phonon scattering mechanisms depending on the initial



and final valleys. There are shades of differences within this approach in literature. For example, Fischetti et al. [64] computed the full overlap integral and approximated the acoustic phonon dispersion by a trigonometric function. Bufler [63] and Jungemann et al. [29] do not resolve the direction dependency of the overlap integral and use the Debye and Einstein approximation for the phonon dispersion relations, which leads to a computationally efficient formulation of the scattering rates. In principle, the overlap integral is included effectively in the definition of the empirical deformation potential.

Models for the calculation of the impact ionization rates, starting from Fermi's golden rule, vary widely in literature. For example, Kane [69], Jung et al. [66], and Kuligk et al. [97] computed the impact ionization rate evaluating the detailed matrix elements, the dielectric function and took momentum conservation into account. Kane introduced the random- $\mathbf{k}$  approximation [69], which neglects momentum conservation. Sano et al. [65] additionally introduced an approximation that assumes mean secondary carrier energies. Some FBMC works utilize a modified Keldysh formula, which is a fit to the impact ionization rate of first principle approaches. At the advent of full-band Monte Carlo simulations, and interestingly, even later, the Keldysh approximation, valid for parabolic band structures, was used for the impact ionization rate calculation despite the existence of Kane's computationally light RKA [64, 98, 56]. Fig. 4.9(a) illustrates the big difference of impact ionization scattering rates calculated with first principle methods and the Keldysh formula.

The inclusion of momentum conservation and the computation of the Coulomb transition matrix elements render the first principle approaches of Kane [69], Jung et al. [66], and Kuligk et al. [97] computationally expensive and their numerical implementation laborious. The magnitude of the impact ionization rate depends on the volume of the available phase space and the average squared transition matrix element  $|M_{fi}|^2$  within that phase space. In indirect gap materials the mean matrix elements are insensitive to the impacting carrier energy. In direct gap materials the CMA underestimates the rate at low impacting carrier energies [99]. Kane's RKA works better for indirect gap than for direct gap semiconductors [100] (p. 4837). Momentum conservation allows a large number of possible final  $\mathbf{k}$ -states due to

the 48-fold symmetry of the cubic lattice. Practically, the large set of final  $\mathbf{k}$ -states will scatter randomly throughout the Brillouin zone. Additionally, the three integrals (sums) over  $\mathbf{k}$ -space (see Eq. (4.24)) considerably average the details of the band structure [69] (p. 628). The RKA and the CMA take advantage of these two properties and highly reduce the complexity of the impact ionization rate computation from a computational and implementational point of view. The RKA and CMA reduce the nine-dimensional integration over the  $\delta$ -function in reciprocal space to a two-dimensional integral over one-particle density of states in energy space. The costly computation of the Coulomb transition matrix elements is bypassed by tuning it to experimental data [55] (p. 816). The application of the RKA and the CMA is an appealing possibility to compute the impact ionization rate with a manageable effort and to keep agreement with first principle methods [69] (p. 628) [87] (p. 43) [55] (p. 818). Compared to the approach of Sano et al. Kane's RKA provides information about the secondary carrier energies without taking another fit parameter into account. The additional implementation work for the RKA- and CMA-based rate calculation compared to the implementation of the approach of Sano et al. is low. The use of the modified Keldysh formula is a viable option for the well-known material GaAs. Secondary carrier energies are provided in literature (e.g. [66], Fig. 7, p. 2477). For the materials InP, InAlAs, and InGaAs the impact ionization scattering rates and the secondary carrier energy distributions were not available in literature. Additionally, the author prefers Kane's RKA and the CMA to compute all the scattering rates based on the same full-band structure, and therefore, to keep band structure consistency. Furthermore, the selection of the final  $\mathbf{k}$ -states in the RKA is computationally efficient. The importance of the impact ionization rate around the threshold energy depends on the high energy tail of the carrier distribution and the ratio of the impact ionization rate to the phonon scattering rates. A carrier, being able to impact ionize, has to survive to energies above threshold emitting less phonons than the bulk of particles. The carrier distribution above the threshold energy therefore strongly depends on dissipation processes below the threshold energy. If the carrier has survived to impact ionization enabling energies, the occurrence of impact ionization has to be relevant compared to phonon scattering. However, compared with

phonon scattering, impact ionization is of no practical importance at energies around threshold [69] (p. 628) [99] (p. 4837). Practically, impact ionization takes place for energies where the ratio of the impact ionization rate and the total phonon scattering rate exceeds about  $10^{-2}$  (compare with Figs. 4.10 and 4.14).



## Chapter 5

# Single Photon Avalanche Diodes

Single photon avalanche diodes are reverse biased diodes operated above the breakdown voltage  $V_b$  in the Geiger-mode. The name Geiger-mode stems from the similar breakdown process in Geiger-Müller detectors for radioactive particles. Linear-mode avalanche photodiodes (APD) are biased below the breakdown voltage. The term linear-mode originates from the fact that for applied voltages smaller than the breakdown voltage the output photocurrent of the APD is proportional to the input optical intensity [11] (p. 175). In principle, a SPAD consists of an absorber and a multiplication region. The absorber layer is made of a semiconductor material having an appropriate band gap to absorb the desired photon energy by lifting an electron from the valence band into the conduction band. For a sufficiently high band gap the multiplication and absorption regions consist of the same semiconductor because the tunneling rate is acceptable. This is the case for Si-SPADs, which operate at visible wavelengths [10] (Fig. 6, p. 1275). For desired near infrared (NIR) photon detection a structure with separated absorption and multiplication (SAM) regions is utilized. The absorber is made of a low band gap semiconductor whereas the multiplication layer consists of a semiconductor material with a wider band gap to limit tunneling to an

acceptable level. In NIR SPADs, InGaAs is the absorber layer and InP [11] (p. 177) or InAlAs [101] (p. 293) form the multiplier. To gain better control over the internal electric field profile, a field control layer separates the absorber and the multiplier (SACM: separate absorption charge and multiplication). The aim of the field control layer is to confine the high electric field as effectively as possible to the high band gap region of the multiplier. Otherwise, a high electric field in the low gap absorption layer leads to tunneling of valence band electrons into the conduction band, and therefore, dark counts are initiated. On the other hand, the electric field has to be strong enough to quickly separate the photoexcited carriers. One photogenerated carrier drifts into the multiplication layer and leads to impact ionization. The newly impact ionized electron-hole pair can impact ionize additional pairs leading to a self-sustaining avalanche. An active or passive quenching circuit stops the avalanche by regulating the applied bias below the breakdown voltage. After a hold-off time the SPAD is biased above the breakdown voltage again.

Especially devices for NIR photon counting suffer from carrier trapping and detrapping by thermal emission at defects within the multiplication layer. If the SPAD is in its armed state above the breakdown voltage, a detrapped carrier can trigger a dark count. This mechanism is named afterpulsing. Sufficiently long hold-off times  $t_{\text{off}}$  reduce afterpulsing to virtually zero. However, this approach sets severe limitations for NIR photon counting devices because it limits the achievable counting rates to the order of  $1/t_{\text{off}}$ . More costly strategies have to be applied. Beside the reduction of material defects or the stimulated detrapping, the decrease of the potential number of charges that can be trapped is the most promising approach to lower afterpulsing [11] (p. 184). Smaller avalanche current charge flow can be achieved with a more elaborate, and thus, more expensive active quenching circuitry. SPADs having a high dark count rate (DCR) are usually operated in the gated mode. A bias is applied just below the breakdown voltage and a gate pulse puts the voltage above breakdown for a short time (approximately 1-100 ns). Operation in the gated mode reduces the probability of a dark count during the gate pulse [101] (p. 285). Lower temperatures decrease the dark count rate because of a lower thermal generation of free carriers. However, lower temperatures increase afterpulsing owing to longer trap lifetimes [101]

(p. 287).

The first studies on the behavior of avalanche multiplication in reverse biased pn junctions above the breakdown voltage reach back to the Shockley laboratory in the 1960s [10] (p. 1267). Since then, remarkable progress has been achieved for SPADs concerning their important performance parameters: photon detection efficiency (PDE), dark count rate, jitter, and afterpulsing [11]. The PDE is the product of the quantum efficiency  $\eta_q$ , the probability that the photoexcited carrier survives into the multiplier  $P_c$ , and the breakdown probability  $P_b$  that the carrier activates a self-sustaining avalanche [11] (p. 178):

$$\text{PDE} = \eta_q P_c P_b . \quad (5.1)$$

The PDE depends on the electric field mainly via  $P_b$ . Concerning the PDE, a high electric field is favorable because  $P_b$  rises with the field. On the other hand, for increasing electric fields SPAD performance degrades owing to dark currents as a result of band-to-band or trap-assisted tunneling in the multiplier. Hence, a steep rise of the breakdown probability with higher electric field is desirable. The timing jitter originates from the different transit times of carriers due to the variation of the location of photon absorption, from the delayed release of trapped carriers at possible heterojunctions, and from fluctuations of the avalanche build-up time  $t_b$ . More precisely, the jitter by virtue of the avalanche build-up time originates from the randomness of the impact ionization process, the expansion of the initially point-like avalanche to the entire high field region, and from local nonuniformities of the excess bias. The avalanche build-up time is the main contribution to timing jitter [11] (p. 180 and 181).

NIR SPADs and linear-mode APDs share the same device structure design of the SAM or SACM type. APDs are designed for a high gain-bandwidth product and a low excess noise factor. Thin multiplication layer widths ( $< 0.5 \mu\text{m}$ ) are advantageous for both APD performance features. The charge carrier transport is faster and the dead-space effect leads to a more deterministic avalanche process, and hence, lower excess noise [11] (p. 178). APDs are optimized for an electric field profile leading to a gain of 10-20 because

the system of the APD and the amplifier possesses its maximum signal-to-noise ratio [101] (p. 287). SPADs are optimized for a low dark count rate and a high photon detection efficiency whereas the gain-bandwidth product and the excess noise factor are irrelevant [11] (p. 178). Compared to APDs, in SPADs the electric field in the absorption layer has to be lower, to reduce tunneling, while the field in the multiplication region has to be higher, to operate in the Geiger-mode [101] (p. 287). Concerning the multiplication layer width, contradictory theoretical predictions have confused the gain material layer design. Wang et al. [12] and Ramirez et al. [13] predict an increasing breakdown probability for thicker multiplication regions whereas Ng et al. [14], Hayat et al. [15], and Tan et al. [16] predict the opposite behavior.

The author concentrates on the investigation of the high-energy charge transport and multiplication process in the SPAD multiplier by means of the FBMC method. Therefore, according to Tan et al. [16], PIN diode structures (see Fig. 5.1) are investigated with different intrinsic region widths operated in the Geiger-mode. In order to compare the SPAD simulations with literature, the temperature is set to  $T = 300$  K. This work examines three multiplication materials: GaAs is utilized as model material in literature for the evaluation of SPAD breakdown properties. InP and InAlAs are suitable materials for real-world devices. The effect of tunneling is not considered. This work examines the breakdown probability, which is the main contribution to the PDE, and the time to avalanche breakdown. In addition, the standard deviation of the time to avalanche breakdown is calculated, which is the main contribution to the timing jitter. Chapter 7.3 presents the results of the FBMC investigation of SPAD breakdown properties.



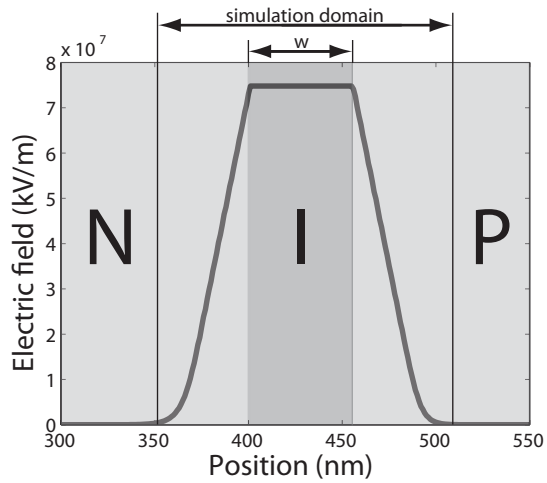


Figure 5.1: PIN diode as SPAD with intrinsic multiplication layer width of  $w = 55$  nm and a simulation domain of 167 nm for the FBMC simulations.



## Chapter 6

# Full-band Monte *Carlo* Simulator

During this PhD work, *CarloS* has come into existence. *CarloS* is an objected-oriented C++ full-band Monte *Carlo Simulator*, which has been developed from scratch. Fig. 6.1 reveals a portrait of *CarloS* in action. A Tcl interface reads the Tcl input files. MPI parallelized code is available for the computation of polar optical phonon scattering rates. Monte Carlo simulations are parallelized with OpenMP. For the discretization of the irreducible wedge of the first Brillouin zone  $N = 20, 40, 60, 80,$  and  $100$  are possible to choose.  $N$  is the number of cubic boxes in the x-direction (compare with Fig. 3.1). The total number of discretization boxes corresponds to  $N_{\text{tot}} = 825, 5950, 19375, 45100,$  and  $87125,$  respectively. During the initialization phase, *CarloS* loads several precomputed tables:

- Energy table:  
The EPM full-band dispersion relation is computed on the  $\mathbf{k}$ -space grid (see Sec. 3.2) for three valence bands and four conduction bands.
- Gradient table:  
The derivatives of the full-band structure  $\nabla E(\mathbf{k})$  are saved for three valence bands and four conduction bands.

Figure 6.1: Portrait of *CarloS*.

- Valley allocation table:  
Every cubic box object saves seven assigned valleys (see Sec. 3.3).
- Density of states table:  
The density of states for every valley is evaluated for an energy grid with a spacing of 1 meV (see Sec. 3.4).
- Energy interval list table:  
Every cubic box defines a box energy interval  $E_{\text{box}} = [E_{\text{box},\text{min}}, E_{\text{box},\text{max}}]$  of possible energies within that cube. The energy interval for the list consists of intervals of 10 meV width [1] (p. 873):  $E_{\text{list}} = [E_1, E_2, \dots, E_i]$ . Every cubic box energy interval  $E_{\text{box}}$  is assigned to the  $E_i$ 's of  $E_{\text{list}}$  it overlaps with (see Sec. 4.5).
- Maximal box density of states tables:  
The maximal density of states per cubic box  $\mathcal{D}^{\text{max}}$  for a given energy is precomputed on a 0.1 meV grid and saved on a 10 meV grid. The author estimates  $\mathcal{D}_{q^{-2}}^{\text{max}}(\mathbf{k}') \approx \mathcal{D}^{\text{max}}(E')/q_{\text{min}}^2$  with a

small but arbitrary minimal momentum transfer  $q_{\min}$  (see Sec. 4.5) .

- Impact ionization rate tables:  
The impact ionization rate is saved on an energy grid with 10 meV spacing. The energy integration grid has a spacing of 10 meV (see Sec. 4.2).
- Secondary carrier distribution tables:  
The author uses an energy grid with 10 meV spacing for the calculation of the secondary carrier distribution and the energy integration (see Sec. 4.2).
- Polar optical phonon scattering rate tables:  
The polar optical phonon scattering rate is precomputed parallelly on the equidistant tensor grid having  $N_{\text{tot}}$  elements (see Sec. 4.1.3).
- $\bar{\Gamma}$ -list table:  
The computation of upper bounds for the total scattering rate per cubic box and band is estimated with eight  $\mathbf{k}$ -point probes per box (see Sec. 2.2.2).
- Electric field table:  
In the case of SPAD device simulations, the electric field profile is precomputed with a commercial drift-diffusion model [23]. The electric field is saved on a 1 nm grid.

The band structure and its derivatives are saved in the irreducible wedge of the Brillouin zone. This has the advantage of smaller memory usage and the disadvantage of additional CPU demand because of transformation operations. For queries of the energy or the velocity the initial reciprocal space vector has to be transformed into the irreducible wedge according to

$$\mathbf{k}_{\text{wedge}} = \mathbf{T}\mathbf{k} \quad (6.1)$$

with an adequate transformation matrix  $\mathbf{T}$  (see App. B.2). Then, the energy or velocity is looked up in the corresponding table. The

dispersion relation fulfills  $E_n(\underline{\mathbf{T}}\mathbf{k}) = E_n(\mathbf{k})$ . For the velocity computation, the wedge velocity  $\mathbf{v}_{\text{wedge}}$  has to be transformed back into the initial wedge corresponding to

$$\mathbf{v} = \underline{\mathbf{T}}^{-1}\mathbf{v}_{\text{wedge}} . \quad (6.2)$$

*CarloS* saves the Monte Carlo output files in the hdf5 file format, which allows a clearly arranged storage of large amounts of data. The Monte Carlo data is postprocessed with MATLAB. Figs. 6.2 and 6.3 present the flowcharts of the main Monte Carlo loop and the SPAD device simulation.

Long-range interaction described by the Poisson equation is implemented into *CarloS* [22] (p. 94) but neglected for the calculation of SPAD properties. For the small amount of charge (see Sec. 7.3) and high electric fields, the author does not expect space-charge effects to be important. Since the simulated SPADs do not possess heterointerfaces, the implemented Wentzel-Kramers-Brillouin (WKB) approximation for quantum tunneling is not in use. The multiple refresh method, which is a statistical enhancement or variance reduction technique, is implemented [22] (p. 91) but not necessary for the SPAD devices examined in this work.

The PhD work of Hektor Meier [22] employed the nonparabolic approximation of the band structure to simulate avalanche photodiodes in linear-mode operation. The nonparabolic version of *CarloS* approximates the real band structure as the nonparabolic valleys  $\Gamma_6$ ,  $L_6$ , and  $X_6$ , and uses the Keldysh approximation for the impact ionization rate computation.

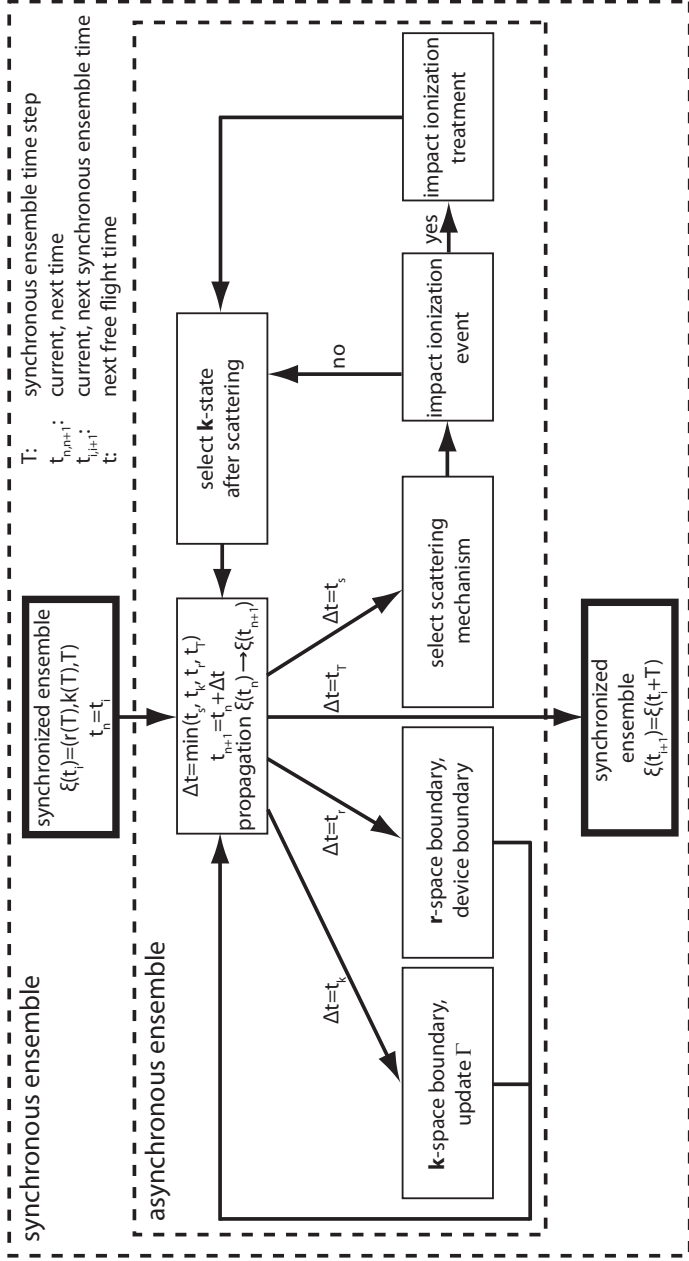


Figure 6.2: Flowchart of the main Monte Carlo loop.

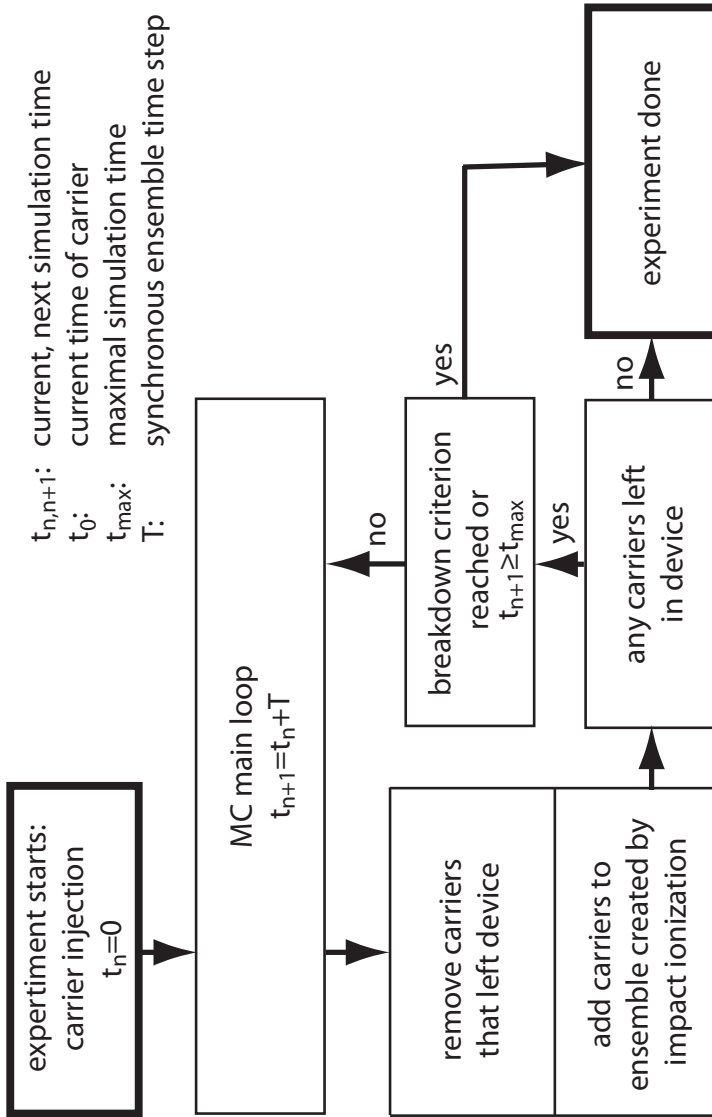


Figure 6.3: Flowchart of the SPAD device simulation.



# Chapter 7

## Simulation Results

All simulations are conducted with a discretization of  $N = 100$  corresponding to  $N_{\text{tot}} = 87125$   $\mathbf{k}$ -points discretizing the irreducible wedge of the first Brillouin zone. The electric field has the property  $\mathbf{E} = (0, 0, E_z)$ .

### 7.1 Calibration

As a result of the empirical deformation potential and impact ionization ansatz, the unknowns have to be calibrated to fit experimental data [64, 55]. The phonon parameters are found by fitting the FBMC curves of the drift velocity  $v$  versus the electric field  $|\mathbf{E}|$  against the experimental data. The impact ionization parameters are determined by means of fits of the FBMC electron and hole impact ionization coefficients  $\alpha$  and  $\beta$  versus the inverse electric field against the experimentally determined curves. During the MC procedure, *CarloS* tracks the distances between consecutive impact ionization events called ionization path lengths. The impact ionization coefficient corresponds to the inverse of the mean ionization path length. Concerning the details of the MC computation of the impact ionization coefficients, consult the thesis of Meier [22] (Sec. 6.1.1, p. 102). FBMC simulations show that the impact ionization prefactor  $\Lambda^{\text{ii}}$  depends exponentially

on the deformation potentials [55]. The reason is that a strong carrier-phonon interaction causes a distribution function with exponentially lower high-energy tail. Therefore, to adjust the impact ionization coefficient, an exponentially higher impact ionization rate has to be chosen. Furthermore, FBMC simulations reveal that the ionization coefficient depends weakly on the ionization rate but strongly on the deformation potentials [55]. Relatively small variation of the deformation potentials does not change  $v(E_z)$  appreciably but changes the impact ionization coefficient strongly with fixed  $\Lambda^{\text{ii}}$ . Hence, a series of similar fitting solutions may be found by sweeping the deformation potentials some few percents and adjusting the impact ionization parameter. First principle calculations of the impact ionization rates pinpoint the impact ionization fit parameters to the order of magnitude. Differences in the calibration results among the FBMC modeling groups have to be expected because the dependency of some fitting parameters on the experimental data is weak [102] (p. 639). In addition, the underlying dispersion relations vary especially for higher carrier energies (compare with Fig. 3.7). The deformation potentials, being fit to low energies, are extrapolated to high energies. Luckily, the main contribution to the scattering rates originates from the density of states, and is less a result of the matrix elements [55] (see Sec. 4.6.2).

For GaAs, InP, InAlAs, and InGaAs, Tables 7.1 and 7.2 outline the calibrated parameters. As a starting set of fit parameters the author took the values from Fischetti et al. [64] (p. 9732) and Dunn et al. [56] (p. 113) for GaAs, from Fischetti et al. [102] (p. 640) and Brennan et al. [67] (p. 5584) for InP, from Mateos et al. [103] (p. 251) and Watanabe et al. [104] (p. 1828) for InAlAs and InGaAs.  $\Xi_{<}$  and  $D_{<}$  label the effective electron-phonon deformation potentials for electron energies below the energy threshold  $E_{\text{th}}^{\Gamma_6}$  for the analytical treatment in the  $\Gamma_6$ -valley (compare with Fischetti et al. [64] p. 9732). Concerning the details of the nonparabolic treatment of the band structure for low-energy electrons in the  $\Gamma_6$ -valley, the author refers

to the thesis of Meier [22]. For GaAs and InP the effective acoustic phonon deformation potential for electrons reads

$$\Xi_\nu = \begin{cases} \Xi_{<} & \text{if } E < E_{\text{th}}^{\Gamma_6} \text{ and } \nu = \Gamma_6 \\ \Xi & \text{else} \end{cases} \quad (7.1)$$

and the effective nonpolar optical phonon deformation potential for electrons is given by

$$D_\nu = \begin{cases} D_{<} & \text{if } E < E_{\text{th}}^{\Gamma_6} \text{ and } \nu = \Gamma_6 \\ D & \text{else.} \end{cases} \quad (7.2)$$

For electrons in InAlAs the effective acoustic phonon deformation potential reads

$$\Xi_\nu = \begin{cases} \Xi_\nu & \text{if } \nu = \Gamma_6, L_6, X_6 \\ \Xi = \Xi_{\Gamma_6} & \text{else.} \end{cases} \quad (7.3)$$

The effective electron nonpolar optical phonon deformation potential in InAlAs and the effective electron acoustic phonon deformation potential in InGaAs have one value for all valleys. The effective electron nonpolar optical deformation potential in InGaAs is given by

$$D_\nu = \begin{cases} 0 & \text{if } \nu = \Gamma_6, X_6 \\ D_{L_6} & \text{if } \nu = L_6 \\ D = D_{L_6} & \text{else.} \end{cases} \quad (7.4)$$

Holes in GaAs, InP, InAlAs, and InGaAs simply possess one value of the deformation potential for the heavy hole, light hole, and split-off band. Figs. 7.1, 7.2, 7.3, and 7.4 summarize the calibration results for GaAs, InP, InAlAs, and InGaAs, respectively, and compare them with experiments and other FBMC simulations from literature: Armiento83 [105], Brennan84 [67], Brennan87 [106], Brennan89 [107], Bulman83 [108], Bulman85 [109], Cook82 [110], Dunn97 [56], Fischetti91 [102], Haase85 [111], Hill87 [112], Holway79 [67] (Ref. 34 therein), Houston77 [113], Kim92 [114], Littlejohn93 [115] (Chap. 4.2), Marsh80 [115] (Chapter 4.2, Ref. 4 therein), Majerfeld74 [116], Millidge95 [117], Nag85 [118], Osaka85 [119], Pearsall78 [120], Shigekawa91 [121], Shihijo81 [19], Taguchi86 [122], Watanabe90 [123],

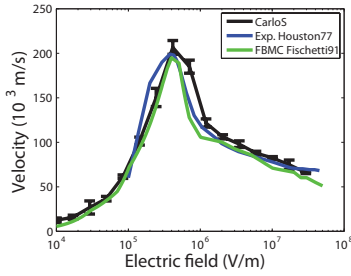
Material	$\Xi_{<}$ (eV)	$\Xi$ (eV)	$D_{<}$ $(\frac{\text{eV}}{\text{nm}})$	$D$ $(\frac{\text{eV}}{\text{nm}})$	$\Lambda^{\text{ii}}$ $(\frac{\text{nm}^9 \text{eV}}{\text{ps}})$	$E_{\text{th}}^{\Gamma_6}$ (eV)
Electrons						
GaAs	7.0	5.0	0.0	19	0.03	0.4
InP	7.0	5.0	0.0	20	0.012	0.4
Holes						
GaAs	-	5.0	-	50	1.0	0.0
InP	-	5.0	-	25	1.0	0.0

Table 7.1: Fit parameters for the binary materials GaAs and InP.

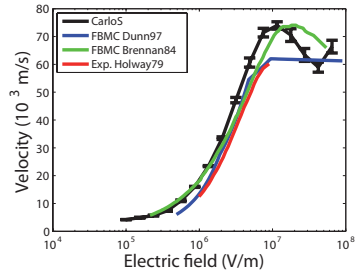
Windhorn82 [124], Windhorn83 [125], and You2000 [126]. The electron and hole saturation velocities  $v_{\text{sat}}$  of InAlAs are taken from Zhou et al. [127] (p. 435) and Palankovski et al. [128] (Table 3.33, p. 104). The bars of length  $2\sigma$  indicate the 68% confidence interval. Fig. 7.5 depicts a comparison of the impact ionization coefficients for the three gain materials. The trend of the steepnesses of the different curves can be estimated by comparing the strengths of the material's scattering rates (compare with Figs. 4.14 and C.5).

Material	$\Xi$ (eV)	$D$ $(\frac{\text{eV}}{\text{nm}})$	$\Delta V$ (eV)	$\Lambda^{\text{ii}}$ $(\frac{\text{nm}^9 \text{eV}}{\text{ps}})$
Electrons				
InAlAs	5.9/7.2/9.0	30	0.47	$2 \cdot 10^{-2}$
InGaAs	4.5	15	0.529	$1.2 \cdot 10^{-2}$
Holes				
InAlAs	4.3	43	0.38	1.0
InGaAs	4.5	25	0.2	$2 \cdot 10^{-2}$

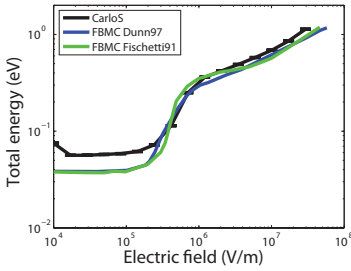
Table 7.2: Fit parameters for the ternary materials InAlAs and InGaAs. The three values of the effective electron acoustic phonon deformation potential of InAlAs correspond to the  $\Gamma_6^-$ ,  $L_6^-$ , and  $X_6^-$ -valley, respectively (compare with Mateos et al. [103]).



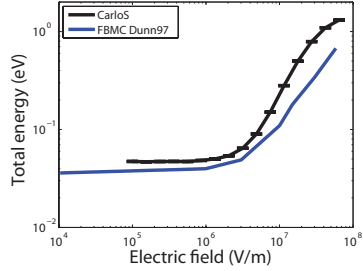
(a) Electron velocity vs. field



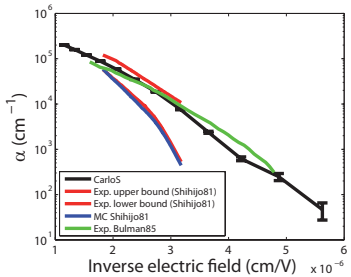
(b) Hole velocity vs. field



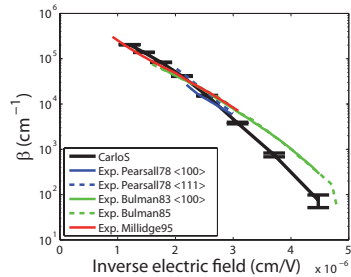
(c) Electron energy vs. field



(d) Hole energy vs. field

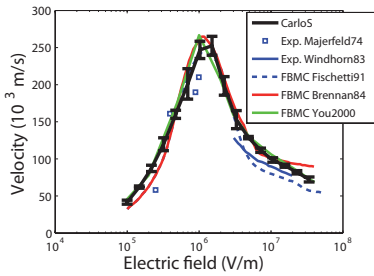


(e) Electron impact ionization coefficient vs. inverse field

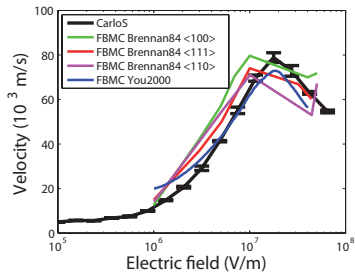


(f) Hole impact ionization coefficient vs. inverse field

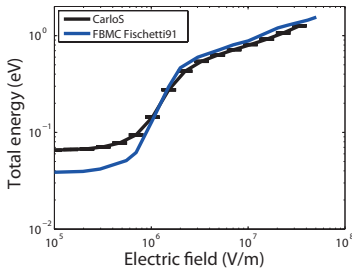
Figure 7.1: GaAs calibration results for the velocity, the energy and the impact ionization coefficients for electrons and holes.



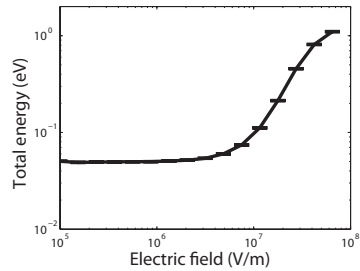
(a) Electron velocity vs. field



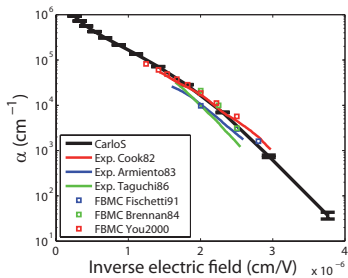
(b) Hole velocity vs. field



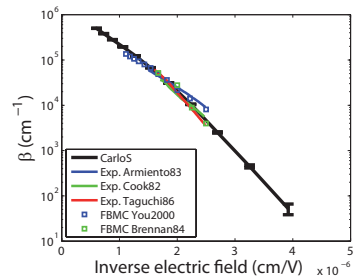
(c) Electron energy vs. field



(d) Hole energy vs. field

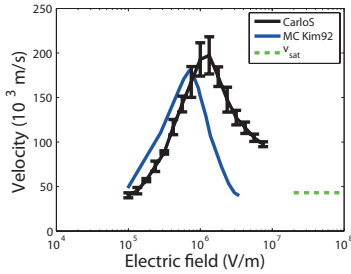


(e) Electron impact ionization coefficient vs. inverse field

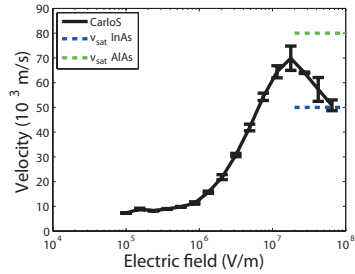


(f) Hole impact ionization coefficient vs. inverse field

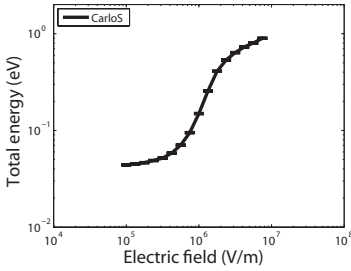
Figure 7.2: InP calibration results for the velocity, the energy and the impact ionization coefficients for electrons and holes.



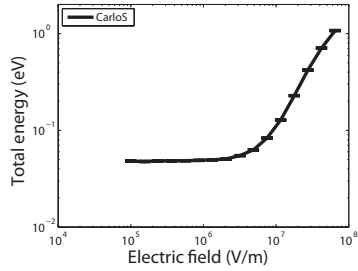
(a) Electron velocity vs. field



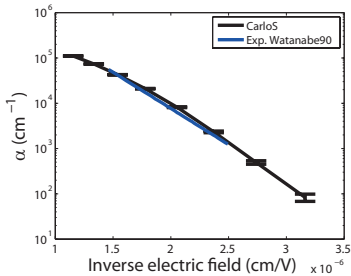
(b) Hole velocity vs. field



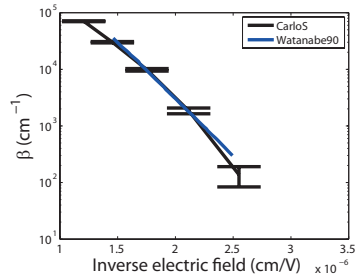
(c) Electron energy vs. field



(d) Hole energy vs. field



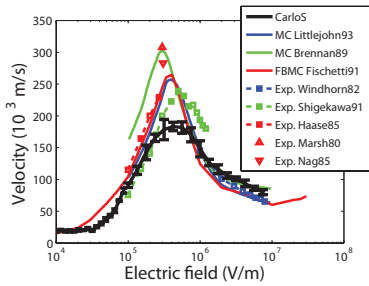
(e) Electron impact ionization coefficient vs. inverse field



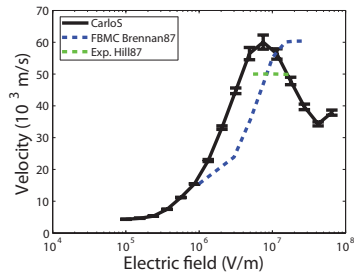
(f) Hole impact ionization coefficient vs. inverse field

Figure 7.3: InAlAs calibration results for the velocity, the energy and the impact ionization coefficients for electrons and holes.

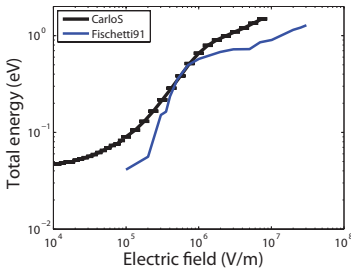




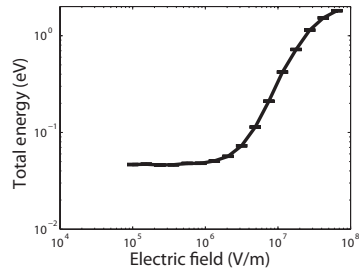
(a) Electron velocity vs. field



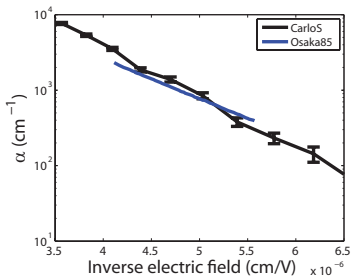
(b) Hole velocity vs. field



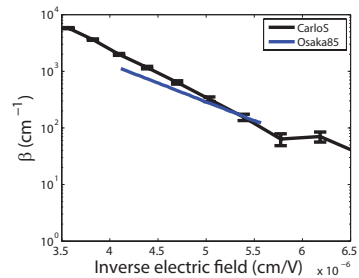
(c) Electron energy vs. field



(d) Hole energy vs. field



(e) Electron impact ionization coefficient vs. inverse field



(f) Hole impact ionization coefficient vs. inverse field

Figure 7.4: InGaAs calibration results for the velocity, the energy and the impact ionization coefficients for electrons and holes.

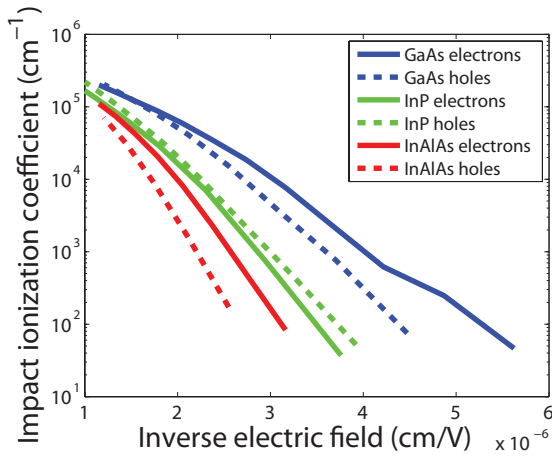


Figure 7.5: Comparison of the electron and hole impact ionization coefficients of the SPAD gain materials GaAs, InP, and InAlAs.

## 7.2 Impact Ionization Scattering Model

The RKA is considered to be “excellent” [100] (p. 4833) [55] (p. 818) because it provides agreement over many orders of magnitude as if no approximation is involved for energies where impact ionization is a relevant scattering mechanism. Interestingly, despite the positive assessment of the RKA and over 360 citations of Kane’s work [69], to the best of the author’s knowledge the impact ionization rates and the secondary carrier energies have not been provided to the MC modeling community of charge transport in terms of analytical fit functions yet [129]. First principle evaluation of the impact ionization rates are provided to the community as piecewise defined modified Keldysh formulas [66] (Eq. (17), p. 2477)

$$W_{ii}(E) = \Lambda^{ii}(E - E_{th})^\gamma \quad (7.5)$$

with the threshold energy  $E_{th}$ . Here, the modified Keldysh formula is defined on three energy intervals I, II, and III according to

$$\text{energy interval} = \begin{cases} \text{I} & \text{if } E_{th} \leq E \leq E_1 , \\ \text{II} & \text{if } E_1 \leq E \leq E_2 , \\ \text{III} & \text{if } E_2 \leq E . \end{cases} \quad (7.6)$$

In this work, the parameters  $\Lambda^{ii}$ ,  $\gamma$ , and  $E_{th}$  are adjusted to possess a best straight line fit through

$$\tilde{W} = \gamma \tilde{E} + \tilde{\Lambda} \quad (7.7)$$

with

$$\tilde{W} = \ln(W_{ii}) \quad (7.8a)$$

$$\tilde{E} = \ln(E - E_{th}) \quad (7.8b)$$

$$\tilde{\Lambda} = \ln(\Lambda^{ii}) \quad (7.8c)$$

and small modifications to assure a continuous rate function at the boundaries  $E_1$  and  $E_2$ . The parameters  $\gamma$  and  $E_{th}$  are fitted against the numerically evaluated DOS overlap integral  $\mathcal{D}_{ii}$  (compare with Sec. 3.6). Table 7.3 shows the threshold energies and the defined

boundaries  $E_1$  and  $E_2$  of the energy intervals. The mean energies of secondary generated carriers are provided as straight line fits [66] (Eq. (19), p. 2478):

$$\langle E'_{c,v} \rangle(E_{c,v}) = mE_{c,v} + s . \quad (7.9)$$

Here,  $\langle E'_{c,v} \rangle$  corresponds to the sum of the energies of the two indistinguishable secondary particles. For example, analytical fit functions may be helpful for multivalley MC approaches, which model materials with incomplete data of impact ionization rates and secondary carrier energies.

As a result of the considerable averaging property of the nine-dimensional integration over the  $\mathbf{k}$ -space, the functional characteristic of the impact ionization rate, being fit to  $(E - E_{\text{th}})^\gamma$ , does not depend strongly on the details of the underlying band structure (compare with Fig. 4.9). The strength of the rate  $\Lambda^{\text{ii}}$  is very sensitive to the individual calibration, in particular to the carrier-phonon coupling strength. Therefore, the exponent  $\gamma$ , defining the functional characteristic of the rate, has to be understood as mainly determined by the band structure. In contrast to  $\gamma$ , the rate strength  $\Lambda^{\text{ii}}$  is viewed as a suggestion based on the particular calibration used in this work. Therefore,  $\Lambda^{\text{ii}}$  may be rather used as a fitting parameter in MC computations than  $\gamma$ . The inclusion of momentum conservation leads to a threshold energy being higher than the band gap energy. In the RKA, simply  $E_{\text{th}} = E_g$  holds true. Table 7.4 summarizes the parameters of the impact ionization rate fits. Figs. 7.6 and 7.7 illustrate the comparison of the RKA-based impact ionization rates and the fitted modified Keldysh formulas. Table 7.5 presents the fit parameters of the mean secondary carrier energies. Fig. 7.8 compares the straight line fits with the RKA-based calculations of the mean secondary carrier energies.

Material	$E_{th}$ (eV)	$E_1$ (eV)	$E_2$ (eV)
GaAs	1.42	1.82	4.5
InP	1.34	2.08	4.84
InAlAs	1.46	2.40	5.53
InGaAs	0.74	2.02	6.0

Table 7.3: Energy boundaries for the fits of the modified Keldysh formula. The threshold energies correspond to the particular band gap energies.

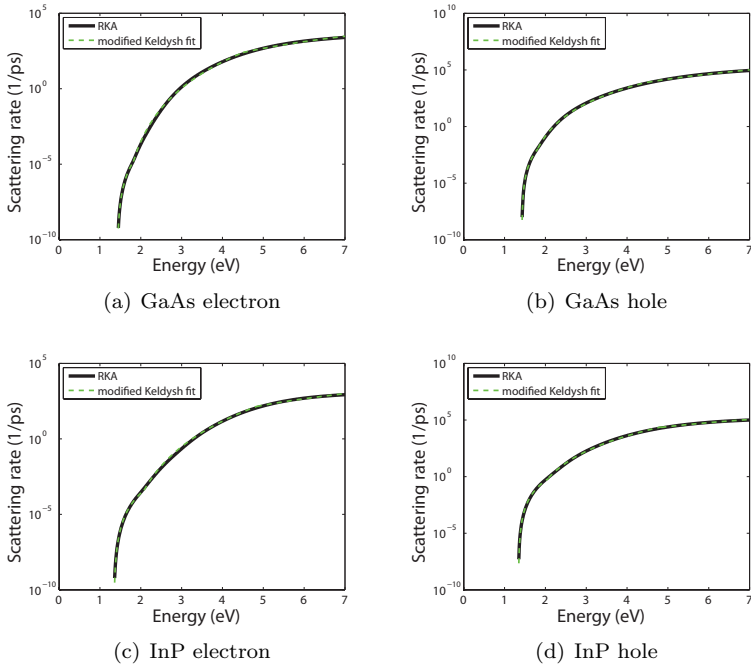


Figure 7.6: Modified Keldysh formulas fitted to the calculated RKA-based impact ionization rates of GaAs and InP.

	I	II	III
GaAs			
$\Lambda_e^{ii}$ (ps <sup>-1</sup> eV <sup>-<math>\gamma_e</math></sup> )	$5.53 \cdot 10^{-4}$	$2.62 \cdot 10^{-2}$	2.31
$\gamma_e$ (1)	3.94	8.15	4.17
$\Lambda_h^{ii}$ (ps <sup>-1</sup> eV <sup>-<math>\gamma_h</math></sup> )	$4.02 \cdot 10^{-1}$	4.72	$6.68 \cdot 10^1$
$\gamma_h$ (1)	3.93	6.61	4.26
InP			
$\Lambda_e^{ii}$ (ps <sup>-1</sup> eV <sup>-<math>\gamma_e</math></sup> )	$1.26 \cdot 10^{-3}$	$4.67 \cdot 10^{-3}$	$8.86 \cdot 10^{-1}$
$\gamma_e$ (1)	3.90	8.24	4.05
$\Lambda_h^{ii}$ (ps <sup>-1</sup> eV <sup>-<math>\gamma_h</math></sup> )	2.33	5.20	$3.50 \cdot 10^2$
$\gamma_h$ (1)	4.01	6.68	3.32
InAlAs			
$\Lambda_e^{ii}$ (ps <sup>-1</sup> eV <sup>-<math>\gamma_e</math></sup> )	$3.55 \cdot 10^{-4}$	$4.87 \cdot 10^{-4}$	$1.10 \cdot 10^{-1}$
$\gamma_e$ (1)	3.79	9.16	5.30
$\Lambda_h^{ii}$ (ps <sup>-1</sup> eV <sup>-<math>\gamma_h</math></sup> )	$9.58 \cdot 10^{-1}$	1.13	$7.86 \cdot 10^1$
$\gamma_h$ (1)	4.19	6.99	3.96
InGaAs			
$\Lambda_e^{ii}$ (ps <sup>-1</sup> eV <sup>-<math>\gamma_e</math></sup> )	$5.41 \cdot 10^{-5}$	$1.85 \cdot 10^{-5}$	$4.51 \cdot 10^{-3}$
$\gamma_e$ (1)	5.19	9.53	6.22
$\Lambda_h^{ii}$ (ps <sup>-1</sup> eV <sup>-<math>\gamma_h</math></sup> )	$7.46 \cdot 10^{-3}$	$4.75 \cdot 10^{-3}$	1.19
$\gamma_h$ (1)	5.30	7.12	3.80

Table 7.4: Fit parameters of the modified Keldysh formulas to the RKA-based calculation of the impact ionization scattering rates in the three energy intervals I, II, and III. The subscripts e and h indicate the parameters for electrons and holes, respectively.

Material	$m$ (1)	$s$ (eV)
GaAs	0.350	-0.501
InP	0.292	-0.417
InAlAs	0.384	-0.518
InGaAs	0.264	-0.357

Table 7.5: Parameters for the fits of the mean secondary carrier energies.

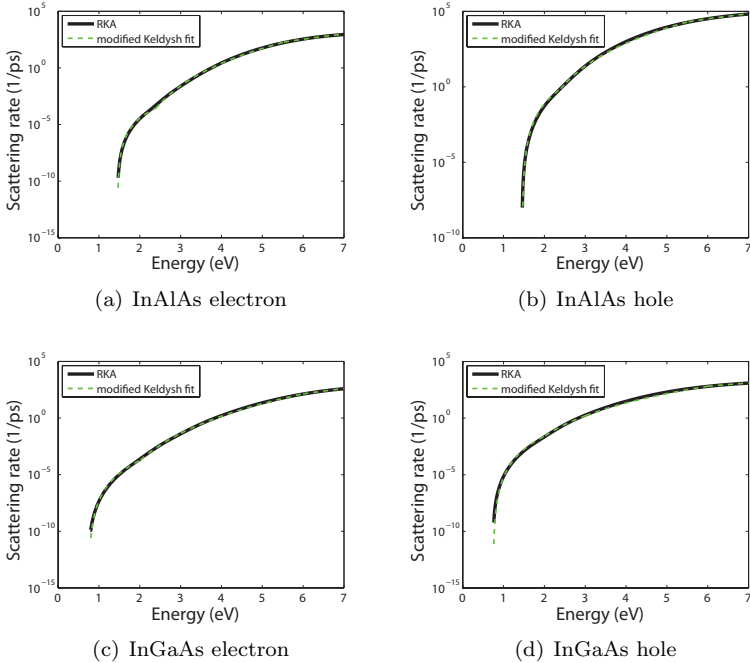


Figure 7.7: Modified Keldysh formulas fitted to the calculated RKA-based impact ionization rates of InAlAs and InGaAs.

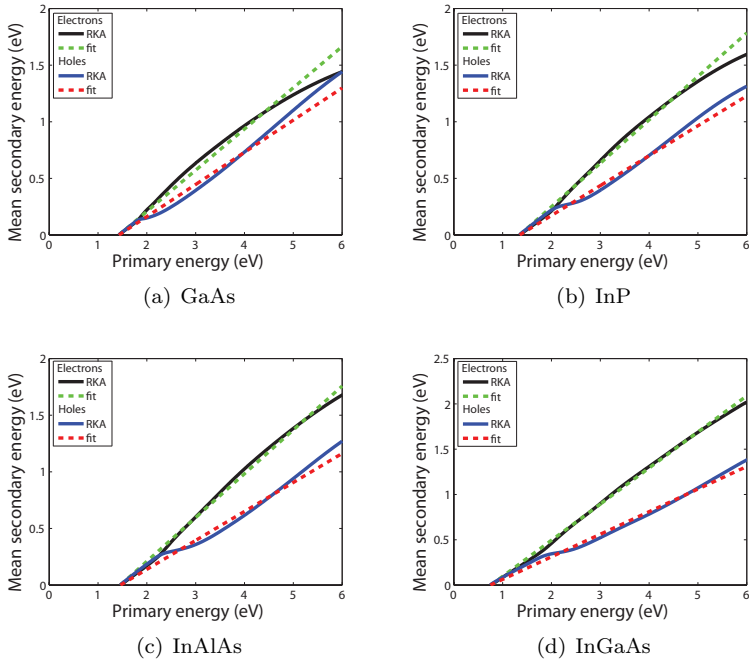


Figure 7.8: Mean secondary energies fitted to the RKA-based mean secondary energy functions.



## 7.3 Single Photon Avalanche Diodes

Parts of the following results have been published in Dolgos et al. [130, 131]. PIN diodes with multiplication (intrinsic) region widths between 55 nm and 500 nm have been simulated. The devices operate in the Geiger-mode at 300 K. The simulation procedure consists of a single electron injection for GaAs and InAlAs and a single hole injection for InP with an energy of 10 meV at the time  $t = 0$  ps into the PIN diode. Table 7.6 outlines the simulation domain boundaries and the positions of carrier injection for the three examined intrinsic region widths (compare with Fig. 5.1). The electron's injection position used in Ref. [130] was chosen in the region of low electric field being 1 nm away from the simulation domain boundaries. A semiconductor is an

$w$	left boundary	right boundary	e injection	h injection
55	350	517	497	370
250	350	710	690	370
500	350	950	930	370

Table 7.6: Simulation domain boundaries and positions of carrier injection. The intrinsic multiplication layer width  $w$ , the left and right simulation domain boundary positions, and the electron and hole injection position are given in units of nm.

electron gain material, if its impact ionization coefficient  $\alpha$  is higher than  $\beta$ , and vice versa for holes. Breakdown occurs, by definition, when the total number of charge carriers, being generated by impact ionization, exceeds 30 within the simulation domain. If a breakdown has not taken place within 500 ps, the simulation stops (compare with Fig. 6.3). The numerical experiments are repeated 2500 times per reverse bias point to gain sufficient statistics. Using Ramo's theorem [132] for the 55 nm GaAs device and the saturation velocities of Tan et al. [16], the breakdown criterion corresponds to a current of approximately 5.4  $\mu\text{A}$ . A breakdown criterion that leads to an early stop of the simulation of the avalanche build-up by means of the FBMC method makes the computation of SPAD statistics feasible on standard computer clusters. Small currents, estimated with Ramo's theorem, and hence few carriers in the simulation domain, possess

high fluctuations. A breakdown criterion using higher currents is computationally too expensive for FBMC simulations.

Fig. 7.9 presents the breakdown probability versus the reverse bias  $V_r$  and the excess bias  $V_{\text{ex}} = V_r - V_b$  for different multiplication region sizes for GaAs, InAlAs, and InP. The breakdown voltage  $V_b$  is defined as  $P_b(V_b) = 10^{-3}$ . Three regions characterize the curves. The breakdown probability ascends slowly in a small voltage interval immediately after the breakdown voltage. With higher reverse bias the breakdown probability increases linearly before it saturates toward unity. Tosi et al. [133] (Fig. 2, p. 301) and Campbell et al. [134] (Fig. 1, p. 2537) experimentally confirm the linear rise after the breakdown voltage for an InGaAs/InP SPAD. The smaller the multiplication region, the steeper is the rise of  $P_b$  with higher reverse bias for all three examined gain materials. A steep rise is advantageous for SPADs because it increases the photon detection efficiency for a constant excess bias. However, for the same excess bias, the electric fields are higher in thinner structures leading to an increased tunneling probability. The region of saturation is larger for increasing multiplier widths. Compared with the simpler models of Refs. [12, 15, 13, 14, 16], the FBMC simulations predict a less steep rise of the breakdown probability with reverse bias. For decreasing multiplication widths the balance between positive feedback of the avalanche and the reduction of the effective length of the gain material governs the behavior of the breakdown probability steepness [14] (p. 773) [16] (p. 044506-4). The smaller  $w$ , the higher is the electric field in the multiplication region for a constant applied bias. Two effects positively affect the charge avalanche. First, higher electric fields cause higher values of the impact ionization coefficients  $\alpha$  and  $\beta$ . Impact ionization takes place more often. Second, for higher electric fields the ratio of the impact ionization coefficients  $k$  tends toward unity (compare with Fig. 7.5). The definition of  $k$  is  $\alpha/\beta$  for electron gain materials and  $\beta/\alpha$  for hole gain materials. A value of  $k \approx 1$  leads to a more pronounced positive feedback of the impact ionization enforcing the avalanche [135] (p. 37). On the other hand, a smaller multiplication region reduces the available gain material length. Additionally, the smaller the multiplier, the higher is the ratio between the dead-space  $d$  and  $w$ . A higher  $d/w$  ratio corresponds to a further reduction of

the effective multiplication region thickness, and thus, has a negative implication on the avalanche. FBMC simulations of the multiplication process by means of the charge transport theory applied to GaAs, InAlAs, and InP SPADs reveal the dominance of the positive feedback over effects that diminish the avalanche. The consequence of a carrier injection near the simulation boundary in a region of low electric fields is a longer region of saturation of  $P_b$  versus  $V_r$  (compare with [130], Fig. 9(a)). For bigger  $w$ , and therefore lower electric fields, the breakdown probability saturates more slowly toward unity. The carrier's leaving of the simulation domain is more probable than for carriers injected in regions of higher electric fields.

Fig. 7.10 summarizes the simulated and the experimental breakdown voltages of the SPADs with different widths of the multiplication regions. For these simulations the carriers are injected 1 nm away from the simulation domain boundaries (compare with Table 7.6). Fits through the experimental breakdown voltages with data from Saleh et al. [136] (Figs. 1 and 2, p. 4038) are conducted to estimate the breakdown voltages for multiplier widths where no measurements exist. The breakdown voltages for GaAs and InP are well predicted. For InAlAs the simulated and the experimental breakdown voltages differ about 20 %, which indicates that a more precise band structure and calibration may be found.

Comparing the mean carrier energies  $\langle E_{ii} \rangle$  immediately before an impact ionization event shown in Fig. 7.11, reveals trends that can be estimated with the ratio between the impact ionization rates  $W_{ii}$  and the total carrier-phonon scattering rates  $W_{ph}$  (see Figs. 4.14 and C.5). The mean energies vary approximately in the energy interval where the ratio  $W_{ii}/W_{ph}$  varies from about 1% to 20%. For smaller multiplication regions, and therefore higher electric fields, the mean energies before the impact ionization events rise. GaAs and InP exhibit a similar rise of  $\langle E_{ii} \rangle$  with increasing voltages except for biases around the threshold. The higher slope of InAlAs indicates less effective dissipation mechanisms compared to GaAs and InP.

Fig. 7.12 shows the mean time to avalanche breakdown and the jitter versus the reverse bias and the excess bias for different widths of the multiplier made of GaAs, InAlAs, and InP. Both,  $\langle t_b \rangle$  and  $\sigma$  decrease exponentially for higher reverse biases. This finding agrees with experimental data of InGaAs/InP SPADs [101] (Fig. 12, p. 302).

The mean time to avalanche breakdown and the jitter feature a fast decline over reverse bias in a region after the breakdown voltage before the quantities evolve into an interval of small change with the reverse bias. Furthermore,  $\langle t_b \rangle$  and  $\sigma$  decrease for smaller multiplication region widths. The mean time to avalanche breakdown and the jitter descend with a sharper decline for smaller multiplication region sizes. The jitter decreases more than the mean time to avalanche breakdown for higher excess voltages. For example, increasing the excess bias from 0.5 V to 5 V at the 55 nm GaAs SPAD leads to a reduction of  $\langle t_b \rangle$  and  $\sigma$  of about an order of magnitude. All examined materials feature fluctuations of the time to breakdown and the jitter for biases around the breakdown voltage. The fluctuations are a result of the small number of avalanche breakdowns leading to low statistics. By trend,  $\langle t_b \rangle$  and  $\sigma$  tend to smaller values around  $V_b$ . Fig. 7.13 depicts the time to breakdown and the jitter versus the breakdown probability. For a given breakdown probability the time to avalanche and the jitter decrease for smaller multiplication region widths.

Fig. 7.14 presents the breakdown probability, the time to breakdown, and the jitter for GaAs, InAlAs, and InP in single plots. Fig. 7.14(b) reveals that the ordering of the breakdown probability versus the excess bias for changing widths of the gain material is preserved for all three examined materials:  $P_b$  versus  $V_{ex}$  is steeper for smaller  $w$ . GaAs exhibits the steepest slope. GaAs is followed by InP and InAlAs for the  $w = 55$  nm devices, and for  $w = 500$  nm, GaAs is followed by InAlAs and InP. The ordering of  $t_b$  and  $\sigma$  versus  $V_{ex}$  and  $P_b$  for different multiplication widths is preserved for GaAs, InAlAs, and InP: the time until the avalanche breakdown and its jitter becomes smaller for shrinking  $w$  (see Figs. 7.14(c), 7.14(d), 7.14(e), and 7.14(f)). Concerning the time to breakdown and the jitter versus the excess bias, GaAs exhibits the best characteristics followed by InP and InAlAs. Here, the improvement of the PDE and the time characteristics were considered. On the other hand, the material's breakdown voltage should be small and its band gap energy should be high to limit tunneling rates.

Fig. 7.15 illustrates the electric field profiles and the distributions of the number of impact ionization events over the real-space positions for different biases applied to the 55 nm GaAs SPAD. For higher electric fields impact ionization takes place more often and features

a broader distribution in real-space. The distributions of the times to avalanche breakdown narrow (compare with Fig. 7.16). The noisy (blue) distributions stem from simulations with voltages around  $V_b$  where breakdown occurs rarely. Fig. 7.17 depicts the number of impact ionization events versus the ionization path length of electrons and holes in the GaAs SPAD with  $w = 55$  nm. The normalized curves result in the probability density functions (PDFs) of the ionization path lengths. For increasing electric fields the total number of impact ionization events rises and the distribution narrows. The mean values of the impact ionization path length and the dead-spaces become shorter for higher applied voltages.

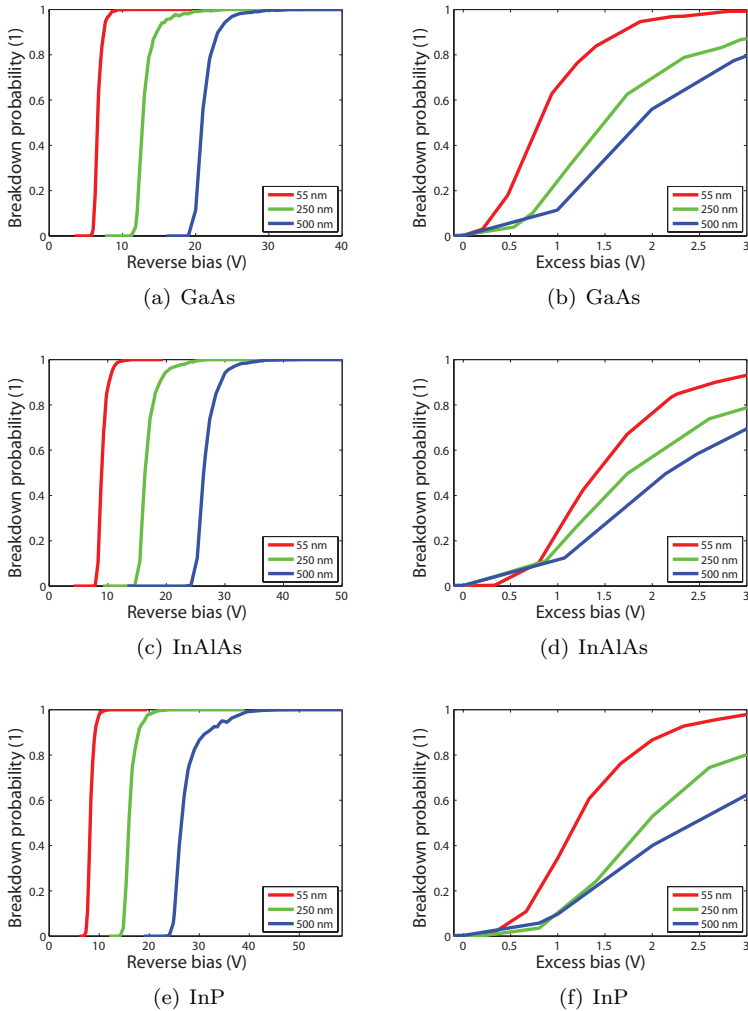


Figure 7.9: Breakdown probability for multiplication region widths of 55 nm, 250 nm, and 500 nm vs. the reverse bias and the excess voltage for GaAs, InAlAs, and InP.

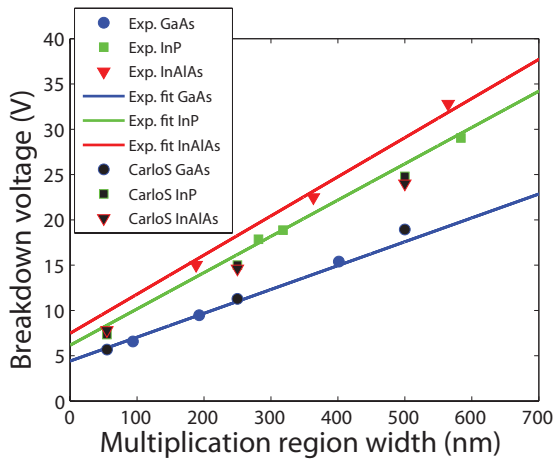


Figure 7.10: Breakdown voltages of GaAs, InP, and InAlAs SPADs with multiplier widths of 55 nm, 250 nm, and 500 nm compared with experimental data.

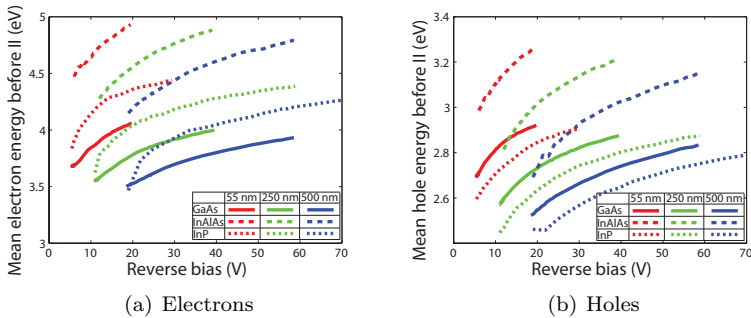


Figure 7.11: Comparison of energies immediately before impact ionization in GaAs, InAlAs, and InP SPADs.

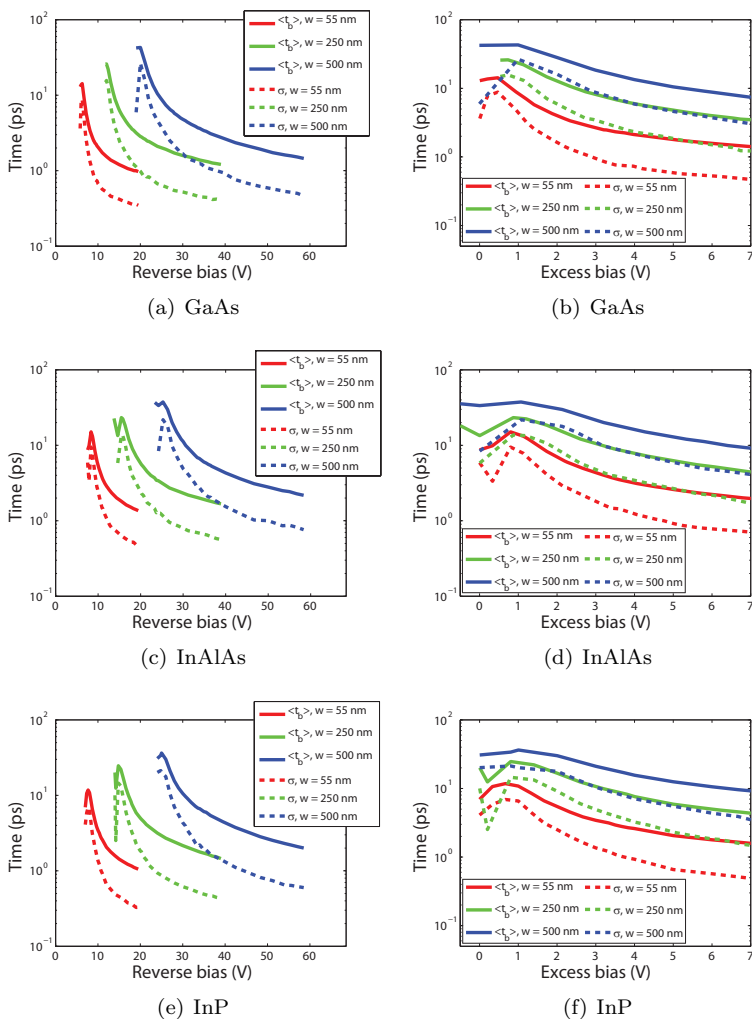


Figure 7.12: Mean time to avalanche breakdown  $\langle t_b \rangle$  and jitter  $\sigma$  for multiplication region widths of 55 nm, 250 nm, and 500 nm vs. the reverse bias and the excess bias for GaAs, InAlAs, and InP.



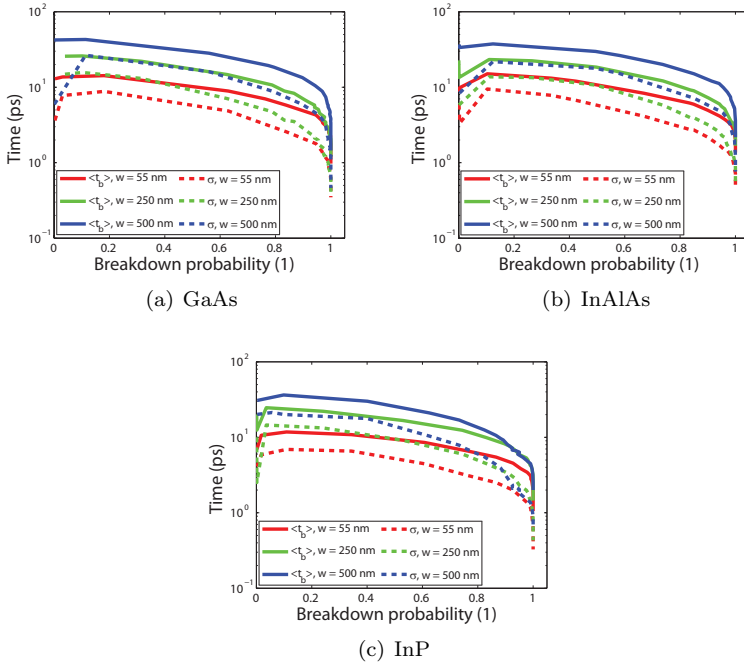


Figure 7.13: Mean time to avalanche breakdown  $\langle t_b \rangle$  and jitter  $\sigma$  for multiplication region widths of 55 nm, 250 nm, and 500 nm vs. the breakdown probability for GaAs, InAlAs, and InP.

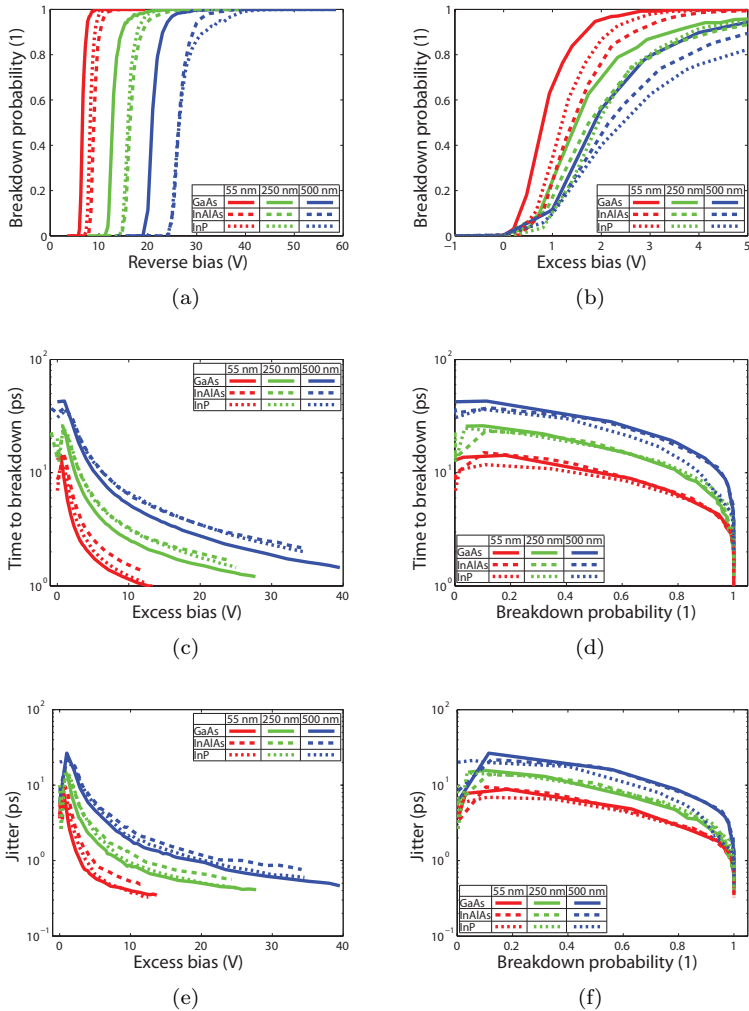


Figure 7.14: Comparison of SPAD breakdown characteristics for the materials GaAs, InAlAs, and InP.

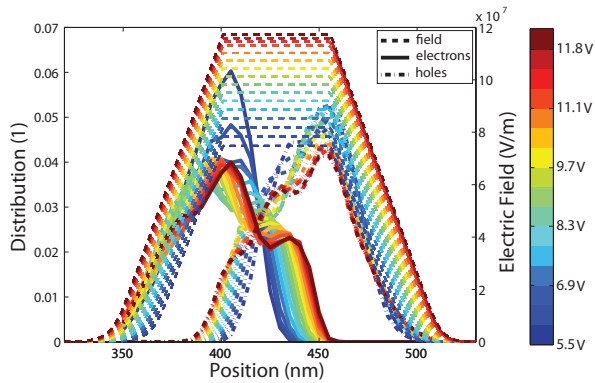


Figure 7.15: Electric field profiles (dashed lines) and distributions of the number of impact ionizations of electrons (full lines) and holes (dash dotted lines) vs. the real-space position for a series of applied voltages at the 55 nm GaAs SPAD. The dead-space decreases from 82 nm to 57 nm for applied voltages of 5.5 V and 11.8 V, respectively. The color map indicates the applied voltage.

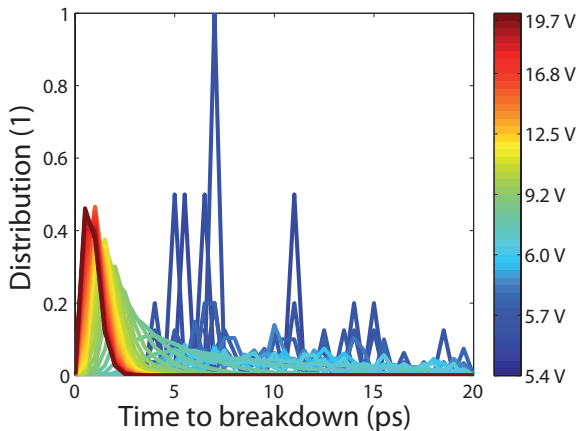
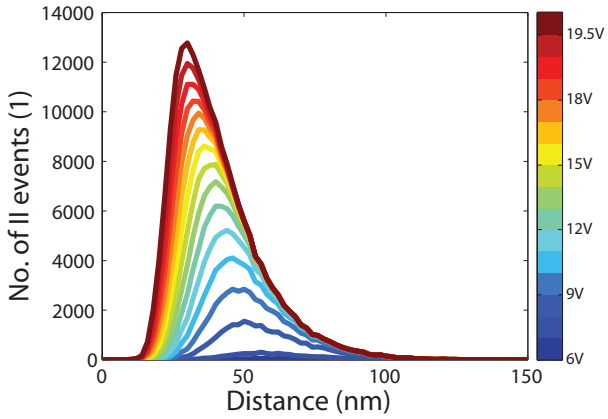
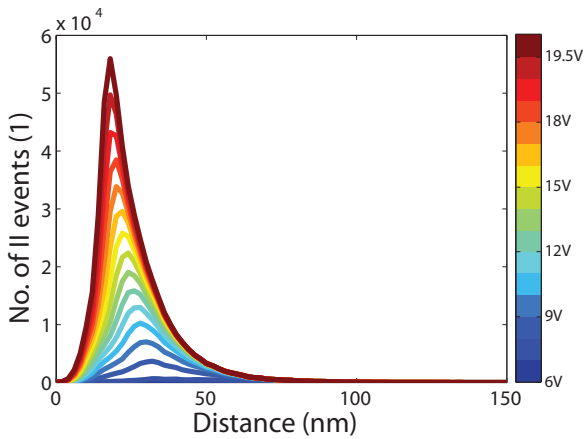


Figure 7.16: Distributions of the times to breakdown for the 55 nm GaAs SPAD. The color map indicates the applied voltage.



(a) Electrons



(b) Holes

Figure 7.17: Distribution of the number of impact ionizations vs. the ionization path length in the 55 nm GaAs SPAD.

# Chapter 8

## Conclusion and Outlook

### 8.1 Major Achievements

In this dissertation, the author has developed the full-band Monte Carlo device simulator *CarloS* for III-V compound semiconductors from scratch. Attention has been paid to achieve computationally efficient scattering expressions. All scattering rates have been calculated based on the same band structure, thus, keeping band structure consistency. As a result of the computationally efficient treatment of the scattering rates and the parallel CPU power of standard computer clusters, the FBMC simulation of single photon avalanche diode breakdown characteristics has become feasible. This thesis describes the modeling of the high-field carrier transport of the charge multiplication process in GaAs, InP, and InAlAs SPADs by means of the currently most accurate device simulation method within the physics of semiclassical charge transport. This puts the computation of SPAD properties on deeper theoretical grounds. Nonequilibrium effects like the dead-space, the nonlocal impact ionization and the velocity overshoot are modeled with the full-band Monte Carlo technique. The author has analyzed the behavior of the breakdown probability, the time to avalanche breakdown, and the jitter for different multiplication region widths. The breakdown probability exhibits a steeper rise with reverse bias for smaller multiplier sizes. The mean time to

avalanche breakdown and jitter decrease for shorter multiplication regions. Provided that tunneling rates in smaller multipliers are at an acceptable level, FBMC simulations suggest smaller multiplication region widths in SPADs for a given excess bias to improve the photon detection efficiency, the photon detection speed due to avalanche breakdown, and the jitter owing to avalanching impact ionization processes.

Only few of the impact ionization scattering rates and secondary carrier energies calculated with first principle methods are available in literature for the materials examined in this dissertation. The impact ionization scattering rates and the secondary carrier energies have been calculated using the random- $\mathbf{k}$  approximation for GaAs, InP, InAlAs, and InGaAs. This thesis provides the impact ionization scattering rates to the MC charge transport modeling community by means of piecewise modified Keldysh formulas with parameters fitted to the full-band calculated rates. The full-band calculated mean secondary carrier energies are analytically available through straight line fits. In order to compare the utilized material parameters with other FBMC parameters in detail, this work tabulates all the calculated deformation potentials, the valley density of states, the valley's local minimum positions and the local minimum energies.

## 8.2 Future Work

*CarloS* is able to simulate linear-mode APDs and Geiger-mode SPADs including the absorber and the multiplier layer. The absorption and multiplication region could consist of group IV or III-V semiconductors. Useful advancements like the multiple refresh method, the WKB tunneling model, and the Poisson equation solver are already implemented.

Concerning additional implementation work, *CarloS* may be extended to track particles in three real-space dimensions. Without self-consistency the extension is straightforward. Self-consistent MC simulations in three real-space dimensions make high demands on

the solution of the Poisson equation. To operate at maximum CPU capacity, a change from OpenMP to MPI is reasonable.

Concerning the physical modeling of high-energy transport in general, basic suggestions for the future work on the band structure computation, the evaluation of the transition rates, and the underlying transport model arise. Up to now, the dispersion relation of higher bands is uncertain for “well-known” semiconductors. Following the empirical ansatz, EPM parameters may be found that reproduce the band structure more realistically. However, as a prerequisite to be able to find better EPM parameters for III-V semiconductors, experimenters should provide more data to examine the real band structure. From a theoretical point of view, *ab initio* band structures without empirical fit parameters would be preferable compared to band structure calculations based on the EPM. The quantum mechanical matrix elements for carrier-phonon and carrier-carrier interactions, and therefore the coupling strengths, could be computed from the underlying band structure. The full-band phonon dispersion could be taken into account. Transition rates beyond Fermi’s golden rule could be examined including collisional broadening and the intracollisional field effect. The equations governing the phonon distribution could be coupled to the carrier transport equations. The semiclassical Boltzmann transport equation could be extended by quantum corrections and finally replaced by equations describing quantum transport. From a theoretical point of view, it is appealing to abandon the use of any fit parameter in the transport model.





# Appendix A

## Generation of Random Numbers According to Given Distributions

The very core of the Monte Carlo method is the usage of uniformly distributed random numbers  $r$  with  $0 < r < 1$  to generate random numbers according to a given distribution. This work uses the pseudo-random number generator *drand48()* of the standard library *stdlib*. The seed, to initialize the random number generator, depends on the simulation starting time in  $\mu\text{s}$ , and therefore, is practically random.

## A.1 Direct Technique

### A.1.1 Continuous Case

The function  $f(x)$  is defined on the interval  $(\check{a}, \check{b})$ . For a given random number  $r$  the random number  $x_r$  according to  $f(x)$  is given by [71] (Eq. (A4), p. 698)

$$r = F(x_r) = \frac{\int_{\check{a}}^{x_r} f(x) dx}{\int_{\check{a}}^{\check{b}} f(x) dx} . \quad (\text{A.1})$$

Then,  $x_r$  is generated with [29] (Eq. (3.4), p. 35)

$$x_r = F^{-1}(r) . \quad (\text{A.2})$$

The direct method is used when the integral, defined in Eq. (A.1), is analytically solvable and when Eq. (A.2) is representable in a closed form. Otherwise, the rejection technique is the method of choice.

### A.1.2 Discrete Case

Let there be the probability of the  $j$ th event  $P_j$ . Then, the  $i$ th event is chosen when [29] (Eq. (3.10), p. 36)

$$\sum_{j=1}^{i-1} P_j < r \leq \sum_{j=1}^i P_j \quad (\text{A.3})$$

holds true.

## A.2 Rejection Technique

Let there be a function  $g(x)$  being an upper estimate of  $f(x)$  [71] (Eq. (A9), p. 699):

$$g(x) \geq f(x) . \quad (\text{A.4})$$

The direct method has to be applicable to  $g(x)$ . In a first step  $x_{r_1}$  is drawn with the first random number  $r_1$  according to  $g(x)$  using the

direct method. The second step consists of the generation of a newly drawn random number  $r_2$ .  $x_{r_2}$  is accepted, if [71] (Eq. (A10), p. 699)

$$f(x_{r_1}) > r_2 g(x_{r_1}) \tag{A.5}$$

is fulfilled. Otherwise, one repeats the algorithm with newly drawn random numbers  $r_1$  and  $r_2$  until Eq. (A.5) holds true. A fast creation of random numbers according to the distribution  $f(x)$  by means of the rejection technique asks for an upper bound estimation function  $g(x)$  that is close as possible to  $f(x)$ . Then, the number of rejected  $x_{r_2}$  suggestions is minimal.



# Appendix B

## Useful Formulas

In this chapter useful formulas have been gathered that come along when a full-band Monte Carlo simulator is built. A useful conversion table from SI units to simulator units may be found in the thesis of Steiger [137] (Table A.1, p. 130).

### B.1 Irreducible Wedge

The corner points (in units of  $2\pi/a$ ) of the irreducible wedge of a crystal with cubic symmetry are  $\Gamma = (0, 0, 0)$ ,  $L = (0.5, 0.5, 0.5)$ ,  $X = (1, 0, 0)$ ,  $K = (0.75, 0.75, 0)$ ,  $W = (1, 0.5, 0)$ , and  $U = (1, 0.25, 0.25)$  with the lattice constant  $a$  (compare with Fig. 3.1). The five faces of the irreducible wedge in Hesse normal form are

- KLUW-plane:

$$\mathbf{k} \frac{1}{\sqrt{3}} \begin{pmatrix} 1 \\ 1 \\ 1 \end{pmatrix} = \frac{3}{2\sqrt{3}} \frac{2\pi}{a}, \quad (\text{B.1})$$

- UWX-plane:

$$\mathbf{k} \begin{pmatrix} 1 \\ 0 \\ 0 \end{pmatrix} = \frac{2\pi}{a}, \quad (\text{B.2})$$

- $\Gamma\text{LK}$ -plane:

$$\mathbf{k} \frac{1}{\sqrt{2}} \begin{pmatrix} 1 \\ -1 \\ 0 \end{pmatrix} = 0, \quad (\text{B.3})$$

- $\Gamma\text{LUX}$ -plane:

$$\mathbf{k} \frac{1}{\sqrt{2}} \begin{pmatrix} 0 \\ 1 \\ -1 \end{pmatrix} = 0, \quad (\text{B.4})$$

- $\Gamma\text{KWX}$ -plane:

$$\mathbf{k} \begin{pmatrix} 0 \\ 0 \\ 1 \end{pmatrix} = 0. \quad (\text{B.5})$$

## B.2 Transformation Matrices

The 48-fold symmetry of the cubic crystal system leads to 48 transformation matrices  $\mathbf{T}_i$  of the point group having the property

$$E_n(\mathbf{T}_i \mathbf{k}) = E_n(\mathbf{k}) \quad (\text{B.6})$$

with the band index  $n$ . The energy bands are invariant under eight spatial reflections [29] (Eq. (5.7), p. 76)

$$E_n(k_x, k_y, k_z) = E_n(|k_x|, |k_y|, |k_z|). \quad (\text{B.7})$$

The corresponding eight reflection matrices  $\mathbf{R}_i$  are

$$\begin{aligned} & \begin{pmatrix} 1 & 0 & 0 \\ 0 & 1 & 0 \\ 0 & 0 & 1 \end{pmatrix}, \begin{pmatrix} 1 & 0 & 0 \\ 0 & 1 & 0 \\ 0 & 0 & -1 \end{pmatrix}, \begin{pmatrix} 1 & 0 & 0 \\ 0 & -1 & 0 \\ 0 & 0 & 1 \end{pmatrix}, \\ & \begin{pmatrix} -1 & 0 & 0 \\ 0 & 1 & 0 \\ 0 & 0 & 1 \end{pmatrix}, \begin{pmatrix} 1 & 0 & 0 \\ 0 & -1 & 0 \\ 0 & 0 & -1 \end{pmatrix}, \begin{pmatrix} -1 & 0 & 0 \\ 0 & 1 & 0 \\ 0 & 0 & -1 \end{pmatrix}, \\ & \begin{pmatrix} -1 & 0 & 0 \\ 0 & -1 & 0 \\ 0 & 0 & 1 \end{pmatrix}, \begin{pmatrix} -1 & 0 & 0 \\ 0 & -1 & 0 \\ 0 & 0 & -1 \end{pmatrix}. \end{aligned} \quad (\text{B.8})$$

Furthermore, the energy bands are invariant under six permutations [29] (Eq. (5.8), p. 76)

$$\begin{aligned} E_n(k_x, k_y, k_z) &= E_n(k_z, k_x, k_y) = E_n(k_y, k_z, k_x) = \\ E_n(k_x, k_z, k_y) &= E_n(k_y, k_x, k_z) = E_n(k_z, k_y, k_x) . \end{aligned} \quad (\text{B.9})$$

The corresponding six permutation matrices  $\mathbf{P}_i$  are

$$\begin{aligned} &\begin{pmatrix} 1 & 0 & 0 \\ 0 & 1 & 0 \\ 0 & 0 & 1 \end{pmatrix}, \begin{pmatrix} 0 & 0 & 1 \\ 1 & 0 & 0 \\ 0 & 1 & 0 \end{pmatrix}, \begin{pmatrix} 0 & 1 & 0 \\ 0 & 0 & 1 \\ 1 & 0 & 0 \end{pmatrix}, \\ &\begin{pmatrix} 1 & 0 & 0 \\ 0 & 0 & 1 \\ 0 & 1 & 0 \end{pmatrix}, \begin{pmatrix} 0 & 1 & 0 \\ 1 & 0 & 0 \\ 0 & 0 & 1 \end{pmatrix}, \begin{pmatrix} 0 & 0 & 1 \\ 0 & 1 & 0 \\ 1 & 0 & 0 \end{pmatrix} . \end{aligned} \quad (\text{B.10})$$

The multiplication of the eight reflection and six permutation matrices leads to  $8 \cdot 6 = 48$  transformation matrices. The transformation matrices are orthogonal, and hence, fulfill the relation [54] (Eq. (4.30), p. 267)

$$\underline{\mathbf{T}}^{-1} = \underline{\mathbf{T}}^T \quad (\text{B.11})$$

### B.3 Cutting Cubes with Planes

The equi-energy plane is defined by

$$E(\mathbf{k}) = E(\mathbf{k}_{\text{cb}}) + \mathbf{n}(\mathbf{k} - \mathbf{k}_{\text{cb}}) \quad (\text{B.12})$$

with the cube center  $\mathbf{k}_{\text{cb}}$  and its normal vector  $\mathbf{n} = \nabla_{\mathbf{k}} E(\mathbf{k})|_{\mathbf{k}=\mathbf{k}_{\text{cb}}}$  that is given by the gradient at the center point. The distance of the plane from  $\mathbf{k}_{\text{cb}}$  is

$$\bar{w} = \frac{E(\mathbf{k}) - E(\mathbf{k}_{\text{cb}})}{|\mathbf{n}|} = \frac{\mathbf{n}}{|\mathbf{n}|}(\mathbf{k} - \mathbf{k}_{\text{cb}}) . \quad (\text{B.13})$$

The direction cosines of the gradient  $l_i$  are

$$l_i = \frac{\mathbf{n}\mathbf{e}_i}{|\mathbf{n}|} \quad (\text{B.14})$$

without loss of generality such that

$$l_1 \geq l_2 \geq l_3 \geq 0. \quad (\text{B.15})$$

The distances of the cube's corner points to the equi-energy plane are given by [57] (Eq. (13), p. 392)

$$\bar{w}_1 = b|l_1 - l_2 - l_3| \quad (\text{B.16a})$$

$$\bar{w}_2 = b(l_1 - l_2 + l_3) \quad (\text{B.16b})$$

$$\bar{w}_3 = b(l_1 + l_2 - l_3) \quad (\text{B.16c})$$

$$\bar{w}_4 = b(l_1 + l_2 + l_3) \quad (\text{B.16d})$$

with the cube's half width  $b$ . Depending on  $\bar{w}$  sweeping from 0 to  $\bar{w}_4$ , different polygons with  $n$  edges arise [57] (Eqs. (14)-(18), p. 392<sup>1</sup>):

1.  $0 \leq \bar{w} \leq \bar{w}_1$ :

(a)  $l_1 - l_2 - l_3 \geq 0$ : a parallelogram with the area

$$A(\bar{w}) = \frac{4b^2}{l_1}, \quad (\text{B.17})$$

(b)  $l_1 - l_2 - l_3 < 0$ : a hexagon having

$$A(\bar{w}) = \frac{2b^2(l_1l_2 + l_2l_3 + l_3l_1) - (\bar{w}^2 + b^2)}{l_1l_2l_3}, \quad (\text{B.18})$$

2.  $\bar{w}_1 \leq \bar{w} \leq \bar{w}_2$ : a pentagon with

$$A(\bar{w}) = \frac{b^2(3l_2l_3 + l_1l_2 + l_3l_1) - b\bar{w}(-l_1 + l_2 + l_3) - \frac{1}{2}(\bar{w}^2 + b^2)}{l_1l_2l_3}, \quad (\text{B.19})$$

3.  $\bar{w}_2 \leq \bar{w} \leq \bar{w}_3$ : a quadrangle exhibiting

$$A(\bar{w}) = 2 \frac{b^2l_3(l_1 + l_2) - b\bar{w}l_3}{l_1l_2l_3}, \quad (\text{B.20})$$

4.  $\bar{w}_3 \leq \bar{w} \leq \bar{w}_4$ : a triangle possessing

$$A(\bar{w}) = \frac{(b(l_1 + l_2 + l_3) - \bar{w})^2}{2l_1l_2l_3}. \quad (\text{B.21})$$

---

<sup>1</sup>for Eq. (16) a factor of 2 is wrong; compare with erratum



## B.4 Time to Cubic Box Boundaries

Let there be the transformation matrix  $\mathbf{T}$  (see App. B.2) that transforms the carrier at  $\mathbf{k}(t_0)$  at the time  $t_0$  into the irreducible wedge:  $\tilde{\mathbf{k}}(t_0) = \mathbf{T}\mathbf{k}(t_0)$ . Then, the transformed electric field is  $\tilde{\mathbf{E}} = \mathbf{T}\mathbf{E}$ . The propagation time  $t_{k,i}$  to the  $i$ th cube boundary plane in the irreducible wedge using Eq. (3.21) is given by

$$t_{k,i} = t_i - t_0 = \frac{d_i - \tilde{\mathbf{k}}(t_0)\mathbf{n}_i}{\frac{q}{h}\tilde{\mathbf{E}}\mathbf{n}_i}. \quad (\text{B.22})$$

The distance of the  $i$ th plane to the coordinate origin is

$$d_i = \mathbf{k}_{ij}^{\text{corn}}\mathbf{n}_i \quad (\text{B.23})$$

with the  $j$ th corner vector of the  $i$ th cubic box boundary plane  $\mathbf{k}_{ij}^{\text{corn}}$  and the boundary plane's normal vector

$$\mathbf{n}_i = \frac{(\mathbf{k}_{i,3}^{\text{corn}} - \mathbf{k}_{i,1}^{\text{corn}}) \times (\mathbf{k}_{i,2}^{\text{corn}} - \mathbf{k}_{i,1}^{\text{corn}})}{|(\mathbf{k}_{i,3}^{\text{corn}} - \mathbf{k}_{i,1}^{\text{corn}}) \times (\mathbf{k}_{i,2}^{\text{corn}} - \mathbf{k}_{i,1}^{\text{corn}})|} \quad (\text{B.24})$$

such that  $\tilde{\mathbf{E}}\mathbf{n}_i > 0$ .

## B.5 Reciprocal lattice vectors

If a carrier leaves the first Brillouin zone, the particle is transformed back by means of an Umklapp process  $\mathbf{k}_{\text{BZ}} = \mathbf{k} + \mathbf{G}$  with a reciprocal lattice vector [138] (p. 60 and 61)

$$\mathbf{G}_{\mathbf{h}} = h_1\mathbf{b}_1 + h_2\mathbf{b}_2 + h_3\mathbf{b}_3 \quad (\text{B.25})$$

such that  $\mathbf{k}$  is again within the first Brillouin zone. The reciprocal primitive lattice vectors for a face-centered cubic lattice in real-space are  $\mathbf{b}_1 = 2\pi/a (-1, 1, 1)$ ,  $\mathbf{b}_2 = 2\pi/a (1, -1, 1)$ , and  $\mathbf{b}_3 = 2\pi/a (1, 1, -1)$ . Furthermore,  $h_1$ ,  $h_2$ , and  $h_3$  are integers.

## B.6 Nonparabolic Expressions

### B.6.1 Band Structure

For small energies around a local valley minimum the nonparabolic approximated valley of a band structure is given by [71] (Eq. (3.5), p. 668)

$$\frac{\hbar^2 \mathbf{k}^2}{2m^*} = E(\mathbf{k})(1 + \bar{\alpha}E(\mathbf{k})) = \gamma(E) \quad (\text{B.26})$$

with the effective mass in the valley bottom  $m^*$  and the nonparabolicity  $\bar{\alpha}$ . The energy-dependent conductivity effective mass is

$$m_c(E) = m^*(1 + 2\bar{\alpha}E) \quad (\text{B.27})$$

and the velocity is given by

$$\mathbf{v}(\mathbf{k}) = \frac{\hbar \mathbf{k}}{m_c} . \quad (\text{B.28})$$

The energy and the  $\mathbf{k}$ -states are measured from the corresponding valley minima. Table B.1 shows the utilized band structure parameters for the nonparabolic approximation for GaAs and InP.

	$\Gamma_6$	$L_6$	$X_6$	$hh$	$lh$	$so$
GaAs [56]						
$\bar{\alpha}$ (eV <sup>-1</sup> )	1.16	0.51	0.58	0.84	0.76	0
$m^*$ ( $m_0$ )	0.063	0.292	0.471	0.61	0.0738	0.131
InP [67, 139]						
$\bar{\alpha}$ (eV <sup>-1</sup> )	0.83	0.23	0.38	-	-	-
$m^*$ ( $m_0$ )	0.078	0.26	0.325	0.45	0.12	0.21

Table B.1: Parameters for nonparabolically approximated band structure for GaAs and InP.

### B.6.2 Density of States

The density of states of a nonparabolic approximated valley is given by

$$\mathcal{D}(E) = \frac{(2m^*)^{3/2}}{2\pi^2 \hbar^3} \sqrt{E(1 + \bar{\alpha}E)}(1 + 2\bar{\alpha}E) \quad (\text{B.29})$$

where the kinetic energy  $E$  is measured from the valley bottom.

### B.6.3 Direction-Weighted Density of States

The analytical direction-weighted density of states is given by (compare with Fawcett et al. [140] (Eq. (2.10), p. 1967) and Eq. (4.18))

$$\mathcal{D}_{q^{-2}}(E) = \frac{\frac{e^2 \sqrt{m^*} \omega_{\text{op}}}{\sqrt{2\hbar}} \left( \frac{1}{\epsilon_{\infty}} - \frac{1}{\epsilon_0} \right) \frac{1+2\bar{\alpha}E'}{\sqrt{\gamma}}}{\frac{2\pi}{\hbar} e^2 F^2} F_0(E, E') \quad (\text{B.30})$$

with

$$F_0(E, E') = \frac{1}{C} \left( A \ln \left| \frac{\sqrt{\gamma} + \sqrt{\gamma'}}{\sqrt{\gamma} - \sqrt{\gamma'}} \right| + B \right) \quad (\text{B.31a})$$

$$A = (2(1 + \bar{\alpha}E)(1 + \bar{\alpha}E') + \bar{\alpha}(\gamma + \gamma'))^2 \quad (\text{B.31b})$$

$$B = -2\bar{\alpha}\sqrt{\gamma\gamma'} \\ \times (4(1 + \bar{\alpha}E)(1 + \bar{\alpha}E') + \bar{\alpha}(\gamma + \gamma')) \quad (\text{B.31c})$$

$$C = 4(1 + \bar{\alpha}E)(1 + \bar{\alpha}E')(1 + 2\bar{\alpha}E) \\ \times (1 + 2\bar{\alpha}E') \quad (\text{B.31d})$$

and the optical phonon angular frequency  $\omega_{\text{op}}$ , the static  $\epsilon_0$  and optical dielectric permittivity  $\epsilon_{\infty}$ , the polar coupling constant  $F$ , the energy  $E$  before and after scattering  $E' = E \pm \hbar\omega_{\text{op}}$ ,  $\gamma = \gamma(E)$ , and  $\gamma' = \gamma(E')$ .



# Appendix C

## Further Material Properties and Constants

### C.1 Fundamental Physical Constants

Table C.1 exhibits the unit conversion of the needed fundamental physical constants from SI units to units used in *CarloS*.

Physical constant	In SI units	In simulator units
$\hbar$	$1.055 \cdot 10^{-34}$ Js	$6.582 \cdot 10^{-4}$ eVps
$e$	$1.602 \cdot 10^{-19}$ C	1 e
$k_B$	$1.381 \cdot 10^{-23}$ J/K	$8.617 \cdot 10^{-5}$ eV/K
$\varepsilon_0$	$8.854 \cdot 10^{-12}$ F/m	$5.526 \cdot 10^{-2}$ e <sup>2</sup> /eVnm
$m_0$	$9.109 \cdot 10^{-31}$ kg	$5.686 \cdot 10^{-6}$ eVps <sup>2</sup> /nm <sup>2</sup>

Table C.1: Fundamental physical constants in SI units and simulator units.

## C.2 Material Parameters

In this part additional information about the calculated material properties of GaAs, InP, InAlAs, and InGaAs is summarized. Table C.2 presents the lattice constant  $a$ , the mass density  $\rho$ , the static  $\kappa_0$  and optical dielectric constants  $\kappa_\infty$ , and the longitudinal sound velocity  $u_l$  at 300 K. Tables C.3, C.4 and C.5 show the valley minimum positions and the corresponding valley minimum energies of the utilized full-band structure (see Chap. 3) evaluated with the customized steepest descent method (see Sec. 3.3). The equivalent valleys in the Brillouin zone enable different possibilities for the intervalley phonon wave vectors  $\mathbf{q}_{\nu\nu'}$ . The effective intervalley deformation potential from valley  $\nu$  to  $\nu'$  is the mean value of all possible equivalent transitions. Tables C.6, C.7, C.8 and C.9 present the calculated effective intervalley deformation potentials using Eq. (4.22). Table C.10 summarizes the used phonon energies. The intervalley phonon energies for transitions of higher conduction band valleys are taken to be overall 23 meV because no information was available. Table C.11 illustrates the computed number of valleys in the Brillouin zone. The knowledge of the number of valleys is necessary for the weighting of the carrier intervalley transition rates. The precomputed final valley DOS  $\mathcal{D}'_\nu(E)$  accounts for the available  $\mathbf{k}$ -space in all final valleys  $\nu'$  in the Brillouin zone. However, an electron in the valley  $\nu$  performing an intervalley transition has  $\nu_{\text{tot}} - 1$  available final valleys, excluding  $\nu' = \nu$ , with the number of final valleys  $\nu_{\text{tot}}$ . Thus, the final valley DOS has to be weighted with  $\nu_{\text{tot}} - 1 / \nu_{\text{tot}}$ .

Material constant	GaAs	InP	InAlAs	InGaAs
$a$ ( $10^{-10}$ m)	5.653 [98]	5.8697 [141]	5.869 [142]	5.867 [143]
$\rho$ ( $\text{kg}/\text{m}^3$ )	5360 [102]	4810 [144]	4900 [114]	5482 [115]
$\kappa_0$ (1)	12.90 [102]	12.5 [144]	12.46 [114]	13.1 [115]
$\kappa_\infty$ (1)	10.92 [102]	9.61 [144]	9.84 [114]	11.09 [115]
$u_l$ (m/s)	5400 [56]	5230 [144]	4679 [103]	4101 [115]

Table C.2: Material parameters.

	GaAs	InP
$\Gamma_6$	(0, 0, 0) 0.0	(0, 0, 0) 0.0
$L_6$	(0.49, 0.5, 0.5) 0.326	(0.49, 0.5, 0.5) 0.536
$X_6$	(0.85, 0, 0) 0.555	(0.93, 0.03, 0.01) 0.786
$X_7$	(1, 0, 0) 0.906	(0.99, 0.03, 0.01) 1.305
$c_{22}$	(0.29, 0, 0) 2.008	(0.34, 0.03, 0.01) 2.185
$c_{23}$	(0.74, 0.49, 0.25) 3.138	(0.76, 0.5, 0.23) 3.303
$c_{31}$	(0.05, 0.05, 0) 3.208	(0.06, 0.06, 0) 3.246
$c_{32}$	(0.7, 0.38, 0) 3.841	(0.71, 0.37, 0) 3.991
$c_{33}$	(0.5, 0.5, 0.46) 4.036	(0.5, 0.5, 0.47) 3.995
$c_{34}$	- -	- -
$c_{41}$	(0, 0, 0) 3.229	(0.03, 0.03, 0.03) 3.266
$c_{42}$	(1, 0.5, 0) 4.590	(0.99, 0.5, 0) 4.769
$c_{43}$	(0.39, 0.25, 0) 4.670	(0.42, 0.32, 0) 4.745
$c_{44}$	(0.5, 0.5, 0.5) 5.965	(0.49, 0.5, 0.5) 6.925

Table C.3: Electron valley minimum positions within the irreducible wedge and minimum energies of GaAs and InP. The positions (upper values) are in units of  $2\pi/a$ , the energies (lower values) are given in eV.



	InAlAs	InGaAs
$\Gamma_6$	(0, 0, 0) 0.0	(0, 0, 0) 0.0
$L_6$	(0.5, 0.49, 0.5) 0.652	(0.5, 0.49, 0.5) 0.898
$X_6$	(0.98, 0.02, 0.01) 1.019	(0.83, 0.03, 0.01) 1.808
$X_7$	(0.99, 0.02, 0.01) 1.535	(0.99, 0.02, 0.02) 2.052
$c_{22}$	(0.34, 0.02, 0.01) 2.533	(0.37, 0.03, 0.01) 3.050
$c_{23}$	(0.73, 0.48, 0.24) 3.729	(0.74, 0.48, 0.23) 4.474
$c_{31}$	(0.03, 0.03, 0.01) 3.621	(0.06, 0.06, 0) 4.415
$c_{32}$	(0.69, 0.36, 0) 4.619	(0.72, 0.38, 0) 5.275
$c_{33}$	(0.5, 0.5, 0.49) 4.328	(0.49, 0.49, 0.45) 5.310
$c_{34}$	(0, 0, 0) 4.674	(0.98, 0.5, 0) 5.283
$c_{41}$	(0.02, 0.02, 0.02) 3.629	(0.02, 0.02, 0.02) 4.444
$c_{42}$	(0.99, 0.5, 0) 5.635	(0, 0, 0) 6.163
$c_{43}$	(0.4, 0.25, 0) 5.218	(0.42, 0.31, 0) 5.903
$c_{44}$	(0.5, 0.49, 0.5) 7.170	(0.49, 0.5, 0.5) 7.356

Table C.4: Electron valley minimum positions within the irreducible wedge and minimum energies of InAlAs and InGaAs. The positions (upper values) are in units of  $2\pi/a$ , the energies (lower values) are given in eV.

	GaAs	InP	InAlAs	InGaAs
<i>hh</i>	(0, 0, 0)	(0, 0, 0)	(0, 0, 0)	(0, 0, 0)
	0.0	0.0	0.0	0.0
<i>lh</i>	(0, 0, 0)	(0, 0, 0)	(0, 0, 0)	(0, 0, 0)
	0.0	0.0	0.0	0.0
<i>so</i>	(0, 0, 0)	(0, 0, 0)	(0, 0, 0)	(0, 0, 0)
	0.350	0.207	0.344	0.392

Table C.5: Hole band minimum positions within the irreducible wedge and minimum energies for GaAs, InP, InAlAs, and InGaAs. The positions (upper values) are in units of  $2\pi/a$ , the energies (lower values) are given in eV.

	$\Gamma_6$	$L_6$	$X_6$	$X_7$	$c_{22}$	$c_{23}$	$c_{31}$	$c_{32}$	$c_{33}$	$c_{41}$	$c_{42}$	$c_{43}$	$c_{44}$
$\Gamma_6$	-	51.4	50.9	-	24.9	-	-	-	-	-	-	-	-
$L_6$	51.4	58.7	48.0	-	45.0	-	-	-	-	-	-	-	-
$X_6$	50.9	48.0	53.0	50.9	50.3	43.7	51.0	-	-	50.9	50.9	-	-
$X_7$	-	-	50.9	-	24.9	54.7	19.4	48.2	50.6	19.0	19.0	32.0	-
$c_{22}$	24.9	45.0	50.3	24.9	31.2	48.5	25.2	50.1	44.3	24.9	24.9	35.1	-
$c_{23}$	-	-	43.7	54.7	48.5	46.9	53.3	40.5	46.8	54.7	54.7	44.7	-
$c_{31}$	-	-	51.0	19.4	25.2	51.2	-	47.0	49.9	19.4	19.4	31.1	50.4
$c_{32}$	-	-	-	48.2	50.1	41.2	48.1	46.7	52.4	48.2	48.2	47.9	46.1
$c_{33}$	-	-	-	50.6	44.3	46.6	50.0	47.5	49.3	50.6	50.6	42.0	48.3
$c_{41}$	-	-	50.9	19.0	24.9	54.7	19.4	48.2	50.6	-	19.0	32.0	51.7
$c_{42}$	-	-	50.9	19.0	24.9	54.7	19.4	48.2	50.6	19.0	-	32.0	51.7
$c_{43}$	-	-	-	32.0	35.1	50.3	31.9	47.9	43.1	32.0	32.0	40.8	45.4
$c_{44}$	-	-	-	-	-	-	50.4	46.1	48.3	51.7	51.7	45.4	58.7

Table C.6: GaAs effective electron intervalley deformation potentials in units of eV/nm.

	$\Gamma_6$	$L_6$	$X_6$	$X_7$	$c_{22}$	$c_{23}$	$c_{31}$	$c_{32}$	$c_{33}$	$c_{41}$	$c_{42}$	$c_{43}$	$c_{44}$
$\Gamma_6$	-	50.2	53.7	56.7	27.1	-	-	-	-	-	-	-	-
$L_6$	50.2	57.1	47.7	49.4	42.3	45.0	48.7	-	-	47.7	-	-	-
$X_6$	53.7	47.7	47.9	43.4	49.4	41.0	53.7	-	-	53.7	-	-	-
$X_7$	56.7	49.4	43.4	47.7	52.1	42.1	54.7	43.4	48.2	55.2	41.4	45.9	-
$c_{22}$	27.1	43.8	51.2	54.2	31.5	46.5	27.2	49.0	43.9	27.1	51.3	37.2	-
$c_{23}$	-	45.1	42.9	42.1	46.5	46.0	52.6	43.7	46.4	51.7	44.8	44.1	-
$c_{31}$	-	48.7	53.7	54.7	27.2	50.1	-	46.0	47.9	20.6	58.6	34.5	-
$c_{32}$	-	-	-	43.4	49.0	43.7	47.2	45.8	49.2	47.0	43.9	45.7	45.2
$c_{33}$	-	-	-	48.2	41.4	44.2	48.5	46.1	42.0	47.1	41.5	45.4	-
$c_{41}$	-	47.7	53.7	55.2	27.1	51.7	20.6	46.9	49.3	-	60.6	34.5	47.7
$c_{42}$	-	-	-	41.4	51.3	44.8	60.2	43.9	41.5	60.6	46.0	47.8	42.8
$c_{43}$	-	-	-	46.8	35.9	45.8	34.9	45.7	46.8	34.5	47.8	44.4	45.4
$c_{44}$	-	-	-	-	-	-	-	45.0	-	47.7	42.8	45.1	57.1

Table C.7: InP effective electron intervalley deformation potentials in units of eV/mm.

	$\Gamma_6$	$L_6$	$X_6$	$X_7$	$c_{22}$	$c_{23}$	$c_{31}$	$c_{32}$	$c_{33}$	$c_{34}$	$c_{41}$	$c_{42}$	$c_{43}$	$c_{44}$
$\Gamma_6$	-	54.3	61.9	62.5	21.5	-	-	-	-	-	-	-	-	-
$L_6$	54.3	63.2	52.5	52.9	44.1	-	51.8	-	-	-	52.2	-	-	-
$X_6$	61.9	52.5	28.6	34.4	56.2	46.1	60.9	-	-	61.9	61.9	-	-	-
$X_7$	62.5	52.9	34.4	42.0	57.1	46.0	61.3	45.2	52.9	62.5	61.3	45.9	53.4	-
$c_{22}$	21.5	44.1	58.9	60.0	27.5	50.5	20.3	51.6	44.1	21.5	21.5	55.1	35.0	-
$c_{23}$	-	-	46.1	46.0	49.1	47.3	55.6	43.4	46.7	57.2	56.5	47.1	47.6	-
$c_{31}$	-	51.8	60.9	61.3	20.3	55.4	-	48.2	51.8	2.8	2.4	67.5	28.4	-
$c_{32}$	-	-	-	45.2	50.1	45.2	48.0	48.2	47.8	49.2	48.8	46.0	49.9	47.6
$c_{33}$	-	-	-	52.9	44.1	45.1	51.8	47.7	61.9	54.3	52.2	43.8	46.1	-
$c_{34}$	-	-	61.9	62.5	21.5	57.2	2.8	49.2	54.3	-	2.2	70.1	29.8	54.3
$c_{41}$	-	52.2	61.9	61.3	21.5	56.0	2.4	48.8	52.2	2.2	-	68.4	28.9	52.2
$c_{42}$	-	-	-	45.9	55.1	46.9	67.5	46.0	43.8	70.1	68.4	48.7	52.9	44.2
$c_{43}$	-	-	-	53.4	35.0	49.9	28.5	49.3	46.3	29.8	29.3	52.9	41.3	46.6
$c_{44}$	-	-	-	-	-	-	-	47.8	-	54.3	52.2	44.2	46.2	63.2

Table C.8: InAlAs effective electron intervalley deformation potentials in units of eV/nm.

	$\Gamma_6$	$L_6$	$X_6$	$X_7$	$c_{22}$	$c_{23}$	$c_{31}$	$c_{32}$	$c_{33}$	$c_{34}$	$c_{41}$	$c_{42}$	$c_{43}$	$c_{44}$
$\Gamma_6$	-	41.5	40.0	47.7	-	-	-	-	-	-	-	-	-	-
$L_6$	41.5	48.2	36.1	40.1	33.0	35.0	39.9	-	-	-	39.8	41.5	-	-
$X_6$	40.0	37.6	40.0	37.7	39.7	32.4	40.1	-	-	-	40.0	40.0	-	-
$X_7$	47.7	40.1	39.1	33.5	43.4	34.6	45.8	33.6	40.5	33.4	46.7	47.7	37.9	-
$c_{22}$	-	34.7	40.2	45.3	22.8	38.1	18.0	41.2	33.6	42.2	17.8	17.9	29.1	-
$c_{23}$	-	36.4	32.9	34.6	36.9	36.7	41.4	32.4	37.1	35.5	43.4	43.9	36.1	-
$c_{31}$	-	39.9	40.1	45.8	17.9	41.3	-	37.9	39.0	49.1	3.8	4.1	24.9	39.9
$c_{32}$	-	-	-	33.8	40.3	33.5	39.1	36.8	38.9	35.1	39.0	39.2	37.5	36.1
$c_{33}$	-	-	-	40.5	32.3	38.1	39.1	33.2	32.1	32.1	39.4	39.8	36.1	-
$c_{34}$	-	-	-	33.4	42.2	35.5	50.9	35.1	32.1	37.6	51.7	53.0	40.6	33.7
$c_{41}$	-	39.8	40.0	46.7	17.8	43.0	3.8	38.6	39.4	51.7	-	1.7	24.5	39.8
$c_{42}$	-	41.5	40.0	47.7	17.9	43.9	4.1	39.2	39.8	53.0	1.7	-	25.2	41.5
$c_{43}$	-	-	-	38.0	27.6	36.7	25.5	37.5	35.4	40.6	24.7	25.2	34.7	36.2
$c_{44}$	-	-	-	-	-	-	39.9	35.9	-	33.7	39.8	41.5	36.0	48.2

Table C.9: InGaAs effective electron intervalley deformation potentials in units of eV/nm.

	GaAs [102]	InP [67]	InAlAs [114]	InGaAs [106, 115]
Optical phonons				
	35.36	43.0	39.5	32.7
Intervalley phonons				
$\Gamma_6 \leftrightarrow L_6$	22.69	22.15	30.8	22.76
$\Gamma_6 \leftrightarrow X_6$	23.45	21.89	29.1	23.84
$L_6 \leftrightarrow L_6$	24.97	24.27	31.1	23.12
$L_6 \leftrightarrow X_6$	21.85	20.90	36.0	26.96
$X_6 \leftrightarrow X_6$	24.31	25.68	29.1	22.76
higher valleys	23.0	23.0	23.0	23.0

Table C.10: Optical and intervalley phonon energies in units of meV.

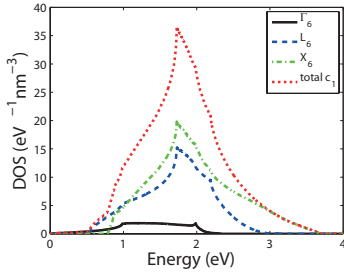
Valley	Number of valleys
$hh$	1
$lh$	1
$so$	1
$\Gamma_6$	1
$L_6$	4
$X_6$	3
$X_7$	3
$c_{22}$	6
$c_{23}$	4
$c_{31}$	1
$c_{32}$	24
$c_{33}$	4
$c_{34}$	12
$c_{41}$	1
$c_{42}$	12
$c_{43}$	24
$c_{44}$	4

Table C.11: Number of valleys in the Brillouin zone.

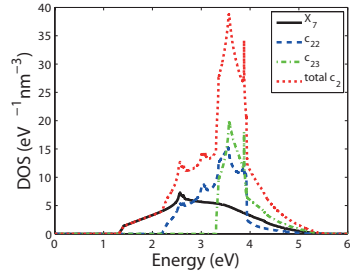


## C.3 Density of States

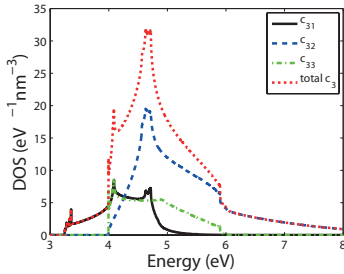
In this section, Figs. C.1, C.2, and C.3 illustrate the calculated DOS of InP, InAlAs, and InGaAs. The utilized full-band structures for MC simulations vary widely in literature. The DOS is a helpful property to compare the underlying band structures and scattering rates. Due to the constant matrix ansatz of Tang et al. [79], the carrier-phonon scattering rates mainly vary as a result of the available DOS.



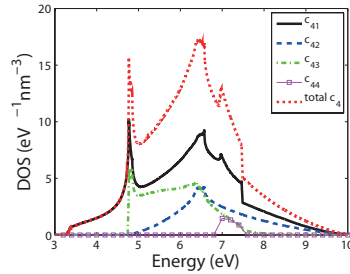
(a) Conduction band 1



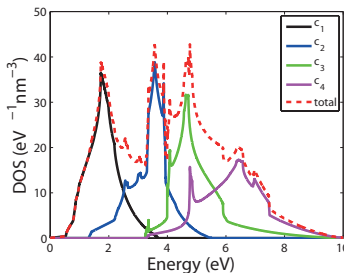
(b) Conduction band 2



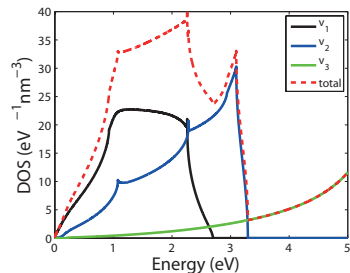
(c) Conduction band 3



(d) Conduction band 4

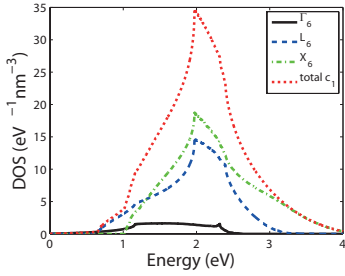


(e) Conduction bands

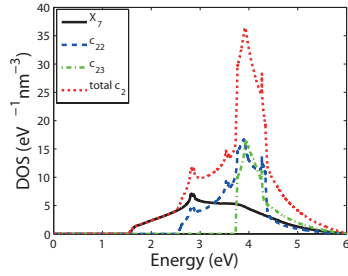


(f) Valence bands

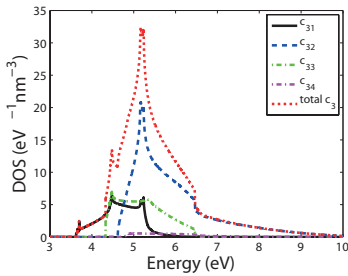
Figure C.1: Valley DOS of InP.



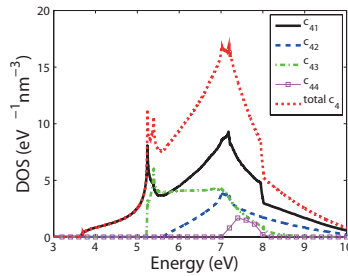
(a) Conduction band 1



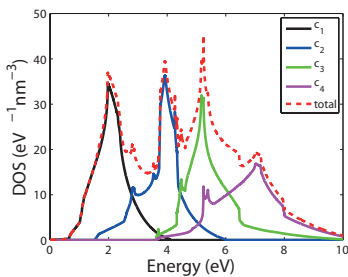
(b) Conduction band 2



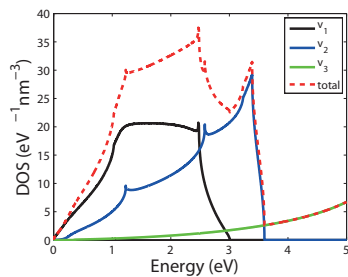
(c) Conduction band 3



(d) Conduction band 4

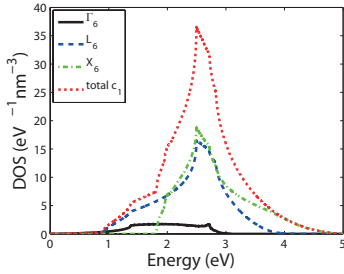


(e) Conduction bands

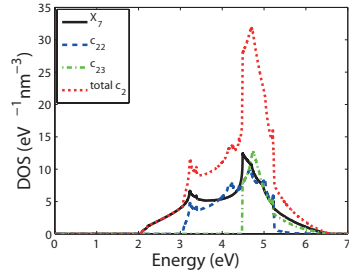


(f) Valence bands

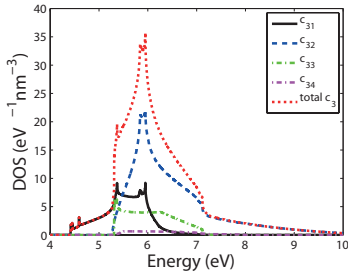
Figure C.2: Valley DOS of InAlAs.



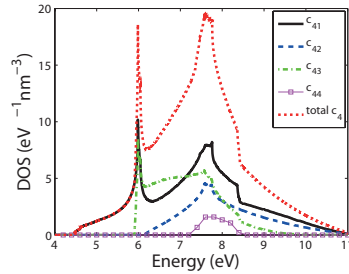
(a) Conduction band 1



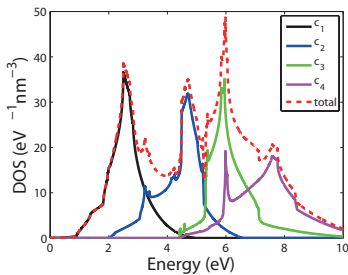
(b) Conduction band 2



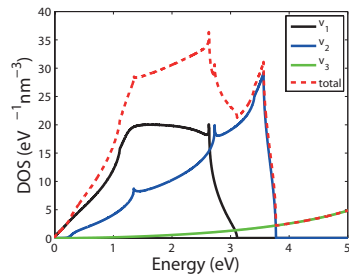
(c) Conduction band 3



(d) Conduction band 4



(e) Conduction bands



(f) Valence bands

Figure C.3: Valley DOS of InGaAs.

## C.4 Scattering Rates

Fig. C.4 presents a comparison between the full-band and the nonparabolic scattering rates in the  $\Gamma_6^-$ ,  $L_6^-$ , and  $X_6^-$ -valley of GaAs. The band parameters for the nonparabolic approximation are taken from Dunn et al. [56] (Table 3, p. 113). For details concerning the nonparabolic approximated band structure consult the PhD thesis of Hektor Meier [22]. The full-band and the nonparabolic scattering rates agree well for kinetic energies of about 1 eV above their valley minimum energies. For higher kinetic energies the nonparabolic approximation is not valid anymore. The mismatch of the scattering rate onset in the  $X_6^-$ -valley of about 100 meV originates from the different values for  $\Delta E_{\Gamma_6^- X_6^-}$ . In nonparabolic MC simulations  $\Delta E_{\nu\nu'}$  is taken from experiment. FBMC simulations rely on the calculated band structure. Fig. C.5 illustrates the total carrier-phonon and impact ionization scattering rates for InP, InAlAs, and InGaAs.

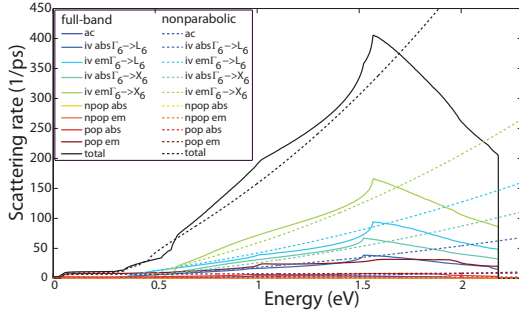
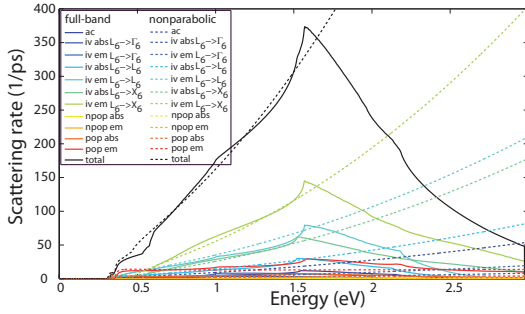
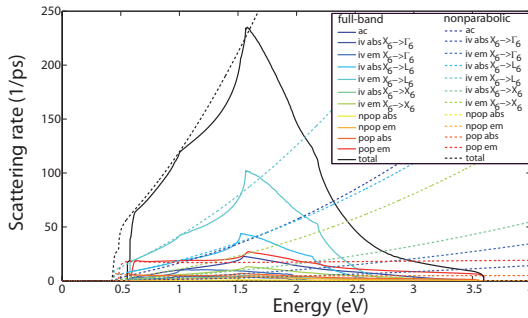
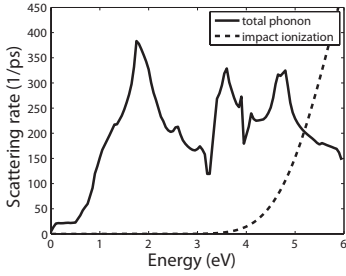
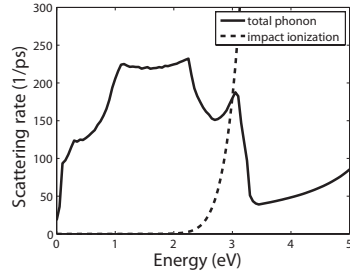

 (a)  $\Gamma_6$ -valley

 (b)  $L_6$ -valley

 (c)  $X_6$ -valley

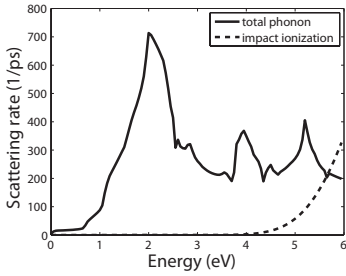
 Figure C.4: Comparison of full-band and nonparabolic scattering rates in the  $\Gamma_6$ -,  $L_6$ -, and  $X_6$ -valley of GaAs.



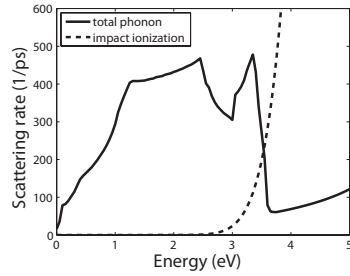
(a) InP electrons



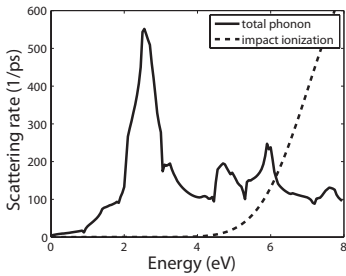
(b) InP holes



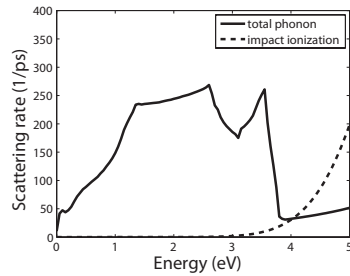
(c) InAlAs electrons



(d) InAlAs holes



(e) InGaAs electrons



(f) InGaAs holes

Figure C.5: Full-band carrier-phonon and impact ionization scattering rates of InP, InAlAs, and InGaAs.





# Notation and Acronyms

## Acronyms and Abbreviations

APD	avalanche photodiode
App.	appendix
BTE	Boltzmann transport equation
BZ	first Brillouin zone
Chap.	chapter
CMA	constant matrix approximation
CPU	central processing unit
DCR	dark count rate
DOS	density of states
EPM	empirical pseudopotential method
Eq.	equation
FBMC	full-band Monte Carlo
Fig.	figure
GaAs	gallium arsenide
hh	heavy hole band
InAlAs	indium aluminium arsenide
InGaAs	indium gallium arsenide
InP	indium phosphide
lh	light hole band
MC	Monte Carlo
MPI	message passing interface

NEGF	nonequilibrium Green's function
NIR	near infrared
OpenMP	open multi-processing
p.	page
PDE	photon detection efficiency
PDF	probability density function
RKA	random- $\mathbf{k}$ approximation
SACM	separate absorption charge and multiplication
SAM	separated absorption and multiplication
so	split-off band
SPAD	single photon avalanche diode
TCAD	technology computer-aided design
vs.	versus
WKB	Wentzel-Kramers-Brillouin

## Symbols

$A$	constant of the analytical polar optical phonon scattering rate
$A(w)$	area of the cut plane of the cubic box cut by the equi-energy plane
$A(\xi, t)$	microscopic quantity
$A_0$	area of the cut plane of the cubic box cut by the equi-energy plane
$A_{\text{BZ}}$	contribution of the cut plane of the cubic box cut by the equi-energy plane in the whole first Brillouin zone
$A_{\nu,i}(E)$	area of the cut plane of the cubic box cut by the equi-energy plane
$A_{\Delta}$	area of a triangle
$a$	lattice constant
$\mathbf{a}$	corner vector of a triangle
$\tilde{a}$	lower interval boundary
$B$	constant of the analytical polar optical phonon scattering rate

<b>B</b>	external magnetic field
$b$	half length of the cubic box edge
<b>b</b>	corner vector of a triangle
$\tilde{b}$	phonon branch index
$\check{b}$	upper interval boundary
$\mathbf{b}_{1,2,3}$	reciprocal primitive lattice vector
$C$	constant of the analytical polar optical phonon scattering rate
$C_{\tilde{b}}(\mathbf{k}, \mathbf{k}')$	carrier-phonon coupling strength
$c, c'$	conduction band index before, after scattering
$c_{nm}$	valley minimum position
<b>c</b>	corner vector of a triangle
$ c\rangle,  c'\rangle$	initial, final crystal quantum state
$D, D_{\nu}$	effective nonpolar optical deformation potential
$\tilde{D}$	nonpolar optical deformation potential
$D_{\nu\nu'}$	effective phonon intervalley deformation potential
$\tilde{D}_{\nu\nu'}$	intervalley phonon deformation potential
$D_{<}$	effective electron nonpolar optical phonon deformation potential for the $\Gamma_6$ -valley below $E_{\text{th}}^{\Gamma_6}$
$d$	dead-space
$d_i$	distance of the equi-energy plane to the coordinate origin
$\mathcal{D}(E)$	total density of states
$\mathcal{D}_{\text{ii}}(E_{\text{c},\nu})$	density of states overlap integral
$\mathcal{D}^{\text{max}}(E')$	maximal box density of states
$\mathcal{D}_{q^{-2},\nu}(\mathbf{k})$	direction-weighted density of states
$\mathcal{D}_{q^{-2},\nu,i}(\mathbf{k})$	direction-weighted box density of states
$\mathcal{D}_{q^{-2}}^{\text{max}}(\mathbf{k}')$	maximal direction-weighted box density of states
$\mathcal{D}_{\nu}(E)$	density of states in $\nu$
$\mathcal{D}_{\nu,i}(E)$	box density of states
$E, E'$	carrier energy before, after scattering
<b>E</b>	external electric field

$\tilde{E}$	transformed energy of the impact ionization rate fits
$\tilde{\mathbf{E}}$	transformed electric field
$E_{1,2}$	boundary of impact ionization rate fits
$E_{\text{box}}$	box energy interval
$E_{\text{box,max}}$	maximal energy within a cubic box
$E_{\text{box,min}}$	minimal energy within a cubic box
$E'_c$	secondary carrier energy after an impact ionization
$\hat{E}_{c'}$	integration boundary of conduction bands
$\langle E'_c \rangle (E_c)$	mean secondary carrier energy of an electron after impact ionization
$E'_{e,e1,e2}$	secondary carrier energy of an electron after impact ionization
$E_g$	band gap
$E'_{h,h1,h2}$	secondary carrier energy of a hole after impact ionization
$E_i$	energy interval
$\langle E_{ii} \rangle$	mean energy before impact ionization
$E_{\text{list}}$	energy interval list
$E_{\text{min,max}}^{\text{box}}$	minimum, maximum energy within a cubic box
$E_{nn'}^{\text{trans}}(\mathbf{k}, \mathbf{k}')$	energy transfer of an interaction process
$E_{n,\nu}$	carrier eigenenergy
$E_{\text{th}}$	impact ionization threshold energy
$E_{\text{th}}^{\Gamma_6}$	energy threshold for analytical treatment
$E_{\text{trans}}(\mathbf{q})$	energy transfer of an interaction process
$\hat{E}_{v'}$	integration boundary of valence bands
$\langle E'_{v'} \rangle (E_v)$	mean secondary carrier energy of a hole after impact ionization
$E_z$	$z$ -component of the external electric field
$e$	elementary charge
$\hat{e}_{x,y,z}$	unit vectors along the cubic box axes
$F$	polar coupling constant in the Fröhlich expression
$F(x_r)$	integrated distribution

$F_{\langle\phi\rangle}$	generalized driving force
$F_0(E, E')$	function of the analytical polar optical phonon scattering rate
$\mathbf{F}_\nu(\mathbf{r}, \mathbf{k}, t)$	external force in $\nu$
$f(\mathbf{r}, \mathbf{k}, t)$	semiclassical carrier distribution function
$f(x)$	distribution
$ f\rangle$	final quantum state
$f_\nu(\mathbf{r}, \mathbf{k}, t)$	semiclassical carrier distribution function in $\nu$
$\mathbf{G}, \mathbf{G}_h$	reciprocal lattice vector
$g(x)$	distribution
$\mathcal{G}(\mathbf{k}, \mathbf{k}')$	overlap integral
$\tilde{H}_p$	Fourier transform of the perturbation operator
$\hat{H}_p$	perturbation operator
$h, \hbar$	Planck constant, reduced Planck constant
$ i\rangle$	initial quantum state
$i_{\max}^{c,v}$	sum boundaries
$j_{\max}^{c,v}$	sum boundaries
$\mathbf{j}_{\langle\phi\rangle}$	generalized flux
$K$	corner point of irreducible wedge
$\mathbf{k}, \mathbf{k}'$	carrier wave vector before, after scattering
$k$	$k$ -ratio
$\tilde{\mathbf{k}}$	transformed carrier wave vector
$k_B$	Boltzmann constant
$\mathbf{k}_{\text{BZ}}$	$\mathbf{k}$ -vector inside the first Brillouin zone
$\mathbf{k}_{\text{cb}}$	center point of a cubic box
$\mathbf{k}_{ij}^{\text{corn}}$	$j$ th corner vector of the $i$ th cubic box boundary plane
$\mathbf{k}_{\text{end}}$	end $\mathbf{k}$ -point in the algorithm of the customized steepest descent method
$\mathbf{k}_{\text{min}}, \mathbf{k}_{\text{min},\nu}$	local minimum $\mathbf{k}$ -space position
$\mathbf{k}_{\text{min}}^{\text{wedge}}$	valley minimum position in the irreducible Brillouin zone
$\mathbf{k}_{\text{next}}$	next $\mathbf{k}$ -point in the algorithm of the customized steepest descent method

$\mathbf{k}_{\text{start}}$	starting $\mathbf{k}$ -point of the customized steepest descent algorithm
$\mathbf{k}_{\text{wedge}}$	$\mathbf{k}$ -vector inside the irreducible wedge
$k_{x,y,z}$	component of a $\mathbf{k}$ -vector
$L$	corner point of the irreducible wedge
$L_6$	valley minimum position
$L_s$	system size
$l_{1,2,3}$	direction cosines of the normal vector of the equi-energy plane
$l_m$	mean-free path
$l_\phi$	phase-relaxation length
$M$	matrix element of an interaction process
$\bar{M}$	oscillator mass
$M_d$	direct term of the impact ionization matrix element
$M_e$	exchange term of the impact ionization matrix element
$M_{ii}$	impact ionization Coulomb matrix element
$M_{nn'}(\mathbf{k}, \mathbf{k}')$	matrix element of an interaction process
$m$	slope of the fit function of the impact ionization secondary energy
$m^*$	effective mass
$m_0$	electron rest mass
$m_c$	conductivity effective mass
$m_\nu^*$	effective mass in the valley bottom
$N$	number of the cubic boxes in the $\hat{e}_x$ -direction
$N_{\text{cell}}$	number of unit cells
$N_{\text{sim}}$	number of carriers in the ensemble
$N_{\text{tot}}$	total number of cubic boxes discretizing the wedge
$n, n'$	band index before, after scattering
$\mathbf{n}$	normal vector of the equi-energy plane
$n(\mathbf{r}, t)$	particle density
$(n, \mathbf{k}), (n', \mathbf{k}')$	initial, final particle state
$n(\omega_{\tilde{\nu}}(\mathbf{q}))$	phonon occupation number

$\mathbf{n}_1$	unit vector showing from $\Gamma$ to a valley minimum
$n_{\text{op}}$	thermal equilibrium occupation number of optical phonons
$n_{\nu\nu'}$	intervalley phonon occupation number
$P$	probability
$\underline{P}$	permutation matrix
$P_0(t \xi_0, t_0)$	probability for zero scattering events
$P_b$	breakdown probability
$P_c$	probability that a carrier survives into the multiplication layer
$P_i(E')$	probability to select the $i$ th cubic box
$P_i^{\text{pop}}(E')$	probability to select the $i$ th cubic box for polar optical phonon scattering
$p$	momentum
$\mathbf{p}$	momentum vector
$p(\xi, t)$	single-particle probability density
$p(\xi, t \xi_0, t_0)$	conditional probability density
$p_0(\xi, t \xi_0, t_0)$	conditional probability density that the particle survives without scattering
$p_{1,2}(\xi, t \xi_0, t_0)$	conditional probability density for one, two scattering events
$p_i(\mathbf{k}')$	probability density for the final $\mathbf{k}$ -state after scattering
$q$	carrier charge
$\mathbf{q}$	phonon wave vector
$\mathbf{q}_{\text{ex}}$	wave vector of the external force
$q_{\text{min}}$	minimal momentum transfer for polar optical phonon scattering
$\underline{R}$	reflection matrix
$r, r_{1,2}$	random number
$\mathbf{r}, \mathbf{r}_{1,2}$	spatial coordinate
$\hat{S}[f]$	scattering operator
$s$	$y$ -intercept of the fit function of the impact ionization secondary energy
$T$	lattice temperature

$\underline{\mathbf{T}}$	transformation matrix, element of the point group of the cubic crystal system
$t$	time
$t_0$	current time
$t_1, t_2$	time
$t_T$	time interval till the time step of the synchronous ensemble
$t_b$	avalanche build-up time
$t_c$	duration of a collision
$t_{i,i+1}$	current, next synchronous ensemble time
$t_k$	time till the boundary of a $\mathbf{k}$ -space cubic box
$t_{\max}$	maximal simulation time
$t_{n,n+1}$	current, next simulation time
$t_{\text{off}}$	hold-off time
$t_r$	time till a real-space border
$t_s$	time till a scattering event
$U$	corner point of the irreducible wedge
$u_{\mathbf{k}}$	periodic part of the Bloch wave function
$u_l$	longitudinal sound velocity
$V$	crystal volume
$V(\mathbf{r}_1, \mathbf{r}_2)$	Coulomb interaction potential
$V_{\text{BZ}}$	volume of the first Brillouin zone
$V_b$	breakdown voltage
$V_{\text{cell}}$	volume of the unit cell
$V_{\text{cube}}$	volume of a cubic box
$V_{\text{ex}}$	excess bias
$V_r$	reverse bias
$V_{\text{wedge}}$	volume of the irreducible wedge
$V_\nu$	volume of the first Brillouin zone or valley
$v, v'$	valence band index before, after scattering
$\hat{v}$	velocity operator
$\mathbf{v}_{\text{wedge}}$	carrier velocity according to $\mathbf{k}_{\text{wedge}}$
$\mathbf{v}_\nu, \mathbf{v}_{\nu,i}$	carrier velocity in $\nu$
$W$	corner point of the irreducible wedge



$\tilde{W}$	transformed rate of the impact ionization rate fits
$W(\mathbf{k}, \mathbf{k}')$	transition rate
$W(\boldsymbol{\xi})$	scattering rate
$W(\boldsymbol{\xi}' \boldsymbol{\xi})$	transition rate
$W^\lambda(\mathbf{k})$	single contributions to the total scattering rate
$W_{\text{ac}}(\nu, \mathbf{k} \nu', \mathbf{k}')$	acoustic phonon transition rate
$W_{\text{ac}}(\nu, E)$	acoustic phonon scattering rate
$W_{\text{alloy}}(E)$	alloy scattering rate
$W_{\text{ee}}(E_c, E_{c'})$	distribution function of the impact ionization secondary carrier energy for primary electrons
$W_{\text{hh}}(E_v, E_{v'})$	distribution function of the impact ionization secondary carrier energy for primary holes
$W_{\text{ii}}(E_{c,v}(\mathbf{k}_{c,v}))$	impact ionization scattering rate
$\tilde{W}_{\text{ii}}(\mathbf{k}_{c,v})$	impact ionization scattering rate
$W_{\text{in}}^\lambda(\nu, \mathbf{k} \nu', \mathbf{k}')$	in-scattering transition rate
$W_{\text{iv}}^{\text{abs/em}}(\nu, \nu', E)$	intervalley phonon scattering rate
$W_{\text{iv}}^{\text{abs/em}}(\nu, \mathbf{k} \nu', \mathbf{k}')$	phonon intervalley transition rate
$W_n(\mathbf{k})$	scattering rate
$W_{nn'}(\mathbf{k}, \mathbf{k}')$	transition rate
$W_{\text{npop}}^{\text{abs/em}}(\nu, E)$	nonpolar optical phonon scattering rate
$W_{\text{npop}}^{\text{abs/em}}(\nu, \mathbf{k} \nu', \mathbf{k}')$	nonpolar optical phonon transition rate
$W_{\text{out}}^\lambda(\nu', \mathbf{k}' \nu, \mathbf{k})$	out-scattering transition rate
$W_{n'}^{\text{pop}}(E)$	polar optical phonon scattering rate
$W_{\text{pop}}^{\text{abs/em}}(n, \mathbf{k})$	polar optical phonon scattering rate
$W_{\text{real}}(\boldsymbol{\xi}' \boldsymbol{\xi})$	real-scattering transition rate
$W_{\text{self}}(\mathbf{k}', \mathbf{k})$	self-scattering transition rate
$W_{\text{self}}(\boldsymbol{\xi}' \boldsymbol{\xi})$	self-scattering transition rate
$W_{\text{tot}}(\nu, \mathbf{k})$	total scattering rate including self-scattering
$W_{\nu\nu'}^m(E)$	scattering rate
$w$	multiplication layer width
$w_i$	box weight of a boundary box
$\bar{w}, \bar{w}_{1,2,3,4}$	distance of the equi-energy plane from a cube center point

$\bar{w}_i$	statistical weight
$X$	corner point of the irreducible wedge
$X_6$	valley minimum position
$X_7$	valley minimum position
$x$	real-space coordinate
$\tilde{x}$	mole fraction
$x_r, x_{r1,2}$	random number according to a given distribution
$y$	real-space coordinate
$z$	real-space coordinate
$z_r$	border of the real-space grid
$\alpha$	electron impact ionization coefficient
$\bar{\alpha}$	nonparabolicity
$\bar{\alpha}_\nu$	nonparabolicity of a valley $\nu$
$\beta$	hole impact ionization coefficient
$\Gamma$	corner point of the irreducible wedge
$\bar{\Gamma}, \bar{\Gamma}(\boldsymbol{\xi}), \bar{\Gamma}(E(\mathbf{k}))$	total scattering rate including self-scattering
$\Gamma_6$	valley minimum position
$\bar{\Gamma}_i, \bar{\Gamma}_i(\boldsymbol{\xi})$	total scattering rate in $\Lambda_i$
$\gamma, \gamma_{e,h}$	exponent of the impact ionization rate fits
$\Delta E$	valley offset energy
$\Delta E_{i,j}$	integration discretization
$\Delta E_{\nu\nu'}$	valley offset energy
$\Delta V$	alloy interaction potential
$\Delta t$	propagation time
$\epsilon_0$	static dielectric permittivity
$\epsilon_\infty$	optical dielectric permittivity
$\varepsilon_0$	vacuum permittivity
$\zeta$	phonon polarization vector
$\eta_q$	quantum efficiency
$\kappa_0$	static dielectric constant
$\kappa_\infty$	optical dielectric constant

$\tilde{\Lambda}$	transformed prefactor of impact ionization rate fits
$\Lambda^{\text{ii}}$	impact ionization prefactor
$\Lambda^{\text{pop}}$	polar optical phonon prefactor
$\Lambda_{\text{e,h}}^{\text{ii}}$	impact ionization prefactor
$\Lambda_i$	region in the $\mathbf{r}$ - and $\mathbf{k}$ -space
$\Lambda_{\nu\nu'}, \Lambda_{\nu\nu'}^m$	scattering mechanism prefactor
$\lambda$	scattering mechanism index
$\lambda_{1,2}$	random variable to get a distribution on a triangle
$\lambda_B$	de Broglie wavelength
$\nu, \nu'$	valley or band index before, after scattering
$\nu_n(\mathbf{k})$	valley allocation function
$\nu_{\text{tot}}$	number of final valleys
$\Xi$	effective acoustic phonon deformation potential
$\tilde{\Xi}$	acoustic phonon deformation potential
$\Xi_\nu$	effective acoustic phonon deformation potential
$\Xi_{<}$	effective electron acoustic phonon deformation potential for the $\Gamma_6$ -valley below $E_{\text{th}}^{\Gamma_6}$
$\xi$	particle state vector
$\xi_0$	initial particle state vector
$\xi_{1,2}, \xi'_{1,2}$	particle state vector before, after scattering
$\xi_{\text{drift}}(t \xi_0, t_0)$	solution of the equation of motion
$\rho$	mass density of the semiconductor material
$\rho_{\mathbf{k}}$	density of states in the reciprocal space
$\sigma$	standard deviation
$\phi(\mathbf{k})$	function
$\Psi$	wave function
$\omega_{\bar{b}}(\mathbf{q})$	phonon angular frequency
$\omega_{\text{ex}}$	angular frequency of the external force
$\omega_{\text{op}}$	optical phonon angular frequency
$\omega_{\nu\nu'}$	intervalley phonon angular frequency
$\langle \dots \rangle$	ensemble average, mean value



# Bibliography

- [1] C. Jungemann, S. Keith, M. Bartels, and B. Meinerzhagen, “Efficient full-band Monte Carlo simulation of silicon devices,” *IEICE Transactions on Electronics*, vol. E82C, no. 6, pp. 870–879, 1999.
- [2] K. Hess, *Monte Carlo Device Simulation: Full Band and Beyond*. Kluwer Academic Publishers, Dordrecht, 1991.
- [3] E. Knill, R. Laflamme, and G. J. Milburn, “A scheme for efficient quantum computation with linear optics,” *Nature*, vol. 409, no. 6816, pp. 46–52, 2001.
- [4] N. Gisin, G. Ribordy, W. Tittel, and H. Zbinden, “Quantum cryptography,” *Reviews of Modern Physics*, vol. 74, no. 1, pp. 145–195, 2002.
- [5] J. Rarity and P. Tapster, “Experimental violation of Bell’s inequality based on phase and momentum,” *Physical Review Letters*, vol. 64, no. 21, pp. 2495–2498, 1990.
- [6] B. F. Aull, “Three-dimensional imaging with arrays of Geiger-mode avalanche photodiodes,” in *Proceedings of the Society of Photo-optical Instrumentation Engineers (SPIE)*, vol. 5353, no. 1, 2004, pp. 105–116.
- [7] V. W. S. Chan, “Free-space optical communications,” *Journal of Lightwave Technology*, vol. 24, no. 12, pp. 4750–4762, 2006.

- [8] A. Lacaita, F. Zappa, S. Bigliardi, and M. Manfredi, "On the bremsstrahlung origin of hot-carrier-induced photons in silicon devices," *IEEE Transactions on Electron Devices*, vol. 40, no. 3, pp. 577–582, 1993.
- [9] R. Cubeddu, D. Comelli, C. D'Andrea, P. Taroni, and G. Valentini, "Time-resolved fluorescence imaging in biology and medicine," *Journal of Physics D: Applied Physics*, vol. 35, no. 9, pp. R61–R76, 2002.
- [10] S. Cova, M. Ghioni, A. Lotito, I. Rech, and F. Zappa, "Evolution and prospects for single-photon avalanche diodes and quenching circuits," *Journal of Modern Optics*, vol. 51, no. 9, pp. 1267–1288, 2004.
- [11] M. Itzler, X. Jiang, M. Entwistle, K. Slomkowski, A. Tosi, F. Acerbi, F. Zappa, and S. Cova, "Advances in InGaAsP-based avalanche diode single photon detectors," *Journal of Modern Optics*, vol. 58, no. 3, pp. 174–200, 2011.
- [12] S. Wang, F. Ma, X. Li, G. Karve, X. Zheng, and J. C. Campbell, "Analysis of breakdown probabilities in avalanche photodiodes using a history-dependent analytical model," *Applied Physics Letters*, vol. 82, no. 12, p. 1971, 2003.
- [13] D. Ramirez, M. Hayat, G. Karve, J. Campbell, S. Torres, B. Saleh, and M. Teich, "Detection efficiencies and generalized breakdown probabilities for nanosecond-gated near infrared single-photon avalanche photodiodes," *IEEE Journal of Quantum Electronics*, vol. 42, no. 2, pp. 137–145, 2006.
- [14] J. Ng, C. Tan, J. David, and G. Rees, "Theoretical study of breakdown probabilities in single photon avalanche diodes," in *IEEE Lasers and Electro-Optics Society (LEOS) Annual Meeting*. IEEE, 2003, pp. 773–774.
- [15] M. Hayat, U. Sakoglu, J. Campbell, B. Saleh, and M. Teich, "Breakdown probabilities for thin heterostructure avalanche photodiodes," *IEEE Journal of Quantum Electronics*, vol. 39, no. 1, pp. 179–185, 2003.

- [16] S. L. Tan, D. S. Ong, and H. K. Yow, “Theoretical analysis of breakdown probabilities and jitter in single-photon avalanche diodes,” *Journal of Applied Physics*, vol. 102, no. 4, p. 044506, 2007.
- [17] E. Schöll, *Theory of Transport Properties of Semiconductor Nanostructures*. Chapman & Hall, London, 1998.
- [18] S. Datta, *Electronic Transport in Mesoscopic Systems*. Cambridge University Press, Cambridge, 1995.
- [19] H. Shichijo and K. Hess, “Band-structure-dependent transport and impact ionization in GaAs,” *Physical Review B*, vol. 23, no. 8, pp. 4197–4207, 1981.
- [20] K. K. Choi, D. C. Tsui, and K. Alavi, “Dephasing time and one-dimensional localization of two-dimensional electrons in GaAs/Al<sub>x</sub>Ga<sub>1-x</sub>As heterostructures,” *Physical Review B*, vol. 36, no. 14, pp. 7751–7754, 1987.
- [21] F. M. Bufer, *Full-Band Monte Carlo Simulation of Electrons and Holes in Strained Si and SiGe*. Herbert Utz, München, 1998.
- [22] H. Meier, “Design, characterization and simulation of avalanche photodiodes,” Ph.D. dissertation, Swiss Federal Institute of Technology Zurich, 2011.
- [23] Synopsys, Inc., *Sentaurus Device User Guide, version Y-2006.06*, Mountain View, California, USA, 2006.
- [24] U. Ravaioli, “Hierarchy of simulation approaches for hot carrier transport in deep submicron devices,” *Semiconductor Science and Technology*, vol. 13, no. 1, pp. 1–10, 1998.
- [25] M. Luisier and G. Klimeck, “Atomistic full-band simulations of silicon nanowire transistors: Effects of electron-phonon scattering,” *Physical Review B*, vol. 80, no. 15, p. 155430, 2009.
- [26] M. Frey, “Scattering in nanoscale devices,” Ph.D. dissertation, Swiss Federal Institute of Technology Zurich, 2010.

- [27] A. Esposito, “Band structure effects and quantum transport,” Ph.D. dissertation, Swiss Federal Institute of Technology Zurich, 2010.
- [28] D. K. Ferry, J. R. Barker, and C. Jacoboni, *Physics of Nonlinear Transport in Semiconductors*. Plenum Press, New York, 1980.
- [29] C. Jungemann and B. Meinerzhagen, *Hierarchical Device Simulation. The Monte Carlo Perspective*. Springer, Wien, 2003.
- [30] V. L. Bonč-Bruveič and S. G. Kalašnikov, *Halbleiterphysik*. VEB Deutscher Verlag der Wissenschaften, Berlin, 1982.
- [31] H. Kroemer, “Quasi-electric and quasi-magnetic fields in nonuniform semiconductors,” *RCA Review*, vol. 18, no. 3, pp. 332–342, 1957.
- [32] A. Schenk, *Advanced Physical Models for Silicon Device Simulation*. Springer, Wien, 1998.
- [33] C. Grinstead and J. L. Snell, *Introduction to Probability*. American Mathematical Society, 1997.
- [34] D. D. McCracken, “The Monte Carlo method,” *Scientific American*, vol. 192, no. 5, pp. 90–96, 1955.
- [35] T. Kurosawa, “Monte Carlo calculation of hot-electron problems,” *Journal of the Physical Society of Japan*, vol. S21, p. 424, 1966.
- [36] H. Kosina, M. Nedjalkov, and S. Selberherr, “Theory of the Monte Carlo method for semiconductor device simulation,” *IEEE Transactions on Electron Devices*, vol. 47, no. 10, pp. 1898–1908, 2000.
- [37] A. Pacelli and U. Ravaioli, “Analysis of variance-reduction schemes for ensemble Monte Carlo simulation of semiconductor devices,” *Solid-State Electronics*, vol. 41, no. 4, pp. 599–605, 1997.



- [38] C. Wordelman, T. Kwan, and C. Snell, "Comparison of statistical enhancement methods for Monte Carlo semiconductor simulation," *IEEE Transactions on Computer-Aided Design of Integrated Circuits and Systems*, vol. 17, no. 12, pp. 1230–1235, 1998.
- [39] K. Banoo, "Direct solution of the Boltzmann transport equation in nanoscale Si devices," Ph.D. dissertation, Purdue University, West Lafayette, USA, 2000.
- [40] F. Mustieles and F. Delaurens, "Numerical simulation of non-homogeneous submicron semiconductor devices by a deterministic particle method," *Solid-State Electronics*, vol. 36, no. 6, pp. 857–868, 1993.
- [41] C. Leung and P. Childs, "Spatially transient hot electron distributions in silicon determined from the Chambers path integral solution of the Boltzmann transport equation," *Solid-State Electronics*, vol. 36, no. 7, pp. 1001–1006, 1993.
- [42] M. A. Alam, "Computational studies of the physics of optoelectronic devices," Ph.D. dissertation, Purdue University, West Lafayette, USA, 1995.
- [43] M. Alam, M. Stettler, and M. Lundstrom, "Formulation of the Boltzmann equation in terms of scattering matrices," *Solid-State Electronics*, vol. 36, no. 2, pp. 263–271, 1993.
- [44] M. Alam, "Scattering matrix formulation of electron transport in compound semiconductor devices," *Solid-State Electronics*, vol. 37, no. 8, pp. 1509–1520, 1994.
- [45] D. Ventura, A. Gnudi, G. Baccarani, and F. Odeh, "Multidimensional spherical harmonics expansion of Boltzmann equation for transport in semiconductors," *Applied Mathematics Letters*, vol. 5, no. 3, pp. 85–90, 1992.
- [46] M. Galler and F. Schürer, "A deterministic solution method for the coupled system of transport equations for the electrons and phonons in polar semiconductors," *Journal of Physics A: Mathematical and General*, vol. 37, no. 5, pp. 1479–1497, 2004.

- [47] K. Kometer, G. Zandler, and P. Vogl, "Lattice-gas cellular-automaton method for semiclassical transport in semiconductors," *Physical Review B*, vol. 46, no. 3, pp. 1382–1394, 1992.
- [48] S. C. Brugger, A. Schenk, and W. Fichtner, "Moments of the inverse scattering operator of the Boltzmann equation: Theory and applications," *SIAM Journal on Applied Mathematics*, vol. 66, no. 4, pp. 1209–1226, 2006.
- [49] V. Peikert and A. Schenk, in *Proceedings of International Conference on Simulation of Semiconductor Processes and Devices (SISPAD)*, 2011, pp. 299–302.
- [50] J. Jakumeit, U. Ravaioli, and K. Hess, "Calculation of hot electron distributions in silicon by means of an evolutionary algorithm," *Journal of Applied Physics*, vol. 80, no. 9, pp. 5061–5066, 1996.
- [51] H. D. Rees, "Calculation of distribution functions by exploiting the stability of the steady state," *Journal of Physics and Chemistry of Solids*, vol. 30, no. 3, pp. 643–655, 1969.
- [52] C. Jacoboni, P. Poli, and L. Rota, "A new Monte Carlo technique for the solution of the Boltzmann transport equation," *Solid-State Electronics*, vol. 31, no. 3-4, pp. 523–526, 1988.
- [53] H. Rees, "Calculation of steady state distribution functions by exploiting stability," *Physics Letters A*, vol. 26, no. 9, pp. 416–417, 1968.
- [54] I. N. Bronstein, K. A. Semendjajew, G. Musiol, and H. Mühlig, *Taschenbuch der Mathematik*. Harri Deutsch, Frankfurt am Main, 2001.
- [55] M. V. Fischetti and S. E. Laux, "Monte Carlo simulation of electron transport in Si: The first 20 years," in *ESSDERC '96. Proceedings of the 26th European Solid State Device Research Conference*, 1996, pp. 813–820.
- [56] G. M. Dunn, G. J. Rees, J. P. R. David, S. A. Plimmer, and D. C. Herbert, "Monte Carlo simulation of impact ionization

- and current multiplication in short GaAs diodes,” *Semiconductor Science and Technology*, vol. 12, no. 1, pp. 111–120, 1997.
- [57] G. Gilat and L. J. Raubenheimer, “Accurate numerical method for calculating frequency-distribution functions in solids,” *Physical Review*, vol. 144, no. 2, pp. 390–395, 1966.
- [58] P. M. Marcus, J. F. Janak, and A. R. Williams, *Computational Methods in Band Theory*. Plenum Press, New York, 1971.
- [59] J. R. Chelikowsky and M. L. Cohen, “Nonlocal pseudopotential calculations for the electronic structure of eleven diamond and zinc-blende semiconductors,” *Physical Review B*, vol. 14, no. 2, pp. 556–582, 1976.
- [60] M. L. Cohen and V. Heine, “The fitting of pseudopotentials to experimental data and their subsequent application,” *Solid State Physics*, vol. 24, pp. 37–248, 1970.
- [61] Y. Zheng, R. Wang, and Y. Li, “The empirical pseudopotential method in the calculation of heterostructure band offsets,” *Journal of Physics: Condensed Matter*, vol. 8, no. 39, pp. 7321–7327, 1996.
- [62] A. Abramo, L. Baudry, R. Brunetti, R. Castagne, M. Charef, F. Dessenne, P. Dollfus, R. Dutton, W. Engl, R. Fauquembergue *et al.*, “A comparison of numerical solutions of the Boltzmann transport equation for high-energy electron transport silicon,” *IEEE Transactions on Electron Devices*, vol. 41, no. 9, pp. 1646–1654, 1994.
- [63] F. M. Bufler, *Full-Band Monte Carlo Simulation of Nanoscale Strained-Silicon MOSFETs*. Hartung-Gorre, Konstanz, 2003.
- [64] M. V. Fischetti and S. E. Laux, “Monte Carlo analysis of electron transport in small semiconductor devices including band-structure and space-charge effects,” *Physical Review B*, vol. 38, no. 14, pp. 9721–9745, 1988.
- [65] N. Sano and A. Yoshii, “Impact-ionization model consistent with the band structure of semiconductors,” *Journal of Applied Physics*, vol. 77, no. 5, pp. 2020–2025, 1995.

- [66] H. K. Jung, K. Taniguchi, and C. Hamaguchi, "Impact ionization model for full band Monte Carlo simulation in GaAs," *Journal of Applied Physics*, vol. 79, no. 5, pp. 2473–2480, 1996.
- [67] K. Brennan and K. Hess, "Theory of high-field transport of holes in GaAs and InP," *Physical Review B*, vol. 29, no. 10, pp. 5581–5590, 1984.
- [68] J. Bude and K. Hess, "Thresholds of impact ionization in semiconductors," *Journal of Applied Physics*, vol. 72, no. 8, p. 3554, 1992.
- [69] E. O. Kane, "Electron scattering by pair production in silicon," *Physical Review*, vol. 159, no. 3, pp. 624–631, 1967.
- [70] F. M. Bufler, A. Schenk, and W. Fichtner, "Proof of a simple time-step propagation scheme for Monte Carlo simulation," *Mathematics and Computers in Simulation*, vol. 62, no. 3–6, pp. 323–326, 2003.
- [71] C. Jacoboni and L. Reggiani, "The Monte Carlo method for the solution of charge transport in semiconductors with applications to covalent materials," *Reviews of Modern Physics*, vol. 55, no. 3, pp. 645–705, 1983.
- [72] C. Jacoboni and P. Lugli, *The Monte Carlo Method for Semiconductor Device Simulation*. Springer, Wien, 1989.
- [73] K. Tomizawa, *Numerical Simulation of Submicron Semiconductor Devices*. Artech House, Norwood, 1993.
- [74] B. K. Ridley, *Quantum Processes in Semiconductors*. Oxford Science Publications, Oxford, 1993.
- [75] C. Hamaguchi, *Basic Semiconductor Physics*. Springer, Berlin Heidelberg, 2001.
- [76] K. F. Brennan, *The Physics of Semiconductors*. Cambridge University Press, Cambridge, 1999.
- [77] K. Seeger, *Semiconductor Physics*. Springer, Berlin Heidelberg, 1985.

- [78] G. Czycholl, *Theoretische Festkörperphysik*. Springer, Berlin Heidelberg, 2008.
- [79] J. Y. Tang and K. Hess, “Impact ionization of electrons in silicon (steady state),” *Journal of Applied Physics*, vol. 54, no. 9, pp. 5139–5144, 1983.
- [80] W. Shockley and J. Bardeen, “Energy bands and mobilities in monatomic semiconductors,” *Physical Review*, vol. 77, no. 3, pp. 407–408, 1950.
- [81] J. Bardeen and W. Shockley, “Deformation potentials and mobilities in non-polar crystals,” *Physical Review*, vol. 80, no. 1, pp. 72–80, 1950.
- [82] T. Kunikiyo, M. Takenaka, Y. Kamakura, M. Yamaji, H. Mizuno, M. Morifuji, K. Taniguchi, and C. Hamaguchi, “A Monte Carlo simulation of anisotropic electron transport in silicon including full band structure and anisotropic impact-ionization model,” *Journal of Applied Physics*, vol. 75, no. 1, pp. 297–312, 1994.
- [83] P. D. Yoder, V. D. Natoli, and R. M. Martin, “Ab initio analysis of the electron-phonon interaction in silicon,” *Journal of Applied Physics*, vol. 73, no. 9, pp. 4378–4383, 1993.
- [84] C. Jungemann, S. Keith, F. M. Bufler, and B. Meinerzhagen, “Effects of band structure and phonon models on hot electron transport in silicon,” *Electrical Engineering*, vol. 79, no. 2, pp. 99–101, 1996.
- [85] N. W. Ashcroft and N. D. Mermin, *Solid State Physics*. W.B. Saunders Company, 1976.
- [86] C. May, “Impact ionization rate calculations for device simulation,” Diplomarbeit, ETH Zürich, 2005.
- [87] M. V. Fischetti, N. Sano, S. E. Laux, and K. Natori, “Full-band Monte Carlo simulation of high-energy transport and impact ionization of electrons and holes in Ge, Si, and GaAs,” in *SISPAD '96 - 1996 International Conference on Simulation of Semiconductor Processes and Devices*, 1996, pp. 43–44.

- [88] C. May and F. M. Bufler, "Threshold energy and impact ionization scattering rate calculations for strained silicon," *Journal of Computational Electronics*, vol. 6, no. 1, pp. 23–26, 2007.
- [89] L. Saravia and J. Duomarco, "The pair scattering and the photoemission effect in GaAs," *Journal of Physics and Chemistry of Solids*, vol. 34, no. 10, pp. 1661–1673, 1973.
- [90] N. Cavassilas, F. Aniel, G. Fishman, and R. Adde, "Full-band matrix solution of the Boltzmann transport equation and electron impact ionization in GaAs," *Solid-State Electronics*, vol. 46, no. 4, pp. 559–566, 2002.
- [91] D. Harrison, R. Abram, and S. Brand, "Impact ionization rate calculations in wide band gap semiconductors," *Journal of Applied Physics*, vol. 85, no. 12, pp. 8178–8185, 1999.
- [92] I. Oguzman, Y. Wang, J. Kolnik, and K. Brennan, "Theoretical study of hole initiated impact ionization in bulk silicon and GaAs using a wave-vector-dependent numerical transition rate formulation within an ensemble Monte Carlo calculation," *Journal of Applied Physics*, vol. 77, no. 1, pp. 225–232, 1995.
- [93] C. Cohen-Tannoudji, B. Diu, and F. Laloë, *Quantenmechanik 2.* de Gruyter, Berlin, 1999.
- [94] M. V. Fischetti, D. J. DiMaria, S. D. Brorson, T. N. Theis, and J. R. Kirtley, "Theory of high-field electron transport in silicon dioxide," *Physical Review B*, vol. 31, no. 12, pp. 8124–8142, 1985.
- [95] L. Reggiani, P. Lugli, and A.-P. Jauho, "Monte Carlo algorithms for collisional broadening and intracollisional field effect in semiconductor high-field transport," *Journal of Applied Physics*, vol. 64, no. 6, pp. 3072–3078, 1988.
- [96] W. Quade, F. Rossi, and C. Jacoboni, "A quantum description of impact ionization in semiconductors," *Semiconductor Science and Technology*, vol. 7, no. 3B, pp. B502–B505, 1992.

- [97] A. Kuligk, N. Fitzer, and R. Redmer, “Ab initio impact ionization rate in GaAs, GaN, and ZnS,” *Physical Review B*, vol. 71, no. 8, p. 085201, 2005.
- [98] K. F. Brennan, N. Mansour, and Y. Wang, “Simulation of advanced semiconductor devices using supercomputers,” *Computer Physics Communications*, vol. 67, no. 1, pp. 73–92, 1991.
- [99] D. Harrison, R. Abram, and S. Brand, “Characteristics of impact ionization rates in direct and indirect gap semiconductors,” *Journal of Applied Physics*, vol. 85, no. 12, pp. 8186–8192, 1999.
- [100] J. Geist and W. Gladden, “Transition rate for impact ionization in the approximation of a parabolic band structure,” *Physical Review B*, vol. 27, no. 8, pp. 4833–4840, 1983.
- [101] M. A. Itzler, R. Ben-Michael, C. F. Hsu, K. Slomkowski, A. Tosi, S. Cova, F. Zappa, and R. Ispasoiu, “Single photon avalanche diodes (SPADs) for 1.5  $\mu\text{m}$  photon counting applications,” *Journal of Modern Optics*, vol. 54, no. 2, pp. 283–304, 2007.
- [102] M. Fischetti, “Monte Carlo simulation of transport in technologically significant semiconductors of the diamond and zinc-blende structures. I. Homogeneous transport,” *IEEE Transactions on Electron Devices*, vol. 38, no. 3, pp. 634–649, 1991.
- [103] J. Mateos, T. González, D. Pardo, V. Hoel, H. Happy, and A. Cappy, “Improved Monte Carlo algorithm for the simulation of  $\delta$ -doped AlInAs/GaInAs HEMTs,” *IEEE Transactions on Electron Devices*, vol. 47, no. 1, pp. 250–253, 2000.
- [104] I. Watanabe, T. Torikai, and K. Taguchi, “Monte Carlo simulation of impact ionization rates in InAlAs-InGaAs square and graded barrier superlattice,” *IEEE Journal of Quantum Electronics*, vol. 31, no. 10, pp. 1826–1834, 1995.
- [105] C. A. Armiento and S. H. Groves, “Impact ionization in (100), (110), and (111) oriented InP avalanche photodiodes,” *Applied Physics Letters*, vol. 43, no. 2, pp. 198–200, 1983.

- [106] K. Brennan, "Theory of the steady-state hole drift velocity in InGaAs," *Applied Physics Letters*, vol. 51, no. 13, pp. 995–997, 1987.
- [107] K. Brennan and D. Park, "Theoretical comparison of electron real-space transfer in classical and quantum two-dimensional heterostructure systems," *Journal of Applied Physics*, vol. 65, no. 3, pp. 1156–1163, 1989.
- [108] G. Bulman, V. Robbins, K. Brennan, K. Hess, and G. Stillman, "Experimental determination of impact ionization coefficients in (100) GaAs," *IEEE Electron Device Letters*, vol. 4, no. 6, pp. 181–185, 1983.
- [109] G. Bulman, V. Robbins, and G. Stillman, "The determination of impact ionization coefficients in (100) gallium arsenide using avalanche noise and photocurrent multiplication measurements," *IEEE Transactions on Electron Devices*, vol. 32, no. 11, pp. 2454–2466, 1985.
- [110] L. W. Cook, G. E. Bulman, and G. E. Stillman, "Electron and hole impact ionization coefficients in InP determined by photomultiplication measurements," *Applied Physics Letters*, vol. 40, no. 7, pp. 589–591, 1982.
- [111] M. Haase, V. Robbins, N. Tabatabaie, and G. Stillman, "Sub-threshold electron velocity-field characteristics of GaAs and  $\text{In}_{0.53}\text{Ga}_{0.47}\text{As}$ ," *Journal of Applied Physics*, vol. 57, no. 6, pp. 2295–2298, 1985.
- [112] P. Hill, J. Schlafer, W. Powazinik, M. Urban, E. Eichen, and R. Olshansky, "Measurement of hole velocity in n-type InGaAs," *Applied Physics Letters*, vol. 50, no. 18, pp. 1260–1262, 1987.
- [113] P. A. Houston and A. G. R. Evans, "Electron drift velocity in n-GaAs at high electric fields," *Solid-State Electronics*, vol. 20, no. 3, pp. 197–204, 1977.
- [114] H. Kim, H. Tian, K. Kim, and M. Littlejohn, "Electron velocity-field characteristics of  $\text{In}_{0.52}\text{Al}_{0.48}\text{As}$ ," *Applied Physics Letters*, vol. 61, no. 10, pp. 1202–1204, 1992.



- [115] P. Bhattacharya, *Properties of Lattice-Matched and Strained Indium Gallium Arsenide*. Institution of Engineering and Technology, London, 1993.
- [116] A. Majerfeld, "Subthreshold velocity-field characteristics for bulk and epitaxial InP," *Journal of Applied Physics*, vol. 45, no. 8, pp. 3681–3682, 1974.
- [117] S. Millidge, D. C. Herbert, M. Kane, G. W. Smith, and D. R. Wight, "Non-local aspects of breakdown in pin diodes," *Semiconductor Science and Technology*, vol. 10, no. 3, pp. 344–347, 1995.
- [118] B. Nag, S. Ahmed, and M. Deb Roy, "Electron drift velocity in  $\text{Ga}_{0.47}\text{In}_{0.53}\text{As}$  at very high fields," *Physica B & C*, vol. 134, no. 1-3, pp. 519–522, 1985.
- [119] F. Osaka, T. Mikawa, and T. Kaneda, "Impact ionization coefficients of electrons and holes in (100)-oriented  $\text{Ga}_{1-x}\text{In}_x\text{As}_y\text{P}_{1-y}$ ," *IEEE Journal of Quantum Electronics*, vol. 21, no. 9, pp. 1326–1338, 1985.
- [120] T. Pearsall, F. Capasso, R. Nahory, M. Pollack, and J. Chelikowsky, "The band structure dependence of impact ionization by hot carriers in semiconductors: GaAs," *Solid-State Electronics*, vol. 21, no. 1, pp. 297–302, 1978.
- [121] N. Shigekawa, T. Furuta, and K. Arai, "High-field electron-transport properties in an  $\text{In}_{0.52}\text{Al}_{0.48}\text{As} / \text{In}_{0.53}\text{Ga}_{0.47}\text{As} / \text{In}_{0.52}\text{Al}_{0.48}\text{As}$  double heterostructure," *Journal of Applied Physics*, vol. 69, no. 7, pp. 4003–4010, 1991.
- [122] K. Taguchi, T. Torikai, Y. Sugimoto, K. Makita, and H. Ishihara, "Temperature dependence of impact ionization coefficients in InP," *Journal of Applied Physics*, vol. 59, no. 2, pp. 476–481, 1986.
- [123] I. Watanabe, T. Torikai, K. Makita, K. Fukushima, and T. Uji, "Impact ionization rates in (100)  $\text{Al}_{0.48}\text{In}_{0.52}\text{As}$ ," *IEEE Electron Device Letters*, vol. 11, no. 10, pp. 437–438, 1990.

- [124] T. Windhorn, L. Cook, and G. Stillman, "The electron velocity-field characteristic for n-In<sub>0.53</sub>Ga<sub>0.47</sub>As at 300 K," *IEEE Electron Device Letters*, vol. 3, no. 1, pp. 18–20, 1982.
- [125] T. H. Windhorn, L. W. Cook, and M. A. Haase, "Electron transport in InP at high electric fields," *Applied Physics Letters*, vol. 42, no. 8, p. 725, 1983.
- [126] A. You and D. Ong, "Monte Carlo modeling of high field carrier transport in bulk InP," in *ICSE 2000. 2000 IEEE International Conference on Semiconductor Electronics. Proceedings*. IEEE, 2000, pp. 168–172.
- [127] G. Zhou, A. Fischer-Colbrie, and J. Harris Jr, "IV kink in InAlAs/InGaAs MODFETs due to weak impact ionization process in the InGaAs channel," in *Conference Proceedings. Sixth International Conference on Indium Phosphide and Related Materials*. IEEE, 1994, pp. 435–438.
- [128] V. Palankovski and R. Quay, *Analysis and simulation of heterostructure devices*. Springer Verlag, Wien, 2004.
- [129] D. Dolgos, A. Schenk, and B. Witzigmann, "To be published," 2012.
- [130] D. Dolgos, H. Meier, A. Schenk, and B. Witzigmann, "Full-band Monte Carlo simulation of high-energy carrier transport in single photon avalanche diodes: Computation of breakdown probability, time to avalanche breakdown, and jitter," *Journal of Applied Physics*, vol. 110, no. 8, p. 084507, 2011.
- [131] D. Dolgos, H. Meier, A. Schenk, and B. Witzigmann, "To be published," 2012.
- [132] S. Ramo, "Currents induced by electron motion," in *IRE Proceedings*, vol. 27, no. 9, 1939, pp. 584–585.
- [133] A. Tosi, A. Dalla Mora, F. Zappa, and S. Cova, "Single-photon avalanche diodes for the near-infrared range: detector and circuit issues," *Journal of Modern Optics*, vol. 56, no. 2-3, pp. 299–308, 2009.

- [134] J. Campbell and C. Hu, “Infrared single photon avalanche detectors,” *Physica Status Solidi (c)*, vol. 7, no. 10, pp. 2536–2539, 2010.
- [135] E. Charbon and S. Donati, “SPAD sensors come of age,” *Optics and Photonics News (OPN)*, vol. 21, no. 2, pp. 35–41, 2010.
- [136] M. Saleh, M. Hayat, O. Kwon, A. Holmes, J. Campbell, B. Saleh, and M. Teich, “Breakdown voltage in thin III–V avalanche photodiodes,” *Applied Physics Letters*, vol. 79, no. 24, pp. 4037–4039, 2001.
- [137] S. Steiger, “Modelling nano-LEDs,” Ph.D. dissertation, Swiss Federal Institute of Technology Zurich, 2009.
- [138] F. M. Bufer and A. Schenk, “Lecture notes: Halbleitertransporttheorie und Monte-Carlo-Bauelements simulation.”
- [139] K. Brennan and K. Hess, “High field transport in GaAs, InP and InAs,” *Solid-State Electronics*, vol. 27, no. 4, pp. 347–357, 1984.
- [140] W. Fawcett, A. D. Boardman, and S. Swain, “Monte Carlo determination of electron transport properties in gallium arsenide,” *Journal of Physics and Chemistry of Solids*, vol. 31, no. 9, pp. 1963–1990, 1970.
- [141] I. Vurgaftman, J. Meyer, and L. Ram-Mohan, “Band parameters for III–V compound semiconductors and their alloys,” *Journal of Applied Physics*, vol. 89, no. 11, pp. 5815–5875, 2001.
- [142] E. Schubert, *Doping in III-V semiconductors*. Cambridge University Press, Cambridge, 1993.
- [143] K. Brennan, “Theoretical study of multi-quantum well avalanche photodiodes made from the GaInAs / AlInAs material system,” *IEEE Transactions on Electron Devices*, vol. 33, no. 10, pp. 1502–1510, 1986.
- [144] [Online]. Available: <http://www.ioffe.ru/SVA/NSM/Semicond/index.html>



# Curriculum Vitae

Denis Dolgos was born on the 6th of October 1981 in Böblingen, Germany. He enjoyed his childhood in Herrenberg, Baden-Württemberg, Germany. From 2001 he studied physics at the University of Stuttgart and received the Dipl.-Phys. degree in 2007. Denis made his diploma work at the Max Planck Institute for Metals Research in Stuttgart. From 2008 to 2011 he was a research and teaching assistant at the Integrated Systems Laboratory at the Swiss Federal Institute of Technology Zurich (ETH Zürich) in Switzerland. His research interests lie in the Monte Carlo modeling of semiconductor physics. In the spare time, Denis enjoys playing the guitar.